SIV-specific neutralizing antibody induction following selection of a PI3K drive-attenuated *nef* variant

Hiroyuki Yamamoto[*1,2,3] and Tetsuro Matano[*1,3,4]

[1]AIDS Research Center, National Institute of Infectious Diseases, 4-7-1 Gakuen, Musashi-Murayama City, Tokyo 208-0011, Japan

[2]Department of Biomedicine, University Hospital Basel, Hebelstrasse 20, Basel 4031, Switzerland

[3]Joint Research Center for Human Retrovirus Infection, Kumamoto University, 2-2-1 Honjo, Kumamoto 860-0811, Japan

[4]The Institute of Medical Science, The University of Tokyo, 4-6-1 Shirokanedai, Minato-ku, Tokyo 108-8639, Japan

*Correspondence:

Hiroyuki Yamamoto, AIDS Research Center, National Institute of Infectious Diseases, 4-7-1 Gakuen, Musashi-Murayama City, Tokyo 208-0011, Japan. Phone: +81-42-848-7154; Fax: +81-42-848-7155. Email: h-yamato@niid.go.jp

Tetsuro Matano, National Institute of Infectious Diseases, 1-23-1 Toyama, Shinjuku-ku, Tokyo 162-8640, Japan. Phone: +81-3-4582-2811; Fax: +81-3-5285-1165. Email: tmatano@niid.go.jp

Running title: SIV neutralization post-PI3K diminution

Abstract

HIV and simian immunodeficiency virus (SIV) infections are known for impaired neutralizing antibody (NAb) responses. While sequential virus-host B cell interaction appears to be basally required for NAb induction, driver molecular signatures predisposing to NAb induction still remain largely unknown. Here we describe SIV-specific NAb induction following a virus-host interplay decreasing aberrant viral drive of phosphoinositide 3-kinase (PI3K). Screening of seventy difficult-to-neutralize SIV_{mac239}-infected macaques found nine NAb-inducing animals, with seven selecting for a specific $CD8^+$ T-cell escape mutation in viral *nef* before NAb induction. This Nef-G63E mutation reduced excess Nef interaction-mediated drive of B-cell maturation-limiting PI3K/mammalian target of rapamycin complex 2 (mTORC2). *In vivo* imaging cytometry depicted preferential Nef perturbation of cognate Envelope-specific B cells, suggestive of polarized contact-dependent Nef transfer and corroborating cognate B-cell maturation post-mutant selection up to NAb induction. Results collectively exemplify a NAb induction pattern extrinsically reciprocal to human PI3K gain-of-function antibody-dysregulating disease, and indicate that harnessing the PI3K/mTORC2 axis may facilitate NAb induction against difficult-to-neutralize viruses including HIV/SIV.

Keywords

neutralizing antibody; B cells; $CD8^+$ T cells; PI3 kinase; inborn errors of immunity; HIV/SIV

45 **Introduction**

46

47 Virus-specific neutralizing antibody (NAb) responses by B cells are induced by an
48 intricate cooperation of adaptive immune cells (Kumar et al., 2010; Shulman et al., 2014; Giltin
49 et al., 2014; Wang et al., 2014) and often play a central role in clearance of acute viral
50 infections (Junt et al., 2007). In contrast, persistence-prone viruses such as human
51 immunodeficiency virus type 1 (HIV-1), simian immunodeficiency virus (SIV) and lymphocytic
52 choriomeningitis virus (LCMV) variously equip themselves with B cell/antibody-inhibitory
53 countermeasures (Moir et al., 2001; Mattapallil et al., 2005; Sommerstein et al., 2015;
54 Sammicheli et al., 2016; Fallet et al., 2016; Mason et al., 2016), impairing NAb induction
55 (Levesque et al.,2009; Mikell et al., 2011). These viruses successfully suppress elicitation of
56 potent NAb responses, especially in acute infection (Hunziker et al., 2003; Tomaras et al.,
57 2008), and establish viral persistence, posing considerable challenge for developing protective
58 strategies. In particular, HIV and SIV establish early a large body of infection *in vivo* from early
59 on with a distinct host genome-integrating retroviral life cycle (Whitney et al., 2014). In addition,
60 these lentiviruses are unique in launching a matrix of host immune-perturbing interactions
61 mainly by their six remarkably pleiotropic accessory viral proteins, which optimally fuels viral
62 pathogenesis (Kirchhoff et al., 1995; Sheehy et al., 2002; Harris et al., 2003; Schindler et al.,
63 2006; Neil et al., 2008; Zhang et al., 2009; Laguette et al., 2011; Yamada et al., 2018; Joas et
64 al., 2018; Langer et al., 2019; Yan et al., 2019; Joas et al., 2020; Khan et al., 2020; Volcic et
65 al., 2020; Reuschl et al., 2022). A body of evidence has depicted this in the last decades, its
66 entity, including focal mechanisms of humoral immune perturbation in HIV/SIV infection,
67 remains elusive to date.

68 Adverse virus-host interactions in HIV/SIV infection leads to a detrimental consequence
69 of the absence of acute-phase endogenous NAb responses. Contrasting this, we and others
70 have previously described in *in vivo* experimental models that passive NAb infusion in the
71 acute phase can trigger an endogenous T-cell synergism resulting in robust control of
72 SIV/SHIV (simian/human immunodeficiency virus) (Haigwood et al., 1996; Yamamoto et al.,

73 2007; Ng et al., 2010; Iseda et al., 2016; Nishimura et al., 2017). This indicates that virus-
74 specific NAbs not only confer sterile protection but also can evoke T-cell-mediated non-sterile
75 viral control, suggesting the importance of endogenous NAb responses supported by humoral-
76 cellular response synergisms, during an optimal time frame. Therefore, identifying
77 mechanisms driving NAb induction against such viruses is an important step to eventually
78 design NAb-based HIV control strategies.

79 One approach that can provide important insights into this goal is analysis of *in vivo*
80 immunological events linked with NAb induction against difficult-to-neutralize SIVs in a non-
81 human primate model. Various *in vivo* signatures of HIV-specific NAb induction, such as
82 antibody-NAb coevolution (Moore et al., 2012), autoimmune-driven induction (Moody et al.,
83 2016) and natural killer cell-related host polymorphisms (Bradley et al., 2018) have been
84 reported to date. The broad range of contributing factors collectively, and interestingly,
85 indicates that pathways to NAb induction against difficult-to-neutralize viruses including
86 HIV/SIV are redundant, and may potentially involve as-yet-unknown mechanisms driving NAb
87 induction. For example, the neutralization resistance of certain SIV strains does not appear to
88 be explained by any of the aforementioned, posing SIV models as attractive tools to analyze
89 NAb induction mechanisms.

90 In the present study, we examined virus-specific antibody responses in rhesus
91 macaques infected with a highly difficult-to-neutralize SIV strain, SIV_{mac239}. This virus is
92 pathogenic in rhesus macaques causing simian AIDS across a broad range of geographical
93 origin of macaques (Cumont et al., 2008). Macaques infected with SIV_{mac239} show persistent
94 viremia and generally lack NAb responses throughout infection (Kestler et al., 1991; Nomura
95 et al., 2012). In this study, a large-scale screening of SIV_{mac239}-infected Burmese rhesus
96 macaques for up to 100 weeks identified a subgroup inducing NAbs in the chronic phase.
97 Interestingly, before NAb induction, these animals commonly selected for a specific $CD8^+$
98 cytotoxic T lymphocyte (CTL) escape mutation in the viral Nef-coding gene. Compared with
99 wild-type (WT) Nef, this mutant Nef manifested a decrease in aberrant interaction with
100 phosphoinositide 3-kinase (PI3K)/mammalian target of rapamycin complex 2 (mTORC2),

101 resulting in decreased downstream hyperactivation of the canonical B-cell negative regulator
102 Akt (Omori et al., 2006; Limon et al., 2014). Machine learning-assisted imaging cytometry
103 revealed that Nef preferentially targets Env-specific B cells *in vivo*. Furthermore, the NAb
104 induction was linked with sustained Env-specific B-cell responses after or during the mutant
105 Nef selection. Thus, NAb induction in SIV_{mac239}-infected hosts conceivably involves a
106 functional boosting of B cells that is phenotypically reciprocal to a recently found human PI3K
107 gain-of-function and antibody-dysregulating inborn error of immunity (IEI), activated PI3 kinase
108 delta syndrome (APDS) (Angulo et al., 2013; Lucas et al., 2014). Our results suggest that
109 intervening PI3K/mTORC2 signaling can potentially result in harnessing NAb induction against
110 difficult-to-neutralize viruses.

111 **Results**

112

113 **Identification of macaques inducing SIV_{mac239}-neutralizing antibodies**

114 We performed a retrospective antibody profile screening in rhesus macaques infected
115 with NAb-resistant SIV_{mac239} (*n* = 70) (**Figure 1A**) and identified a group of animals inducing
116 anti-SIV_{mac239} NAb responses (*n* = 9), which were subjected to characterization. These NAb
117 inducers showed persistent viremia with no significant difference in viral loads compared with
118 a subgroup of NAb non-inducers (*n* = 19) that were previously profile-clarified, naïve and major
119 histocompatibility complex class I (MHC-I) haplotype-balanced (used for comparison
120 hereafter) (**Figure 1B** and **Figure 1-figure supplement 1**). Plasma SIV_{mac239}-NAb titers
121 measured by 10 $TCID_{50}$ SIV_{mac239} virus-killing assay showed an average maximum titer of 1:16,
122 being induced at an average of 48 weeks post-infection (p.i.) (**Figure 1C**). Two of the nine
123 NAb inducers showed detectable NAb responses by 24 weeks p.i., while the remaining seven
124 induced NAbs after 30 weeks p.i. Anti-SIV_{mac239} neutralizing activity was confirmed in
125 immunoglobulin G (IgG) purified from plasma of these NAb inducers (**Figure 1-figure**
126 **supplement 2**). SIV Env-binding IgGs developed from early infection in both NAb inducers
127 and non-rapid-progressing NAb non-inducers, the latter differing from rapid progressors
128 known to manifest serological failure (Hirsch et al., 2004; Nakane et al., 2013) (**Figure 1-**
129 **figure supplement 3A**). Titers of Env-binding IgG were not higher but rather lower at year 1
130 p.i. in the NAb inducers (**Figure 1-figure supplement 3B** and **3C**). This was consistent with
131 other reports (Havenar-Daughton et al., 2016) and differing with gross B-cell enhancement in
132 Nef-deleted SIV infection with enhanced anti-SIV binding antibody titers accompanying
133 marginal neutralization (Adnan et al., 2016). NAb inducers and non-inducers showed similar
134 patterns of variations in viral *env* sequences (Burns et al., 1993), mainly in variable regions 1,
135 2 and 4 (V1, V2 and V4) (**Figure 1-figure supplement 4**).

136

137 **Selection of a viral *nef* mutation (Nef-G63E) precedes chronic-phase SIV_{mac239}-specific**
138 **NAb induction**

139 To explore viral mutations linked to NAb induction, we assessed viral nonsynonymous
140 polymorphisms outside *env*. Strikingly, we found selection of a viral genome mutation resulting
141 in G (glycine)-to-E (glutamic acid) substitution at residue 63 of Nef (Nef-G63E) in seven of the
142 nine NAb inducers (**Figure 2A**). Two inducers that did not select Nef-G63E were the early
143 inducers detected for NAb positivity before 24 weeks p.i. This 63rd residue lies in the
144 unstructured N-terminus of Nef, flanked by two α-helices conserved in SIVmac/SIVsmm
145 (**Figure 2B**). This region is generally polymorphic among HIV-1/HIV-2/SIV, occasionally being
146 deleted in laboratory and primary isolate HIV-1 strains (Geyer et al., 2001). AlphaFold2-based
147 structure prediction did not derive palpable change except for low-probability disruption of the
148 alpha helices (data not shown). This mutation was found only in two of the nineteen NAb non-
149 inducers, including one rapid progressor (**Figure 1-figure supplement 1**) and selection was
150 significantly enriched in the NAb inducers as compared to the nineteen non-inducers (**Figure**
151 **2C**). Analysis of Nef-G63E mutation frequencies in plasma viruses showed that Nef-G63E
152 selection preceded or at least paralleled NAb induction (**Figure 2D**).
153
154 **Nef-G63E is a CD8$^+$ T-cell escape mutation**
155 To explore the mechanistic link between Nef-G63E selection and NAb induction, first we
156 assessed whether CD8$^+$ T-cell responses target this region. We found that these seven NAb
157 inducers selecting this mutation elicited CD8$^+$ T-cell responses specific for a 9-mer peptide
158 Nef$_{62–70}$ QW9 (QGQYMNTPW) (**Figure 3A**). This Nef$_{62–70}$ QW9 epitope is restricted by MHC-
159 I molecules Mamu-B*004:01 and Mamu-B*039:01 (Evans et al., 1999; Sette et al., 2012).
160 Possession of these accounted for six cases of Nef-G63E selection (**Figure 3A**), and the
161 remaining one animal possessed Mamu-A1*032:02 predicted to bind to Nef$_{63–70}$ GW8
162 (NetMHCpan). Ten of nineteen NAb non-inducers also had either of these alleles (**Figure 1-**
163 **figure supplement 1**). This did not significantly differ with the NAb inducer group (P = 0.25
164 by Fisher's exact test, data not shown), indicating that NAb induction was not simply linked
165 with possession of these MHC-I genotypes but instead required furthermore specific selection
166 of the Nef-G63E mutation (**Figure 2C**). Nef-G63E was confirmed to be an escape mutation

167 from Nef_{62-70}-specific $CD8^+$ T-cell responses (**Figure 3B**). NAb non-inducers possessing these
168 alleles elicited little or no Nef_{62-70}-specific $CD8^+$ T-cell responses (**Figure 3-figure supplement**
169 **1A**), suggesting that *in vivo* selection and fixation of this Nef-G63E SIV was indeed Nef_{62-70}-
170 specific $CD8^+$ T cell-dependent. Replication of SIV carrying the Nef-G63E mutation was
171 comparable with WT on a cynomolgus macaque HSC-F $CD4^+$ T-cell line (Akari et al., 1996),
172 excluding the possibility that the mutation critically impairs viral replication (**Figure 3-figure**
173 **supplement 1B**), and plasma viral loads were comparable between Nef-G63E mutant-
174 selecting NAb inducers versus non-inducers (**Figure 3-figure supplement 1C**). These results
175 indicate NAb induction following *in vivo* selection and fixation of the $CD8^+$ T-cell escape *nef*
176 mutation, Nef-G63E under viral persistence.
177
178 **G63E mutation reduces aberrant Nef interaction-mediated drive of PI3K/mTORC2**
179 We next focused on the functional phenotype of Nef-G63E mutant SIV in infected cells.
180 An essence of host perturbation by Nef is its wide-spectrum molecular downregulation,
181 ultimately facilitating viral replication (Schindler et al., 2004; Zhang et al., 2009). To evaluate
182 possible amelioration of this property, we compared downregulation of major targets CD3,
183 CD4, MHC-I, CXCR4 and BST-2 (Jia et al., 2009) in infected HSC-F cells. Nef-G63E mutation
184 did not confer notable change compared with WT [*P* = not significant (*n.s.*) for all molecules,
185 data not shown], implicating other non-canonical changes (**Figure 4A**). One report suggested
186 Nef to drive macrophage production of soluble ferritin and perturb B cells, with its plasma level
187 correlating with viremia (Swingler et al., 2008). Here, plasma ferritin levels showed no
188 differences (**Figure 4-figure supplement 1A**) and viral loads were comparable as
189 aforementioned between Nef-G63E-selecting NAb inducers and non-inducers, arguing
190 against gross involvement of ferritin as well as other viral replication-related Nef phenotypes
191 at least in this model.
192 Next, we elucidated immunosignaling-modulating properties of Nef-G63E SIV. Akt is
193 known as the predominant immune-intrinsic negative brake of B-cell maturation and
194 AFC/antibody responses *in vivo* (Omori et al., 2006; Limon et al., 2014; Fruman et al., 1999;

195 Ray et al., 2015; Sander et al., 2015). Thus, we analyzed Akt phosphorylation on day 3 after
196 Nef-G63E SIV infection at low multiplicity of infection (MOI). This analysis revealed that its
197 serine 473-phosphorylated form (pAkt Ser473), non-canonically known for Nef-mediated
198 upregulation (Kumar et al., 2016), was significantly lower in Nef-G63E mutant-infected cells
199 compared with WT (**Figure 4B**). The difference observed here was more pronounced than
200 histogram deviation levels in PI3K gain-of-function mice with full recapitulation of B-
201 cell/antibody-dysregulating human APDS disease phenotype (Avery et al., 2018). In contrast,
202 the threonine 308-phosphorylated Akt (pAkt Thr308) level remained unaffected (**Figure 4-**
203 **figure supplement 1B**).
204 Interestingly, external PI3K stimuli by serum starvation (Kennedy et al., 1997)
205 accelerated phenotype appearance from day 3 to day 1 post-infection (**Figure 4C**, left). A
206 similar trend was obtained by short-term PI3K stimulation with interferon-γ (Nguyen et al.,
207 2001), interleukin-2 (Marzec et al., 2008) and SIV Env (François & Klotman, 2003) (**Figure 4-**
208 **figure supplement 1C**). A high-MOI SIV infection, comprising higher initial concentration of
209 extracellular Env stimuli, also accelerated phenotype appearance from day 3 to day 1 post-
210 infection, with stronger pAkt reduction (**Figure 4C**, right). These data indicate that the Akt-
211 inhibitory G63E mutant Nef phenotype is PI3K stimuli-dependent. Transcriptome analysis
212 signatured decrease in PI3K-pAkt-FoxO1-related genes in mutant SIV infection (**Figure 4-**
213 **figure supplement 1D**). Given that Akt is also a survival mediator, Nef-G63E mutation may
214 be Th-cytopathic and decrease Th dysfunctional expansion (Baumjohann et al., 2013), as had
215 been observed in LCMV strain WE (Recher et al., 2004) and chronic HIV/SIV (Gray et al.,
216 2011; Lindqvist et al., 2012; Petrovas et al., 2012) infections. Here, reduced chronic-phase
217 peripheral $CXCR3^{-}CXCR5^{+}PD\text{-}1^{+}$ memory follicular Th (Tfh), linked with antibody cross-
218 reactivity in one cohort (Locci et al., 2013), was somewhat in line with this notion (**Figure 4-**
219 **figure supplement 1E** and **1F**). We additionally examined another CTL escape mutant Nef-
220 G63R, selected with marginal statistical significance primarily in early stage (**Figure 4-figure**
221 **supplement 2A**). This mutant did not associate with NAb induction in one control animal (R06-
222 034) even upon preferential selection (**Figure 4-figure supplement 2B**) and Nef-G63R

223 mutant was not similarly decreased in pAkt drive (**Figure 4-figure supplement 2C**),
224 implicating that the Nef-G63E mutation was more tightly linked with NAb induction in terms of
225 an immunosignaling phenotype.

226 We further explored molecular traits of this decreased Akt hyperactivation. We reasoned
227 that comparing endogenous Nef binding patterns would be adequate and analyzed SIV-
228 infected HSC-F cells with a flow cytometry-based proximity ligation assay (PLA) (Leuchowius
229 et al., 2009; Avin et al., 2017). We found that this Nef-G63E mutation causes significant
230 decrease in Nef binding to PI3K p85/p110α and downstream mTORC2 components mTOR
231 (Sarbassov et al., 2005) and GβL/mLST8 (Kim et al., 2003) in the $CD4^{lo}$-SIV Gag $p27^{+}$ infected
232 population (**Figure 4D**). Results were biochemically confirmed by a decrease in G63E-
233 mutated Nef binding to the mTORC2-intrinsic cofactor Sin1 in coimmunoprecipitation analysis
234 of infected HSC-F cells (**Figure 4E**). Collectively, the Nef-G63E mutation attenuates
235 PI3K/mTORC2 signaling driven by aberrant Nef bridging, explaining decreased Akt Ser473
236 phosphorylation by mTORC2. These properties were in keeping with more pronounced
237 apoptosis of CD4-downregulated/infected HSC-F cells upon Nef-G63E SIV infection (**Figure**
238 **4F**). Thus, Nef-G63E SIV is a mutant virus decreased in aberrant interaction/drive of B-cell-
239 inhibitory PI3K/mTORC2 signaling, manifesting a molecular signature reciprocal to human
240 APDS (Angulo et al., 2013; Lucas et al., 2014; Avery et al., 2018).

241

242 **Targeting of lymph node Env-specific B cells by Nef *in vivo***

243 Next, we analyzed *in vivo* targeting of virus-specific B cells by Nef in lymph nodes to
244 explore the potential B-cell-intrinsic influence of the Nef-G63E phenotype. Previously
245 suggested influence of soluble Nef itself (Qiao et al., 2006) and/or related host factors
246 (Swingler et al., 2008) may derive generalized negative influence on B cells. However, SIV
247 antigen-specific binding antibody responses were rather decreased in NAb inducers (**Figure**
248 **1-figure supplement 1**), with comparable viral loads (**Figure 3-figure supplement 1C**) and
249 ferritin levels (**Figure 4-figure supplement 1A**), differing from the aforementioned literature
250 stating positive correlation between the three. We surmised that some targeted Nef intrusion

251 against Env-specific B cells may be occurring and that the decreased aberrant drive of Nef-
252 PI3K/mTORC2 may result in their enhanced maturation in lymph nodes.

253 While reports (Xu et al., 2009) histologically proposed Nef B-cell transfer, quantitative
254 traits, e.g., invasion frequency and influence on virus-specific B cells, have remained unvisited.
255 One of the reasons is that intracellular Nef staining is dim (particularly for B cell-acquired Nef)
256 and difficult to examine by conventional flow cytometry. To circumvent this issue, defining
257 staining cutline using single-cell images potentially overcomes confounding technical hurdles,
258 such as high Nef false-staining signals owing to pre-permeation rupture and post-permeation
259 processing that derives biologically discontinuous staining and/or batch-inflated signals. Thus,
260 we reasoned that at the expense of spatial information, sophisticating imaging cytometry
261 would best visualize Nef-mediated B-cell perturbation *in vivo*. We analyzed lymph node B cells
262 with Image Stream X MKII, with high-power (> 10-fold) antigen detection [e.g., molecules of
263 equivalent soluble fluorochrome (MESF) 5 *vs.* MESF 80 in an average flow cytometer for FITC
264 detection] ideal for detection/single-cell verification.

265 We designed a triple noise cancellation strategy to overcome the issues stated above.
266 Firstly, amine reactive dye staining (Perfetto et al., 2006) gated out B cells being Nef-positive
267 due to pre-experimental membrane damage (**Figure 5-figure supplement 1A**, left). Next, we
268 deployed secondary quantitative parameters of Nef signals deriving from each pixel of the
269 images. Generation of a gray-level cooccurrence matrix (GLCM) (Haralick et al., 1973), which
270 computes adjacent signal deviation as their frequencies on a transpose matrix, enables
271 calculation of a variety of feature values summarizing traits of the whole image. A biological
272 assumption of Nef signal continuity in a true staining suggested that the sum of weighted
273 square variance of GLCM, i.e., the {sum of [square of (value – average signal strength) ×
274 frequency of each value occurrence]} would separate natural versus artificial Nef signals. This
275 value, known as Haralick variance, was computed for multiple directions and averaged. The
276 resultant Haralick variance mean (**Figure 5-figure supplement 1A**, X axis) is proportionate
277 with unnaturalness of signals in the Nef channel. Finally, Nef signal intensity threshold (**Figure
278 5-figure supplement 1A**, Y axis) gated out overtly-stained cells void for true-false verification.

279 These measures excluded B cells with non-specific, strong-signal binary-clustered staining
280 pixels for Nef (deriving a large summated variance: X axis, and/or batch-stained for Nef: Y
281 axis; likely originating from post-experimental membrane damage).

282 Using this approach, we successfully acquired images of viable Nef$^+$CD19$^+$ B cells with
283 low Nef signal Haralick variance mean and low Nef signal intensity threshold, with fine-textured
284 gradation of low-to-intermediate Nef staining with continuity from membrane-proximal regions
285 and without sporadic staining speckles (**Figure 5A** and **Figure 5-figure supplement 1**).
286 Scoring segregation of typical void/valid images by a linear discriminant analysis-based
287 machine learning module showed that this gating provides the highest two-dimensional
288 separation (**Figure 5-figure supplement 1**). Combined with visualization of Env-binding B
289 cells, we reproducibly obtained images of Env-specific (Ch 12) CD19$^+$ (Ch 11) B cells without
290 membrane ruptures (Ch 08) and showing fine-textured transferred Nef (Ch 02) (**Figure 5B**).
291 Nef invasion upregulated pAkt Ser473 (Ch 03) to a range resembling *in vitro* analysis (**Figure**
292 **5C**), demonstrating that Nef-driven aberrant PI3K/mTORC2 signaling does occur in Nef-
293 invaded B cells *in vivo*. Strikingly, lymph node Env-specific B cells showed significantly higher
294 Nef-positive frequencies as compared with batch non-Env-specific B cells (**Figure 5D**). This
295 indicated that infected cell-derived Nef preferentially targets adjacent Env-specific B cells,
296 putatively through its contact/transfer from infected CD4$^+$ cells to B cells (Xu et al., 2009;
297 Hashimoto et al., 2016). Thus, the phenotypic change in Nef can directly dictate Env-specific
298 B-cell maturation.

299

300 **Cell contact-dependent B-cell invasion from infected cells *in vitro***

301 To understand cell-intrinsic properties enhancing B-cell Nef acquisition *in vivo*, we
302 addressed in an *in vitro* coculture reconstitution how infected cell-to-B-cell Nef invasion takes
303 place and how it is modulated. We performed imaging cytometry on a twelve-hour coculture
304 of SIV-disseminating HSC-F cells (reaching around 30% Nef-positivity at moment of coculture)
305 with Ramos B cells, with or without modulators added throughout the coculture period (**Figure**
306 **6A**, top left). In this coculture, there is no MHC-related interaction known to enhance T-cell/B-

307 cell contact (Wülfing et al., 1998). Machine learning-verified noise cancellation of fragmented
308 signal acquisition (**Figure 6A**, middle left) filtered reproducible images of Nef-positive HSC-F
309 cells directly adhering to Ramos B cells within the doublet population (**Figure 6A**, top to middle
310 right). Importantly, addition of soluble, stimulation-competent antibodies against macaque
311 CD3 enhanced adhesion of Nef^{+} T cells to B cells (**Figure 6A**, bottom center). In these
312 doublets, we readily detected images of polarized Nef protrusion/injection from T cells to B
313 cells (second column, filled wedges) as well as trogocytosed B-cell membranes (third column,
314 open wedge), suggesting dynamic Nef acquisition by B cells. Changing centrifugation
315 strengths upon coculture collection and staining (190 x *g* versus 1,200 x *g* and 600 x *g* versus
316 1,200 x *g*, respectively) shifted the tendency between enriched Nef^{+} HSC-F-B-cell doublet
317 versus singlet detection via CD3 stimulation, respectively (**Figure 6A**, lower right).
318 Substantiated by the acquired images, an enhancement of live singlet Ramos B-cell Nef
319 acquisition (% Nef^{+} in total B cells) was also observed by CD3 stimulation in conventional flow
320 cytometry (**Figure 6B**). There was a similar enhancement when we added phytohemagglutinin
321 (PHA) whereas phorbol-12-myristate-13-acetate (PMA)/ionomycin did not affect Nef
322 acquisition by B cells. In a similar 72-hour static coculture with primary CD20^{+} B cells, we
323 detected recapitulation of the decreased B-cell pAkt Ser473 phosphorylation upon G63E Nef
324 transfer compared to that of WT Nef (**Figure 6C**), indicating that the Nef-G63E mutation can
325 directly alleviate maturation inhibition in preferentially Nef-targeted Env-specific B cells.
326
327 **Enhanced Env-specific B-cell responses after PI3K-diminuting mutant selection**
328 Finally, to assess *in vivo* B-cell quality in NAb inducers with Nef-G63E mutant selection,
329 we examined peripheral SIV Env-specific IgG^{+} B-cell responses comprising plasmablasts
330 (PBs) and memory B cells (B_{mem}). After excluding lineage-specific cells [T/NK/pro-B
331 cells/monocytes/myeloid dendritic cells (DCs)/plasmacytoid DCs], we defined IgG^{+} PBs as
332 showing: high replication (Ki-67^{+}), post-activation (HLA-DR^{+}), transcriptional switching for
333 terminal differentiation (IRF4^{hi}) and downregulated antigen surface binding (surface [s]Env^{lo}-
334 cytoplasmic [Cy]Env^{+}) (Nutt et al., 2015; Silveira et al, 2015) (**Figure 7A** and **Figure 7-figure**

335 **supplement 1**). NAb inducers showed significantly higher Env-specific IgG$^+$ PB responses
336 around week 30 p.i., after Nef-G63E selection, compared to those in NAb non-inducers
337 (**Figures 7B** and **7C**). At 1 year, this difference became enhanced as a result of less
338 pronounced decrease in Env-specific PB frequencies in the NAb inducers.

339 Simultaneous quantification of Env-specific PB and IgD$^-$CD27$^+$IgG$^+$ B_{mem} responses
340 allowed for an assessment of overall B-cell response quality by pair-wise analysis of Env-
341 specific IgG$^+$ B_{mem}/PB as a projection of germinal center (GC) output (Zotos et al., 2010)
342 (**Figure 7D**, left). In this two-dimensional vector temporally plotting the frequency of B_{mem} and
343 PBs, vector protrusion towards upper right represents higher gross GC output of antibody-
344 forming cells (AFCs). In NAb non-inducers, all vectors converged on an empirically defined
345 polygonal attractor area D_n (gray area surrounded with dotted lines in **Figure 7D**, right) at year
346 1 p.i. and beyond, describing that these NAb non-inducers failed to sustain Env-specific GC
347 output. In contrast, the vectors were consistently tracked outside D_n in the NAb inducers with
348 Nef-G63E (**Figure 7D**). At the time of NAb induction, they converged on another upper-right
349 GC output attractor area D_i (red area surrounded with dotted lines in **Figure 7D**, right) that is
350 mutually exclusive with D_n ($P < 0.0001$ by Fisher's exact test on NAb non-inducer/inducer
351 vector distribution frequency within D_n). These suggest more robust virus-specific IgG$^+$ B-cell
352 responses following Nef-G63E CD8$^+$ T-cell escape mutant selection, ultimately leading to NAb
353 induction. The enhanced signature of cognate B-cells was also an inverted pattern of impaired
354 terminal differentiation of B-cell responses in APDS (Al Qureshah et al., 2021).

355 Taken together, in the current model, Nef_{62-70}-specific CD8$^+$ T-cell responses in
356 persistently SIV_{mac239}-infected macaques selected for an escape mutant, Nef-G63E, which
357 displays attenuated aberrant Nef binding and ensuing drive of B-cell-inhibitory PI3K/mTORC2.
358 Nef invasion of B cells *in vivo* occurred more preferentially in Env-specific B cells, suggesting
359 diminution in Nef-mediated tonic dysregulation of B cells after mutant selection. These events
360 conceivably predisposed to enhanced Env-specific B-cell responses and subsequent
361 SIV_{mac239}-specific NAb induction, altogether, in a manner reciprocal to human APDS-mediated
362 immune dysregulation.

363 **Discussion**

364

365 In the present study, we found that in macaques infected with an NAb-resistant SIV,
366 selection of a $CD8^+$ T-cell escape *nef* mutant virus, Nef-G63E, precedes NAb induction. As a
367 result, Nef binding-mediated drive of PI3K/mTORC2 in Env-specific B cells becomes
368 attenuated, which in turn unleashes maturation of antiviral B-cell responses *in vivo* to induce
369 NAbs. Importantly, this manifested through a pAkt deviation level more pronounced than WT
370 versus germline *PIK3CD* gain-of-function mutation heterozygote mice recapitulating full
371 human APDS phenotype (Avery et al., 2018). Thus, the current Nef-G63E-associated B-
372 cell/NAb phenotype likely occurs in a "reciprocal APDS-like" manner. This proposition was
373 enhanced based on extension of immune cell-intrinsic Nef influence on cognate B cells (Fig.
374 5), in addition to infected T cells. This work is, to our knowledge, the first to interlink a
375 PI3K/mTORC2-modulating viral signature and enhanced B-cell/NAb responses in a viral
376 infection model.

377 A link between viral T-cell escape and consequent immune modulation has been
378 previously explored to some extent. For example, enhanced binding of mutant HIV-1 epitope
379 peptide to inhibitory MHC-I on DCs impairs T cells (Lichterfeld et al., 2007) and decreased
380 CTL-mediated lymph node immunopathology can drive, and not inhibit, the production of
381 LCMV-specific antibodies (Battegay et al., 1993). Our results now evidence a new pattern of
382 NAb responses that are bivalently shaped through viral interactions with both humoral and
383 cellular immunity in AIDS virus infection. SIV_{mac239} infection of macaques possessing MHC-I
384 alleles associated with Nef-G63E mutation can be one unique model to analyze virus-host
385 interaction for B cell maturation leading to NAb induction. The interval between Nef-G63E
386 mutant selection and NAb induction was variable in the NAb inducers, for which we did not
387 obtain a clear explanation. This may be influenced by certain basal competitive balance
388 between humoral versus cellular adaptive immunity, as observed in certain vaccination
389 settings (Querec et al., 2009).

390 The current Nef-G63E phenotype identified here adds yet another aspect to the wealth

391 of evidence documenting the multifaceted impact of Nef in HIV/SIV infection (Kirchhoff et al.,
392 1995; Gauduin et al., 2006; Stolp et al., 2012). Based on our data, the current phenotype
393 differed from decreased replication-related properties or generalized amelioration in immune
394 impairment such as those of delta-Nef HIV/SIV (Kirchhoff et al., 1995; Johnson et al., 1997;
395 Gauduin et al., 2006; Fukazawa et al., 2012). The SIV Nef N-terminal unstructured region
396 comprising Nef-G63E is not conserved in HIV-1 (Schindler et al., 2004) and beyond this model
397 study it remains to be addressed whether a mutant HIV-1 with a similar immunosignaling-
398 related phenotype can be obtained and how much lentiviral conservation exists for such
399 interactions. Analysis of cognate B-cell maturation on cohort basis (Hau et al., 2022) may
400 potentially assist this approach.

401 Preferential Nef transfer to Env-specific B cells (**Figure 5**) suggests potential
402 involvement of polarized perturbation in cognate immune cells *in vivo*, which was best depicted
403 for preferential infectivity of HIV-specific $CD4^+$ T cells (Douek et al., 2002) and HIV
404 condensation to the interface of dendritic cell-T-cell contacts (McDonald et al., 2003). As
405 cognate MHC class II interactions (Wülfing et al., 1998; Giltin et al., 2014) regularly occur
406 between HIV/SIV-specific $CD4^+$ T cells and Env-specific B cells in GCs, dysregulation of Env-
407 specific B cells may well result from hijacking of cognate T-cell/B-cell interactions by the virus.
408 Enhanced T-cell attachment and transfer of Nef to B cells by TCR stimulation (**Figure 6**) may
409 override constraints of infection-mediated $CD4^+$ T-cell cytoskeletal impairment (Campbell et
410 al., 2004; Jolly et al., 2004; Stolp et al., 2009) particularly by antagonizing reduced motility
411 (Stolp et al., 2012), resulting in *in vivo* “filtering” of enhanced cognate $CD4^+$ T-cell interaction
412 with cognate B cells. Interestingly, Tfh cells that bear trogocytosed CD20 and are positive for
413 viral DNA appear *in vivo* during SIV infection and increase when infection progresses (Samer
414 et al., 2023). This is consistent with our data that suggest occurrence of contact-dependent,
415 polarized interactions facilitating Nef transfer to cognate B cells.

416 The major *in vivo* readout of this study is autologous neutralization of a highly difficult-
417 to-neutralize SIV strain, which is different from HIV-specific broadly neutralizing antibodies
418 (bNAbs). Importantly, however, obtained signatures of enhanced IgG^+ Env-specific AFC and

419 B cells (class switch/terminal differentiation) and virus neutralization (hypermutation) in our
420 model are indicative of elevated activity of activation-induced cytidine deaminase (AID), the
421 canonical positive driver of B-cell fate. Thus, we reason that findings in this study have a strong
422 conceptual continuity with bNAb regulation by AID in HIV infection.

423 Our results extracted an *in vivo* link between a decrease in aberrant Nef-PI3K/mTORC2
424 interaction and major enhancement in B-cell responses. The relationship is reciprocal to
425 immunogenetic mechanisms of human PI3K gain-of-function mutations resulting in APDS with
426 multiply impaired anti-viral B-cell responses. APDS occurs from germline mutations in
427 leukocyte-intrinsic p110δ catalytic subunit-coding *PIK3CD* or the ubiquitous p85α regulatory
428 subunit-coding *PIK3R1*. In both cases, the mutations cause residue substitutions resulting in
429 class IA PI3K gain-of-function (Dornan et al., 2017). Hyperactivated PI3K interferes with
430 cognate B cells in an immune cell-intrinsic manner, leading to impaired B-cell class switching
431 and resultant susceptibility against various infections (Angulo et al., 2013; Lucas et al., 2014;
432 Coulter et al., 2017). In the current work, we conversely document a decrease in virally
433 induced tonic PI3K drive, enhanced IgG class-switched cognate B-cell responses and NAb
434 induction against a notably difficult-to-neutralize SIV. The exact hierarchy of binding between
435 Nef and PI3K/mTORC2 components (including PI3K isoforms) and its alteration by Nef-G63E
436 mutation remains to be investigated. Yet PI3Kp85 showed the strongest Nef-binding index in
437 PLA assay (**Figure 4D**) presumably because of the SH3-binding PxxP domain in Nef which
438 binds the SH3 domain of PI3Kp85 (Rickles et al., 1994). Decreased binding of Nef to its
439 canonical target PI3Kp85 may precipitate into attenuated interactions of Nef with quintuple
440 PI3K/mTORC2, resulting in fragile downstream Akt signaling. Such domino-triggering is also
441 observed in APDS patients, from gain-of-function mutant p85 to p110 (Dornan et al., 2017),
442 which similarly illustrates the fine-tuned nature of the PI3K/mTORC2/Akt signaling pathway.

443 A limitation of this study is the use of retrospective samples, posing constraints for
444 detecting exact temporal changes in tonic viral B-cell perturbation. Related with this, it was not
445 attainable to optimally time the sampling of lymph node cells in animals belonging to the
446 subgroup of interest. Certain plasma and cellular samples were also unavailable in differing

447 experiments. While partially addressed in *in vitro* reconstitution, much remains to be
448 investigated for the observed polarity of Env-specific B-cell perturbation *in vivo*. Similarly,
449 influence of the Nef-G63E phenotype on $CD4^+$ T cells *in vivo* and its consequence on B-cell
450 modulation remains largely elusive, and in the current work we focused mainly on molecular
451 properties of the NAb-correlating Nef-G63E mutant strain. HIV/SIV infection uniquely shows a
452 biphasic Tfh dysregulation of acute-phase destruction (Mattapallil et al., 2005; Moukambi et
453 al., 2015; Moukambi et al., 2019) followed by dysregulated chronic-phase hyper-expansion
454 (Lindqvist et al., 2012; Petrovas et al., 2012; Cubas et al., 2013; Xu et al., 2015). Further
455 studies are therefore warranted to uncover how the Nef mutant, which is proapoptotic and
456 displays ameliorated PI3K drive, influences Tfh responses at different phases of the infection.
457 Gain-of-function mutations in PI3K-encoding genes appear to affect B cells more strongly
458 (Asano et al., 2018). Nonetheless, it is noteworthy that they also evoke basal dysregulation in
459 peripheral $CD4^+$ T cells, which locally recapitulates dysregulation and death of HIV/SIV-
460 infected $CD4^+$ T cells, highlighting the importance of PI3K-mediated signaling in HIV/SIV
461 infection. In any event, we surmise that specific animal models like the current one help to
462 depict a temporal cascade of *in vivo* events leading to NAb induction, assisting human
463 immunology. As an extension of this study extracting the NAb-involved molecular axis,
464 manipulation/reconstitution experiments shall be designed.

465 In conclusion, we demonstrated in a non-human primate AIDS model that NAb induction
466 against a difficult-to-neutralize SIV strain occurs after selection of a $CD8^+$ T-cell escape variant
467 with a reduced ability to drive excess PI3K/mTORC2 signaling. These results collectively offer
468 an example of how NAb responses against immunodeficiency viruses can be shaped by both
469 wings of adaptive immune pressure. Given the key role for Nef-mediated perturbation of
470 PI3K/mTORC2 in NAb resistance, immune cell-intrinsic PI3K/mTORC2 manipulation may
471 offer a new possibility to harness antiviral NAb responses. As human IEIs are increasingly
472 becoming discovered with various immune-perturbing phenotypes and inheritance patterns
473 (Jauch et al., 2023), search of other types of analogies between viral immune dysregulations
474 and human IEIs may fuel the discovery of novel targets to modulate and harness immune

475 responses in translational settings.

476

Acknowledgments

This work was supported by Japanese Initiative for Progress of Research on Infectious Diseases for Global Epidemic (J-PRIDE) (JP19fm0208017 to H.Y.), Japan Program for Infectious Diseases Research and Infrastructure (Interdisciplinary Cutting-edge Research) (JP22wm0325006 to H.Y.), Research Programs on HIV/AIDS, Emerging and Re-emerging Infectious Diseases, and Global Health Issues (JP20fk0410022 and JP24fk0410066 to H.Y.; JP18fk0410003, JP20fk0410011, JP20fk0108125, JP20jm0110012, JP21fk0410035, and JP21jk0210002 to T.M.) from Japan Agency for Medical Research and Development, the Ministry of Education, Culture, Sports, Science, and Technology in Japan ([JSPS] KAKENHI Grants 17H02185, 18K07157 and 24K21287 to H.Y.; 21H02745 to T.M.), the Takeda Science Foundation (to H.Y.), the Imai Memorial Trust for AIDS Research (to H.Y.), and the Mitsui-Sumitomo Insurance Welfare Foundation (to H.Y.). We thank Fumiko Ono, Koji Hanari, Katsuhiko Komatsuzaki, Akio Hiyaoka, Hiromi Ogawa, Keiko Oto, Hirofumi Akari, Yasuhiro Yasutomi, Hiromi Sakawaki, Tomoyuki Miura and Yoshio Koyanagi for animal experiment assistance; Hiroyuki Kogure, Sayuri Seki and Julia R. Hirsiger for imaging cytometry technical assistance; Masako Nishizawa, Trang Thi Thu Hau, Shigeyoshi Harada, Takushi Nomura, Akiko Takeda, Taku Nakane, Nami Iwamoto, Taeko K. Naruse, Akinori Kimura and Mark S. de Souza for their help. H.Y. thanks Shoi Shi, Bettina Stolp, Jens V. Stein, Makoto Yamagishi and Yusuke Yanagi for conceptual discussions, and Jun Abe and Mike Recher for collaborative support.

Author Contributions

H.Y. conceived/designed/performed study and wrote manuscript; T.M. provided animal cohort, co-edited manuscript and co-directed study.

CRediT taxonomy:

Conceptualization: HY

Methodology: HY

Validation: HY

Formal analysis: HY

Investigation: HY

Resources: HY, TM

Data curation: HY

Writing—original draft: HY

Writing—review & editing: HY, TM

Visualization: HY

Supervision: HY, TM

Project administration: HY

Funding acquisition: HY, TM

Declaration of Interests

The authors declare no competing interests.

522 **Figure Legends**

523

524 **Figure 1. NAb induction against NAb-resistant SIV_{mac239}.**

525 **(A)** Study design.

526 **(B)** Plasma viral loads (SIV *gag* RNA copies/ml plasma) in NAb non-inducers (left) and

527 inducers (right).

528 **(C)** Plasma SIV_{mac239} 100% neutralizing end point titers by 10 $TCID_{50}$ killing assay on MT4-R5

529 cells. Points on the dotted line show marginally NAb-positive results (< 1:2). In some animals,

530 titers were comparable with our reported results using MT4 cells.

531

532 **Figure 2. Selection of a viral *nef* mutation (Nef-G63E) before NAb induction.**

533 **(A)** Viral *nef* mutations in NAb inducers. A linear schema indicating Nef functional domains is

534 aligned above. Mutations at timepoints with NAb^- (indicated by white wedge; mostly before 6

535 months p.i.), $NAb^{+/-}$ (green wedge) and NAb^+) (purple wedge; mostly after 1 year) are shown

536 in individual animals. Black and dark gray represent dominant and subdominant mutations (or

537 deletion in R-360) by direct sequencing, respectively. Red and pink indicate dominant and

538 subdominant G63E detection, respectively.

539 **(B)** Schema of SIV_{mac239} Nef structure and Nef-G63E mutation orientation.

540 **(C)** Comparison of frequencies of macaques having Nef-G63E in plasma viruses between

541 NAb non-inducers and inducers. Compared by Fisher's exact test.

542 **(D)** Temporal relationship of Nef-G63E frequencies in plasma virus and NAb induction. Black

543 boxes (left Y axis) show log_2 NAb titers; red triangles and blue diamonds (right Y axis) show

544 percentage of G63E and G63R mutations detected by subcloning (15 clones/point on average),

545 respectively.

546

547 **Figure 3. Nef-G63E is a $CD8^+$ T-cell escape mutation.**

548 **(A)** $Nef_{62–70}$ QW9-specific $CD8^+$ T-cell frequencies and related MHC-I alleles in seven NAb

549 inducers selecting Nef-G63E. Mamu-B*039:01 and Mamu-B*004:01 are known to restrict

550 $Nef_{62–70}$ QW9 epitope and binding of $Nef_{63–70}$ peptide to Mamu-A1*032:02 was predicted.

551 **(B)** $CD8^+$ T-cell responses specific to wild-type (WT) $Nef_{62–70}$ or mutant $Nef_{62–70}$.G63E or $Nef_{62–}$

552 $_{70}$.G63R peptides.

553

554 **Figure 4. Nef-G63E mutation reduces PI3K/mTORC2 binding and pAkt drive.**

555 **(A)** Representative surface expression level histograms of CD3, CD4, MHC class I, CXCR4

556 and BST-2 in $CD4^{lo}Nef^+$ subpopulations after WT or Nef-G63E mutant SIV infection at

557 multiplicity of infection (MOI) 0.1 on HSC-F cells.

558 **(B)** Left: representative histograms of relative pAkt serine (Ser) 473 levels in $p27^+$

559 subpopulations after WT or Nef-G63E mutant SIV infection at MOI 0.1 on HSC-F cells.

560 Numbers show pAkt Ser473 mean fluorescence intensities (MFIs) for each. Right: Deviation

561 of pAkt Ser473 MFIs in $p27^+$ HSC-F cells compared with mean MFI of uninfected cells.

562 Compared by unpaired t test.

563 **(C)** Left: Relative pAkt Ser473 levels (normalized to mean MFI of uninfected controls) in Nef^+

564 HSC-F cells assessed for serum starvation (MOI 0.2, 1 day p.i.). Adjusted *P* values show

565 results of comparison via Sidak's post-hoc test of 2-way ANOVA (C, left). Right: Deviation of

566 pAkt Ser473 MFIs in Nef^+ HSC-F cells assessed for high-MOI infection (MOI 5, 1-day p.i.).

567 Compared by unpaired t test.

568 **(D)** Proximity ligation assay (PLA) of Nef binding with mTOR, GβL/mLST8, PI3Kp85 and

569 PI3Kp110α. MFI-based binding index was calculated as (anti-Nef/anti-partner) - (isotype/anti-

570 partner) - (anti-Nef/isotype) + (isotype/isotype). Histograms for samples and isotype/isotype

571 are representatively shown. Differences in MFI binding indexes can be enhanced compared

572 with comparison of raw MFIs. Compared by paired t tests.

573 **(E)** Sin1 co-immunoprecipitation analysis of WT versus Nef-G63E mutant SIV-infected HSC-

574 F cells (infected at MOI 0.05, day 3). Immunoblotting of Nef (37 kDa) in whole cell lysates

575 (lanes 4-6) and anti-Sin1 antibody immunoprecipitates (lanes 1-3) are shown.

576 **(F)** Cell death frequencies of SIV-infected cells measured by Annexin V positivity (% of $CD4^{lo}$)

577 (infected at MOI 0.1, day 3). Compared by unpaired t test.

578 Data represent one of two [(A); (B); (C, right)] independent experiments in quadruplicate, four
579 independent experiments performed in triplicate [(C, left)], four independent single-well
580 comparison experiments pooled for statistical analysis (D), two experiments (E) or two
581 experiments performed with six wells/control (F). Bars: mean ± SD (B, C right), mean ± SEM
582 (C left, F).
583
584 **Figure 5. Preferential targeting of lymph node Env-specific B cells by Nef *in vivo*.**
585 **(A)** Representative gating of triple noise-cancellation *in vivo* Nef staining in B cells analyzed
586 by ImageStreamX MKII. Pre-experimental damaged cells are first excluded with Live/Dead
587 from focused/centroid/singlet image-acquired $CD19^+$ B cells (first lane right/R4 gated on
588 "Focused"). Following Nef^+ gating (second lane left/R5 gated on R4), a second step of Nef
589 noise cancellation (second lane middle/R7 on R5) comprises double-negative removal of post-
590 experimental stochastic irregular staining building a disparate intracellular staining gradient (X
591 axis, Nef signal pixel Haralick variance mean) and post-experimental batch overt cellular
592 staining (Y axis, Nef signal pixel intensity threshold). This outputs a B-cell population with a
593 fine-textured pericellular $Nef^{int\text{-}lo}$ staining, biologically concordant with Nef membrane-
594 anchoring. Probing of anti-Env BCR (αEnv) by recombinant SIV Env (second lane, right) is
595 combined, resulting in a 2-D panel of intracellular Nef versus αEnv for noise-cancelled Nef^+ B
596 cells (R7) plus Nef^- B cells (R8) (third lane left/"R7+R8"). pAkt Ser473 expression (third lane
597 right) and cellular morphology (B) was further analyzed. DN, double-negative.
598 **(B)** Typical images of Nef-transferred Env-specific B cells defined αEnv^+-intracellular Nef^+-Nef
599 Haralick variance $mean^{lo}$-Nef Intensity $threshold^{lo}$-$Live/Dead^-$-$CD19^+$ cells ["Nef^+aEnv^+"
600 population of lower left panel in (A), gated on "R7, R8"]. Note the pericellular pAkt Ser473
601 upregulation in these cells (Ch 03/yellow). Data on inguinal lymph node lymphocytes of
602 macaque R10-007 at week 62 post-SIV_{mac239} infection are shown in (A) and (B).
603 **(C)** Comparison of pAkt Ser473 median fluorescence (medFI) intensity levels in Nef^- B cells
604 (R8) versus noise-cancelled Nef^+ B cells (R7). Analyzed by paired t test.
605 **(D)** Comparison of Nef-positive cell frequencies in non-Env-specific (left) versus Env-specific

606 (right) B cells in lymph nodes of persistently SIV-infected macaques (*n* = 6). Analyzed by paired
607 t test.
608
609 **Figure 6. Contact-dependent enhancement of B-cell Nef acquisition in reconstitution.**
610 **(A)** Imaging flow cytometric analyses of stimuli-dependent enhancement of infected HSC-F
611 cell adhesion to non-permissive $CD19^+$ Ramos B cells with the indicated gating (left).
612 Cocultured doublet cells subjected to machine learning-verified filtration of fragmented signal
613 acquisition (via gating Nef pixel signal $contrast^{lo}$-Nef mean pixel per $object^{hi}$ cells) deriving
614 typical images of infected HSC-F cell (Nef stain shown in pale blue pseudocolor) adhesion to
615 Ramos cells (CD19 stain shown in purple pseudocolor) are shown. Analyzed by unpaired t
616 test for doublet formation in the unstimulated versus anti-CD3 monoclonal antibody (clone FN-
617 18)-stimulated group.
618 **(B)** Flow cytometric analyses of Nef-acquiring live $CD19^+$ Ramos B cells upon coculture with
619 SIV-infected HSC-F cells with or without the indicated stimuli. Analyzed by one-way ANOVA
620 with Tukey's post-hoc multiple comparison tests.
621 **(C)** Representative flow cytometric plot (left), histogram (middle) and pAkt Ser473 signal
622 deviation in WT versus G63E Nef-acquiring $CD20^+$ primary B cells (six wells/control). Analyzed
623 by unpaired t test. Data represent pooled data of two (A) or three [(B) and (C)] independent
624 experiments with indicated number of replicates showing similar results.
625
626 **Figure 7. Enhanced SIV Env-specific B-cell output up to NAb induction following Nef-**
627 **G63E selection.**
628 **(A)** Representative gating (R02-004, week 32 p.i.) of SIV Env gp140-specific memory B cells
629 (B_{mem}) and plasmablasts (PBs). Two panels for PB gating are shown in lower resolution for
630 visibility. B_{mem} staining was performed separately and gating are merged with PB panels
631 (second row, panels 2–4). For lineage-specific exclusion (first row, panel 4), CD10 was stained
632 independently for B_{mem} (see parenthesis).
633 **(B)** Changes in SIV Env gp140-specific plasmablast (PB) frequencies in viremic NAb non-

634 inducers (left, n = 12) and Nef-G63E-selecting NAb inducers (right, n = 6). Available samples
635 of twelve viremic NAb non-inducers (including ten with ≥ 1-year survival) and six NAb inducers
636 were tracked. In the right panel, the frequencies in NAb non-inducers are shown in background
637 (gray) for comparison.
638 **(C)** Comparison of Env gp140-specific PB frequencies between NAb non-inducers and
639 inducers by Mann Whitney U tests. In the right, the frequencies at NAb induction were
640 compared with those at year 1 in NAb non-inducers with ≥ 1-year survival (n = 10). Bars: mean
641 ± SD.
642 **(D)** Left: vector chart of Env gp140-specific memory B cell (B_{mem}) and PB levels. Legends for
643 each animal correspond to the ones in (B). Right: NAb non-inducer vectors empirically define
644 a polygonal GC output attractor area D_n (gray area surrounded with dotted lines) on which
645 they converge by and beyond year 1 p.i. The NAb inducer vectors (shown up to the time of
646 NAb induction) remained outside of D_n. At the moment of NAb induction they converged on a
647 second GC output attractor area D_i (red area surrounded with dotted lines), mutually exclusive
648 with D_n (P < 0.0001 by Fisher's exact test on NAb inducer vector convergence frequency within
649 D_n). Legends for year 1 p.i. in the NAb non-inducers and moment of NAb induction in the NAb
650 inducers are specified.

651 **Materials and Methods**

652

653 **Material availability**

654 This study did not generate new unique reagents.

655

656 **Data and code availability**

657 Data were analyzed using existing computational packages. The accession number for the
658 transcriptome data [WT SIV_{mac239}-infected HSC-F cell line (*n* = 3), Nef-G63E SIV_{mac239}-infected
659 HSC-F cell line (*n* = 3) and uninfected HSC-F cell line (*n* = 3)] has been deposited under the
660 accession number GenBank: GSE65806.

661

662 **Rhesus macaques retrospectively utilized for samples**

663 Seventy Burmese rhesus macaques (*macaca mulatta*) (57 males and 13 females) were
664 retrospectively analyzed in this study. Experiments were previously carried out (Matano et al.,
665 2004; Yamamoto et al., 2007; Iseda et al., 2016; Nomura et al., 2012; Ishii et al., 2012;
666 Takahashi et al., 2013; Nakane et al., 2013; Shi et al., 2013; Iwamoto et al., 2014; Terahara et
667 al., 2014) in the Tsukuba Primate Research Center, National Institutes of Biomedical
668 Innovation, Health and Nutrition (NIBIOHN) with the help of the Corporation for Production
669 and Research of Laboratory Primates and the Institute for Frontier Life and Medical Sciences,
670 Kyoto University (IFLMS-KU) after approval by the Committee on the Ethics of Animal
671 Experiments of NIBIOHN and IFLMS-KU under the guidelines for animal experiments at
672 NIBIOHN, IFLMS-KU and National Institute of Infectious Diseases in accordance with the
673 Guidelines for Proper Conduct of Animal Experiments established by Science Council of
674 Japan (http://www.scj.go.jp/ja/info/kohyo/pdf/kohyo-20-k16-2e.pdf). The experiments were in
675 accordance with the "Weatherall report for the use of non-human primates in research"
676 recommendations (https://royalsociety.org/topics-policy/publications/2006/weatherall-report/).
677 Animals were housed in adjoining individual primate cages allowing them to make sight and
678 sound contact with one another for social interactions, where the temperature was kept at

679 25°C with light for 12 hours per day. Animals were fed with apples and commercial monkey
680 diet (Type CMK-2, Clea Japan, Inc.). Blood collection and virus challenge were performed
681 under ketamine anesthesia.
682
683 **Cells and viruses**
684 MT4-R5 cells were maintained in RPMI1640 (Invitrogen) supplemented with 10% fetal bovine
685 serum (FBS) (Clontech) and antibiotics. HSC-F cells (cynomolgus $CD4^+$ T-cell line) and
686 HSR5.4 cells (rhesus macaque $CD4^+$ T-cell line) were maintained in RPMI1640 (Invitrogen)
687 supplemented with 10% fetal bovine serum (FBS) (Clontech), human interleukin-2 (IL-2) (10
688 IU/ml, Roche), 4-(2-hydroxyethyl)-1-piperazineethanesulfonic acid (HEPES) (Invitrogen) and
689 2-mercaptoethanol (Gibco). SIV_{mac239} molecular clone derivative was generated by
690 mutagenesis PCR (Agilent Technologies) using the primers listed. For virus preparation, COS-
691 1 cells were transfected with pBR_{mac239} proviral DNA using FuGENE 6 (Promega). At 48 h post-
692 transfection, culture supernatants were harvested, centrifuged and filtered through a 0.45-μm
693 pore-size filter (Merck Millipore). To titrate infectivity, prepared viruses were serially diluted and
694 infected on HSC-F cells in 96-well plates (Falcon) in quadruplicate. At 10 days post-infection,
695 the endpoint was determined using SIV p27 antigen enzyme-linked immunosorbent assay
696 (ELISA) kit (ABL), and virus infectivity was calculated as the 50 percent tissue culture infective
697 dose ($TCID_{50}$) according to the Reed-Muench method.
698
699 **Identification of SIV_{mac239}-NAb inducers**
700 Burmese rhesus macaques previously challenged with the highly pathogenic molecular clone
701 virus SIV_{mac239} (n = 70) were retrospectively examined approximately up to 2 years for their
702 plasma NAb profiles. Animals were challenged intravenously with 1,000 $TCID_{50}$ of SIV_{mac239}.
703 In the current study, virological and immunological profiles were compared between the newly
704 identified NAb inducers (n = 9) and representative NAb non-inducers (n = 19). Sex distribution
705 of the NAb inducers (eight males and one female) did not significantly differ with the total non-
706 inducers (49 males and 12 females, P = 0.99 by Fisher's exact test). These NAb non-inducers

707 and eight NAb inducers except R06-032 were previously partially reported for their plasma
708 viral loads (Yamamoto et al., 2007; Iseda et al., 2016; Nomura et al., 2012; Takahashi et al.,
709 2013; Nakane et al., 2013; Iwamoto et al., 2014) (**Figure 1B**). MHC-I haplotypes and alleles
710 were determined by reference strand-mediated conformation analysis, PCR-SSP (PCR
711 amplification utilizing sequence-specific priming) and cloning as described (Naruse et al.,
712 2010). MHC-I binding prediction was made on April 27, 2013 using the IEDB analysis resource
713 NetMHCpan tool (Hoof et al., 2009). Alleles of interest in the study have been previously
714 identified in macaques (Nomura et al., 2012; Evans et al., 1999; Sette et al., 2012). Macaques
715 R06-032, R03-015, R01-010 and R05-010 received a prime-boost vaccination (Matano et al.,
716 2004) composed of a DNA prime/intranasal Sendai virus vector expressing SIV_{mac239} Gag
717 (SeV-Gag). R03-015, R06-019, R06-038 and R10-001 received 300 mg of non-specific rhesus
718 IgG at day 7 post-SIV_{mac239} challenge as an experimental control in our previous reports
719 (Yamamoto et al., 2007; Iseda et al., 2016; Nakane et al., 2013).
720

721 **Plasma viral load quantitation**

722 Plasma viral RNA samples were extracted with High Pure Viral RNA kit (Roche Diagnostics).
723 Serial fivefold sample dilutions were amplified in quadruplicate by reverse transcription and
724 nested PCR using SIV_{mac239} *gag*-specific primers to determine end point via the Reed-Muench
725 method as described previously (Matano et al., 2004; Iseda et al., 2016). The lower limit of
726 detection is approximately 400 viral RNA copies/ml plasma. Viral loads have been previously
727 partially reported (Yamamoto et al., 2007; Nomura et al., 2012; Takahashi et al., 2013; Nakane
728 et al., 2013; Iwamoto et al., 2014).
729

730 **SIV_{mac239}-specific neutralization assay**

731 NAbs were titrated as described (Yamamoto et al., 2007; Iseda et al., 2016). Serial twofold
732 dilutions of heat-inactivated plasma, or polyclonal IgG affinity-purified with Protein G
733 Sepharose 4 Fast Flow (GE Healthcare) from heat-inactivated and filtered plasma were mixed
734 with 10 $TCID_{50}$ of SIV_{mac239} at a 1:1 ratio (5 μl:5 μl) in quadruplicate. After 45-min incubation at

735 room temperature, the 10 µl mixtures were added into 5 x 10^4 MT4-R5 cells/well in 96-well
736 plates. Progeny virus production in day 12 culture supernatants was examined by SIV p27
737 ELISA (ABL) to determine 100% neutralizing endpoint. The lower limit of titration is 1:2.
738 Neutralization in three out of four wells at a dilution of 1:2 is defined as marginally NAb-positive
739 (< 1:2). Results were comparable when the same assay was performed with macaque HSC-
740 F cells (Akari et al., 1996) as targets. NAb inducers R01-012, R02-004, R01-010, R02-007
741 and NAb non-inducer R01-011 were previously partially reported for their NAb titers measured
742 with the same method using MT4 cells as targets (Kawada et al., 2007), which derived
743 comparable results. For assessment of neutralizing activity in IgG, SIV_{mac239}-specific IgGs
744 purified from pools of plasma with SIV_{mac239}-specific NAb titers were obtained from each animal
745 as described (Yamamoto et al., 2007). After complement heat-inactivation at 56°C, 30 min and
746 0.45 µm filtration, IgGs were purified by Protein G Sepharose 4 Fast Flow (GE Healthcare)
747 and concentrated by Amicon Ultra 4, MW 50,000 (Millipore) to 30 mg/ml and similarly
748 examined for their 10 $TCID_{50}$ SIV_{mac239} killing titers on MT4-R5 cells.
749
750 **SIV Env-specific IgG ELISA and immunoblotting**
751 Plasma Env-specific IgG titers were measured as described (Nakane et al., 2013). SIV_{mac251}
752 Env gp120 (ImmunoDiagnostics) were coated on 96-well assay plates (BD) at 1000 ng/ml
753 (100 µl/well). Wells were prewashed with phosphate-buffered saline (PBS), blocked with 0.5%
754 bovine serum albumin (BSA)/PBS overnight and plasma samples were incubated at a 1:20
755 dilution (5 µl:95 µl) for 2 hours. Wells were washed with PBS and SIV Env-bound antibodies
756 were detected with a horseradish peroxidase (HRP)-conjugated goat anti-monkey IgG (H+L)
757 (Bethyl Laboratory) and SureBlue TMB 1-Component Microwell Peroxidase Substrate (KPL).
758 Absorbance at 450 nm was measured. Samples from week 0 pre-challenge and month 3,
759 month 6 and year 1 post-challenge were assessed in duplicate. Week 0 average values were
760 subtracted from corresponding later time point values for calibration. For immunoblotting, SIV
761 virion-specific IgGs in plasma were detected with a SIV_{mac239}-cross-reactive western blotting

762 system (ZeptoMetrix). In the NAb non-inducers, samples from those close to rapid progression
763 (euthanized due to AIDS progression within approximately 1 year) known for low plasma anti-
764 SIV reactivity (Hirsch et al., 2004; Nakane et al., 2013) were not included.
765
766 **Sequencing**
767 Sequencing was performed as described (Matano et al., 2004; Iseda et al., 2016). Viral cDNA
768 fragments spanning from nt (nucleotide) 4829 to nt 7000, nt 6843 to nt 8831 and nt 8677 to nt
769 10196 in SIV_{mac239} (GenBank accession number MM33262) covering SIV *env* and *nef* were
770 amplified from plasma viral RNA by nested RT-PCR using Prime-Script one-step RT-PCR kit
771 v2 (TaKaRa) and KOD-Plus v2 (Toyobo). PCR products were either directly sequenced or
772 subcloned with a TOP10-transforming TOPO blunt-end cloning system (Invitrogen).
773 Sequencing was performed using dye terminator chemistry with an ABI 3730 DNA sequencer
774 (Applied Biosystems). On average, 15 clones were obtained per sample and 20 clones were
775 assessed when *nef* mutations of interest in early time points were subdominant.
776
777 **SIV_{mac239}-specific $CD8^+$ T-cell responses**
778 Virus-specific $CD8^+$ T-cell frequencies were measured as described (Matano et al., 2004;
779 Iseda et al., 2016). Peripheral blood mononuclear cells (PBMCs) were cocultured for 6 hours
780 with autologous herpesvirus papio-immortalized B lymphoblastoid cell lines (B-LCLs) pulsed
781 with Nef peptides (Sigma-Aldrich Japan) at 1 μM concentration or as indicated otherwise
782 under GolgiStop (monensin, BD) presence. Intracellular gamma interferon (IFN-γ) staining
783 was performed using Cytofix/Cytoperm kit (BD) and the following conjugated anti-human
784 monoclonal antibodies (mAbs): anti-CD4-FITC (M-T477, BD Pharmingen), anti-CD8-PerCP
785 (SK1, BD Biosciences), anti-CD3-APC (SP34-2, BD Pharmingen) and anti-IFN-γ-PE (4S.B3,
786 BioLegend). Specific $CD8^+$ T-cell frequencies were determined by subtracting nonspecific IFN-
787 γ^+ $CD8^+$ T-cell frequencies from those after peptide-specific stimulation; frequencies beneath
788 100 cells/million PBMCs were considered negative. Cells acquired by FACS Canto II (BD)

789 were analyzed by FACS Diva (BD) and FlowJo (Treestar). Approximately 1 x 10^5 PBMCs were
790 gated per test.
791
792 **Nef-mediated signaling perturbation analysis**
793 Virus supernatants obtained from COS-1 cells after transfection with WT or mutant SIV_{mac239}
794 molecular clones were used for infection of $CD4^+$ T-cell lines, cynomolgus macaque-derived
795 HSC-F and rhesus macaque-derived HSR5.4 (Akari et al., 1996). QuikChange II XL site-
796 directed mutagenesis kit (Agilent Technologies) was used to construct mutant SIV_{mac239}
797 molecular clones possessing *nef* mutations Nef-G63E (G-to-A mutation at nt 9520) and Nef-
798 G63R (G-to-A mutation at nt 9519) from the WT SIV_{mac239} molecular clone (Kestler et al., 1991)
799 (nt number from GenBank accession number M33262). Cells (1 x 10^5 cells/well in U-bottomed
800 96-well culture plates [BD]) were infected with WT or mutant SIV_{mac239} cultured in RPMI-1640
801 medium supplemented with 10% fetal bovine serum (FBS) for indicated periods at MOI 0.1
802 (intracellular signaling analysis) or 0.001 (supernatant analysis). Culture supernatants were
803 subjected to measurement of SIV capsid p27 concentrations by ELISA. Harvested cells were
804 fixed and permeabilized with Cytofix/Cytoperm kit, washed twice and subjected to
805 immunostaining. The following antibodies were used; anti-SIV_{mac251} Gag p27 mAb (ABL)
806 manually conjugated with Alexa 647 (Life Technologies), anti-SIV_{mac251} Nef mAb (clone 17,
807 epitope peptide corresponding to SIV_{mac239} Nef 71-80 not including the residue G63: Thermo
808 Fisher Scientific/Pierce) manually conjugated with Alexa 488 or Alexa 647, anti-human CD3-
809 APC-Cy7 (SP34-2, BD Pharmingen), anti-human CD4-PerCP (L200, BD Pharmingen), anti-
810 human HLA-ABC-FITC (G46-2.6, BD Pharmingen), anti-human CXCR4-APC (12G5,
811 BioLegend), BST2-Alexa 647 (RS38E, BioLegend), Alexa 488-conjugated anti-phospho-Akt
812 (Ser473) (D9E, CST) and Alexa 488-conjugated anti-phospho-Akt (Thr308) (C31E5E, CST).
813 Cells acquired by FACS Canto II were analyzed by FACS Diva and FlowJo. Approximately 5
814 x 10^4 cells were gated for each test.
815
816 **Ferritin ELISA**

817 Plasma ferritin levels in NAb inducers and control animals were analyzed by monkey ferritin
818 sandwich ELISA kit (LS Bio) according to the manufacturer's instructions.
819
820 **PI3K stimulation assay**
821 5 x 10^4 HSC-F cells were infected with WT or Nef-G63E mutant SIV_{mac239} at MOI 0.2 and
822 cultured for 1 day in medium supplemented with 10% (normal), 1% (1/10 starvation) or 0.1%
823 (1/100 starvation) FBS. For ligand stimulation (**Figure 4-figure supplement 1C**), cells at the
824 end of 1-day culture were pulsed for 20 minutes with 40 ng/ml of recombinant human IFN-γ
825 (Gibco/Thermo Fisher Scientific), 100 IU/ml of recombinant human IL-2 (Roche Diagnostics)
826 or 10 μg/ml of SIV_{mac251} Env gp130 (ImmunoDx). Cells were intracellularly stained using
827 Cytofix/Cytoperm kit with anti-SIV_{mac251} Nef mAb or anti-SIV_{mac251} p27 mAb manually
828 conjugated to Alexa 647 and PE-conjugated anti-human phospho-Akt (Ser473) (D9E, CST) or
829 Alexa 488-conjugated anti-human phospho-Akt (Ser473). Cells acquired by FACS Canto II
830 were analyzed by FACS Diva and FlowJo. Approximately 7 x 10^4 HSC-F cells were gated per
831 test.
832
833 **Transcriptome analysis**
834 Total RNAs were extracted using RNeasy Plus Mini kit (Qiagen) from 2 x 10^6 HSC-F cells 1
835 day after infection with WT or Nef-G63E mutant SIV_{mac239} at MOI 5. Negative control RNA
836 samples were extracted from 2 x 10^6 uninfected HSC-F cells after culture with the same
837 condition. Three sets of experiments were performed. Total RNA samples were subjected to a
838 quality control (QC) analysis using an Agilent 2100 Bioanalyzer. The obtained amounts of total
839 RNAs were: 12.37 ± 0.39 (uninfected), 8.80 ± 0.44 (WT) and 9.02 ± 0.17 (Nef-G63E) μg (P =
840 0.66 for WT versus Nef-G63E by unpaired t test). In all samples, two bands of 18S and 28S
841 rRNA were confirmed and the RNA integrity number (RIN) was 10. 500 ng of total RNA
842 samples were processed with GeneChip WT Plus reagent (Affymetrix/Thermo Fisher
843 Scientific) to produce 150 μl of fragmented and labeled cDNA samples. These were incubated

844 with a Human Gene 2.0 ST Array (Affymetrix/Thermo Fisher Scientific) for 16 hours, 60 rpm
845 at 45°C using GeneChip hybridization oven 645 (Affymetrix/Thermo Fisher Scientific). Results
846 were scanned with GeneChip Scanner 3000 7G (Affymetrix/Thermo Fisher Scientific) and
847 processed with Affymetrix Expression Console Software (Affymetrix/Thermo Fisher Scientific)
848 according to the manufacturer's instructions. Expression values were normalized by the RMA
849 method. Genes above mean background expression within the cognate sample and showing
850 significant difference between WT and Nef-G63E SIV ($P < 0.05$ via unpaired t test for $\log_2$-
851 transformed values, 768 candidates) were determined. Akt-related genes exhibiting a change
852 of approximately 10% or more were representatively extracted and manually aligned by the
853 authors.
854
855 **Peripheral CD4$^+$ T-cell surface staining**
856 Cryopreserved/thawed PBMCs were stained for 30 minutes at 4°C with the following reagents
857 or conjugated anti-human mAbs: Live/Dead Aqua (Life Technologies), anti-CD4-PerCP (L200,
858 BD Pharmingen), anti-CD8-APC-Cy7 (RPA-T8, BD Pharmingen), anti-CD3-Alexa 700 (SP34-
859 2, BD Pharmingen), anti-CD95-PE-Cy7 (DX2, eBioscience), anti-CXCR5-PE (87.1,
860 eBioscience), anti-PD-1-Brilliant Violet 421 (EH12.2H7, BioLegend) and anti-CXCR3-Alexa
861 488 (G025H7, BioLegend). Cells acquired by FACS LSRII Fortessa (BD) were analyzed by
862 FACS Diva and FlowJo. Approximately 1.5 x 10^5 PBMCs were gated per test.
863
864 **Proximity ligation assay (PLA)**
865 A flow cytometry-based arrangement of proximity ligation assay (PLA) (Avin et al., 2017) was
866 performed to quantitatively assess Nef binding to candidate interacting molecules. 1 x 10^5
867 HSC-F cells were infected with SIV_{mac239} at MOI 0.05 in U-bottomed plates and permeated
868 with Cytofix/Perm kit (BD Biosciences). After two washes, they were resuspended in 0.5%
869 BSA/PBS for prevention of experimental procedure-related loss and stained with mouse anti-
870 SIV_{mac251} Nef mAb (clone 17, Thermo Fisher Scientific/Pierce) or mouse IgG1 isotype control

871 mAb (P3.6.2.8.1, Abcam) in combination with either of the following rabbit antibodies: anti-
872 GβL (86B8, CST), anti-mTOR (7C10, CST), polyclonal anti-human PI3K p85 (Merck Millipore),
873 anti-PI3 Kinase p110α (C73F8, CST) or rabbit IgG1 isotype control mAb (DA1E, CST).
874 Antibody-stained cells were subsequently probed with Duolink In Situ PLA Probe anti-mouse
875 PLUS and anti-mouse MINUS probes (Sigma/Merck). Next, they were detected for
876 intermolecular binding using Duolink flow PLA detection kit (Green) (Sigma/Merck) with a
877 reaction time of 100 minutes for post-mouse/rabbit probe linking amplification. Finally, these
878 PLA-subjected cells were additionally stained with anti-SIV_{mac251} Gag p27 mAb manually
879 conjugated with Alexa 647 and anti-CD4-PerCP for 30 minutes for 20 minutes at 4°C. Cells
880 acquired by FACS Canto II were analyzed by FACS Diva and FlowJo. Approximately 1 x 10^5
881 cells were gated per test. Binding index (Y axis) was calculated by deriving the deviation from
882 the summation of: {baseline P: (MFI of background reaction with mouse isotype control/rabbit
883 isotype control) + anti-Nef antibody-derived background Q: [(MFI of reaction with mouse anti-
884 Nef/rabbit isotype control) - (MFI of background reaction with mouse isotype control/rabbit
885 isotype control)] + anti-binding partner antibody-derived background R:[(MFI of reaction with
886 mouse isotype control/rabbit anti-binding partner molecule) - (MFI of background reaction with
887 mouse isotype control/rabbit isotype control)]}.
888
889 **Co-immunoprecipitation analysis**
890 1 x 10^5 HSC-F cells were infected with SIV_{mac239} at MOI 0.05 in U-bottomed plates in
891 quadruplicate for each SIV strain for three days and pooled for each for acquiring cell pellets.
892 These pellets were lysed with Capturem IP & Co-IP Kit lysis buffer (Takara) and portions for
893 each were immunoprecipitated by anti-Sin1 mAb (D7G1A, CST) (1:50 dilution, 20 minutes,
894 room temperature). Spin column membrane-bound immunoprecipitates were obtained by
895 centrifugation with Capturem IP & Co-IP Kit (Clontech/Takara). Whole cell lysates and Sin1-
896 immunoprecipitated products were subjected to SDS-polyacrylamide gel electrophoresis
897 separation on a Mini Protean TGX 4-15% gel (BioRad) and transferred to a Immun-Blot PVDF
898 membrane (BioRad). Immunoblotting was performed by mouse anti-SIV_{mac251} Nef mAb (clone

899 17, Thermo Fisher Scientific/Pierce) primary antibody probing (1:1000 dilution, 18 hours, 4°
900 C) and Mouse TrueBlot ULTRA anti-mouse Ig HRP (eB144, Rockland Immunochemicals)
901 secondary antibody incubation (1:1000 dilution, 30 minutes, room temperature). Nef-specific
902 bands in infected controls were visualized by enhanced chemiluminescence using
903 SuperSignal West Pico PLUS (Thermo Fisher Scientific). Bands auto-detectable by Image
904 Lab software (BioRad) were analyzed for signal intensities. Uncropped images are provided
905 as supplementary data.
906
907 **Cell death assay**
908 Infected cell apoptosis was measured by methods previously described (Jauch et al., 2023).
909 1 x 10^5 HSC-F cells were infected with SIV_{mac239} at MOI 0.1 in U-bottomed plates (six
910 wells/control) for each SIV strain for three days. These cells were stained with CD4-FITC (M-
911 T477, BD Pharmingen) for 15 minutes at room temperature, washed once and next stained
912 with APC Annexin V (Biolegend) in Annexin V Binding Buffer (Biolegend) for 20 minutes at
913 room temperature. Stained reactions were then diluted fivefold with Annexin V Binding Buffer
914 and subjected to analysis. Cells acquired by FACS Lyric were analyzed by FACS Suite and
915 FlowJo. Approximately 1 x 10^4 HSC-F cells were gated per test.
916
917 **Quantitative *in vivo* imaging flow cytometry**
918 Cryopreserved/thawed lymph node cells (LNCs) from several persistently SIV-infected
919 macaques used in previous experiments (Nakane et al., 2013; Takahashi et al., 2013; Iwamoto
920 et al., 2014) were seeded in V-bottomed 96-well plates (Nunc) and blocked with 25 μg/ml of
921 anti-human CD4 (clone L200: BD) in 100 μl volume for 15 minutes at 4°C. After three washes,
922 they were stained with 10 μg/ml of recombinant SIV_{mac239} Env gp140-biotin (Immune
923 Technology) for 30 minutes at 4°C. Cells were then stained with anti-CD19-PC5.5 (J3-119,
924 Beckman Coulter), Live/Dead Aqua (Invitrogen) and streptavidin-APC-Cy7 (BioLegend) for 30
925 minutes at 4°C. After two washes, cells were processed with Cytofix/Cytoperm kit (BD) for 20

926 minutes at 4°C, washed twice, and next intracellularly stained with PE-conjugated anti-human
927 phospho-Akt (Ser473) (D9E, CST) and anti-SIV_{mac251} Nef mAb (clone 17, Thermo Fisher
928 Scientific/Pierce) manually conjugated with Alexa 488 or mouse IgG1 isotype control mAb
929 (P3.6.2.8.1, Abcam) for 30 minutes at 4°C. After final two washes, cells were suspended in
930 0.8% PFA/PBS. All centrifugations for washing (1,200 x g, 2 minutes) were performed at 4°C.
931 Cells were subjected to image acquisition with Image Stream X MKII imaging flow cytometer
932 (Amnis/Merck Millipore/Luminex) and analyzed with IDEAS 6.3 software (Amnis/Merck
933 Millipore/Luminex). Approximately 5 x 10^5 LNCs were acquired for analyses (**Figure 5**). A
934 custom-implemented linear discriminant analysis-based machine learning module (Luminex)
935 was utilized for verifying candidate Nef staining signal-related secondary parameters (**Figure**
936 **5** and **Figure 5-figure supplement 1A**) for their efficacy of target population separation.
937

938 **B-cell Nef invasion *in vitro* assay**

939 For Nef invasion assay, 5 x 10^4 HSC-F cells were infected at MOI 1 for 48 hours. These were
940 then additionally cocultured with 7.5 x 10^4 Ramos B cells for 12 hours with or without addition
941 of macaque T cell-stimulating anti-CD3 antibody (FN-18, Abcam) at 1 µg/ml. Cells were
942 double-stained with Alexa 488-conjugated mouse anti-Nef (clone 17: Thermo
943 Scientific/Pierce) and anti-CD19-PC-5.5 (J3-119, Beckman Coulter). For graphical
944 visualization (**Figure 6A**), interacting Nef^+ infected cell-invaded B cell doublet images acquired
945 with ImageStream X MKII (Amnis/Merck Millipore) were analyzed by IDEAS 6.3 (Amnis/Merck
946 Millipore/Luminex) with the defined noise-cancelling gating (via gating Nef pixel signal
947 $contrast^{lo}$-Nef mean pixel per $object^{hi}$ cells). For Nef invasion modulation verification on
948 conventional flow cytometry, the aforementioned culture condition was similarly used. Anti-
949 CD3 antibody (FN-18, Abcam) addition at 1 µg/ml and phorbol 12-myristate 13-acetate (PMA,
950 Sigma) plus ionomycin (Sigma) addition (10 ng/ml and 50 ng/ml, respectively) l were evaluated.
951 Cells were stained with Alexa 647-conjugated mouse anti-Nef (clone 17: Thermo
952 Scientific/Pierce), anti-CD19-PC-5.5 (J3-119, Beckman Coulter), anti-human phospho-Akt

953 (Ser473)-Alexa 488 (D9E, CST) and Live/Dead Near-IR (Invitrogen) for dead cell exclusion.
954 Dead cell frequencies were less than 3%. For viral phenotype evaluation, 1 x 10^5 HSC-F cells
955 (surface $CD40L^+$) were pre-infected at MOI 0.2 with WT or Nef-G63E mutant SIV_{mac239} six
956 hours before coculture. 1.5 x 10^5 $CD20^+$ B cells, positively selected from fresh PBMCs of
957 uninfected rhesus macaques via anti-CD20 microbeads (Miltenyi Biotec), were cocultured with
958 these HSC-F cells at an E:T ratio of 2:3 for 3 days in the presence of 40 ng/ml carrier-free
959 recombinant human IL-4 (R&D Systems). Cells were surface-stained with anti-human CD20-
960 PerCP (2H7, BioLegend) and intracellularly stained using Cytofix/Cytoperm kit with anti-
961 SIV_{mac251} Nef mAb manually conjugated to Alexa 488 and Alexa 647-conjugated anti-human
962 phospho-Akt (Ser473) (D9E, CST). For **Figure 6B** and **Figure 6C**, Cells acquired by FACS
963 Canto II were analyzed by FACS Diva and FlowJo. Approximately 5 x 10^4 $CD20^+$ primary B
964 cells and 3 x 10^4 $CD19^+$ Ramos B cells were analyzed.
965
966 **Peripheral SIV Env-specific B-cell responses**
967 Peripheral SIV Env gp140-specific memory B cells (B_{mem}) and plasmablasts (PBs) were
968 measured by flow cytometry with procedures modified from previous reports and our
969 experience (Silveira et al., 2015; Hau et al., 2022). First, cryopreserved/thawed PBMCs
970 seeded in V-bottomed 96-well plates (Nunc) were blocked with 25 μg/ml of anti-human CD4
971 (clone L200: BD) in 100 μl volume for 15 minutes at 4°C. This concentration attains blockade
972 of promiscuous SIV Env binding to CD4 comparable to levels by magnetic depletion of $CD3^+$
973 T cells (data not shown). After three washes, they were next stained with 10 μg/ml of
974 recombinant SIV_{mac239} Env gp140-biotin (Immune Technology) for 30 minutes at 4°C. They
975 were subsequently stained with the following anti-human antibodies and fluorochromes for 30
976 minutes at 4°C with combinations as follows; PB/B_{mem}: anti-CD3-APC-Cy7 (SP34-2, BD
977 Pharmingen), anti-CD8-APC-Cy7 (RPA-T8, BD Pharmingen), anti-CD14-APC-Cy7 (M5E2,
978 BioLegend), anti-CD16-APC-Cy7 (3G8, BioLegend), streptavidin-Brilliant Violet 421
979 (BioLegend), anti-CD19-PC5.5 (J3-119, Beckman Coulter) and Live/Dead Aqua (Invitrogen);

980 PB: anti-CD10-APC-Cy7 (HI10a, BioLegend), anti-CD11c-PE-Cy7 (3.9, BioLegend), anti-
981 CD123-PE-Cy7 (6H6, BioLegend) and anti-HLA-DR-PE-Texas Red (TU36, Invitrogen); B_{mem}:
982 anti-CD27-PE/Dazzle 594 (M-T271, BioLegend), anti-CD10-PE-Cy7 (HI10a, BioLegend), anti-
983 IgD-FITC (DaKo), anti-CD38-Alexa 647 (AT1, Santa Cruz Biotechnology), anti-IgG-Alexa 700
984 (G18-145, BD Pharmingen) and anti-CD138-PE (DL-101, eBioscience). After two washes,
985 B_{mem} samples were suspended in 0.8% PFA/PBS. For PB staining, surface-stained cells were
986 further processed with Cytofix/Cytoperm kit (BD) for 20 minutes at 4°C, washed twice, and
987 next intracellularly stained with 10 μg/ml of recombinant SIV_{mac239} Env gp140-biotin (Immune
988 Technology) for 30 minutes at 4°C. After three washes, they were next stained with anti-human
989 IgG-PE (G18-145, BD), anti-human/mouse IRF4-eFluor 660 (3E4, eBioscience), anti-human
990 Ki67-Alexa 700 (B56, BD Pharmingen) and streptavidin-Alexa 488 (BioLegend) for 30 minutes
991 at 4°C. After final two washes, cells were suspended in 0.8% PFA/PBS. Cells acquired with
992 FACS LSRII Fortessa were analyzed with FACS Diva and FlowJo. Approximately 1.5 x 10^5
993 PBMCs were acquired for B_{mem} and 4 x 10^5 PBMCs were acquired for PB analyses (**Figure**
994 **6**). All centrifugations for washing (1,200 x g, 2 minutes) were performed at 4°C. Env-specific
995 PB frequencies were 0 cells/million PBMCs for pre-challenge samples in all animals examined,
996 ruling out background confounding for high-sensitivity quantitation of the population.
997
998 **Statistical Analysis**
999 Analyses were performed via Prism 8 (GraphPad Software). $P < 0.05$ were considered
1000 significant in two-tailed unpaired t tests, paired t tests, Mann Whitney U tests, Fisher's exact
1001 tests, Wilcoxon signed-rank tests, one-way ANOVA with Tukey's post-hoc multiple comparison
1002 tests and two-way ANOVA with Sidak's post-hoc multiple comparison tests. For analysis of
1003 Nef-invaded B-cell pAkt levels, median fluorescence intensities (mFIs) were analyzed due to
1004 relatively small numbers of Nef^+ B cells. Analyses involving pAkt Ser473 levels all derived
1005 comparable results between mFI and MFI for WT versus Nef-G63E virus. Machine learning-

1006 based rating of Nef signal parameters was verified with IDEAS 6.3 Machine Learning Module

1007 (Luminex).

1008 **References**

1009

1010 Adnan, S., Reeves, R.K., Gillis, J., Wong, F.E., Yu, Y., Camp, J.V., Li, Q., Connole, M., Li, Y.,
1011 Piatak, M. Jr., et al. (2016). Persistent low-level replication of SIVΔnef drives maturation of
1012 antibody and CD8 T cell responses to induce protective immunity against vaginal SIV infection.
1013 *PLoS Pathog*. 12, e1006104.

1014

1015 Akari, H., Mori, K., Terao, K., Otani, I., Fukasawa, M., Mukai, R., and Yoshikawa, Y. (1996). In
1016 vitro immortalization of Old World monkey T lymphocytes with Herpesvirus saimiri: its
1017 susceptibility to infection with simian immunodeficiency viruses. *Virology* 218, 382–388.

1018

1019 Al Qureshah, F., Sagadiev, S., Thouvenel, C.D., Liu, S., Hua, Z., Hou, B., Acharya, M., James,
1020 R.G., and Rawlings, D.J. (2021). Activated PI3Kδ signals compromise plasma cell survival via
1021 limiting autophagy and increasing ER stress. *J. Exp. Med.* 218, e20211035.

1022

1023 Angulo, I., Vadas, O., Garçon, F., Banham-Hall, E., Plagnol, V., Leahy, T.R., Baxendale, H.,
1024 Coulter, T., Curtis, J., Wu, C., et al. (2013). Phosphoinositide 3-kinase δ gene mutation
1025 predisposes to respiratory infection and airway damage. *Science* 342, 866–871.

1026

1027 Asano, T., Okada, S., Tsumura, M., Yeh, T.W., Mitsui-Sekinaka, K., Tsujita, Y., Ichinose, Y.,
1028 Shimada, A., Hashimoto, K., Wada, T., et al. (2018). Enhanced AKT phosphorylation of
1029 circulating B cells in patients with activated PI3Kδ syndrome. *Front. Immunol.* 9, 568.

1030

1031 Avery, D.T., Kane, A., Nguyen, T., Lau, A., Nguyen, A., Lenthall, H., Payne, K., Shi, W., Brigden,
1032 H., French, E., et al. (2018). Germline-activating mutations in PIK3CD compromise B cell
1033 development and function. *J. Exp. Med.* 215, 2073–2095.

1034

1035 Avin, A., Levy, M., Porat, Z., and Abramson, J. (2017) Quantitative analysis of protein-protein
1036 interactions and post-translational modifications in rare immune populations. *Nat. Commun.*
1037 8, 1524.
1038
1039 Battegay, M., Moskophidis, D., Waldner, H., Bründler, M.A., Fung-Leung, W.P., Mak, T.W.,
1040 Hengartner, H., and Zinkernagel, R.M. (1993). Impairment and delay of neutralizing antiviral
1041 antibody responses by virus-specific cytotoxic T cells. *J. Immunol.* 151, 5408–5415.
1042
1043 Baumjohann, D., Preite, S., Reboldi, A., Ronchi, F., Ansel, K.M., Lanzavecchia, A., and
1044 Sallusto, F. (2013). Persistent antigen and germinal center B cells sustain T follicular helper
1045 cell responses and phenotype. *Immunity* 38, 596–605.
1046
1047 Bradley, T., Peppa, D., Pedroza-Pacheco, I., Li, D., Cain, D.W., Henao, R., Venkat, V., Hora,
1048 B., Chen, Y., Vandergrift, N.A., et al. (2018). RAB11FIP5 Expression and Altered Natural Killer
1049 Cell Function Are Associated with Induction of HIV Broadly Neutralizing Antibody Responses.
1050 *Cell* 175, 387–399.e17.
1051
1052 Burns, D.P., Collignon, C., and Desrosiers, R.C. (1993). Simian immunodeficiency virus
1053 mutants resistant to serum neutralization arise during persistent infection of rhesus monkeys.
1054 *J. Virol.* 67, 4104–4113.
1055
1056 Campbell, E.M., Nunez, R., and Hope, T.J. (2004). Disruption of the actin cytoskeleton can
1057 complement the ability of Nef to enhance human immunodeficiency virus type 1 infectivity. *J.*
1058 *Virol.* 78, 5745–5755.
1059
1060 Coulter, T.I., Chandra, A., Bacon, C.M., Babar, J., Curtis, J., Screaton, N., Goodlad, J.R.,
1061 Farmer, G., Steele, C.L., Leahy, T.R., et al. (2017). Clinical spectrum and features of activated

1062 phosphoinositide 3-kinase δ syndrome: A large patient cohort study. *J. Allergy Clin. Immunol.*
1063 139, 597–606.e4.
1064
1065 Cubas, R.A., Mudd, J.C., Savoye, A.L., Perreau, M., van Grevenynghe, J., Metcalf, T., Connick,
1066 E., Meditz, A., Freeman, G.J., Abesada-Terk, G. Jr., et al. (2013). Inadequate T follicular cell
1067 help impairs B cell immunity during HIV infection. *Nat. Med.* 19, 494–499.
1068
1069 Cumont, M.C., Diop, O., Vaslin, B., Elbim, C., Viollet, L., Monceaux, V., Lay, S., Silvestri, G.,
1070 Le Grand, R., Müller-Trutwin, M., et al. (2008). Early divergence in lymphoid tissue apoptosis
1071 between pathogenic and nonpathogenic simian immunodeficiency virus infections of
1072 nonhuman primates. *J. Virol.* 82, 1175–1184.
1073
1074 Dornan, G.L., Siempelkamp, B.D., Jenkins, M.L., Vadas, O., Lucas, C.L., and Burke, J.E.
1075 (2017). Conformational disruption of PI3Kδ regulation by immunodeficiency mutations in
1076 PIK3CD and PIK3R1. *Proc. Natl. Acad. Sci. USA* 114, 1982–1987.
1077
1078 Douek, D.C., Brenchley, J.M., Betts, M.R., Ambrozak, D.R., Hill, B.J., Okamoto, Y., Casazza,
1079 J.P., Kuruppu, J., Kunstman, K., Wolinsky, S., et al. (2002). HIV preferentially infects HIV-
1080 specific $CD4^+$ T cells. *Nature* 417, 95–98.
1081
1082 Evans, D.T., O'Connor, D.H., Jing, P., Dzuris, J.L., Sidney, J., da Silva, J., Allen, T.M., Horton,
1083 H., Venham, J.E., Rudersdorf, R.A., et al. (1999). Virus-specific cytotoxic T-lymphocyte
1084 responses select for amino-acid variation in simian immunodeficiency virus Env and Nef. *Nat.*
1085 *Med.* 5, 1270–1276.
1086
1087 Fallet, B., Narr, K., Ertuna, Y.I., Remy, M., Sommerstein, R., Cornille, K., Kreutzfeldt, M., Page,
1088 N., Zimmer, G., Geier, F., et al. (2016). Interferon-driven deletion of antiviral B cells at the onset
1089 of chronic infection. *Sci. Immunol.* 1, pii: eaah6817.

1090

1091 François, F., and Klotman, M.E. (2003). Phosphatidylinositol 3-kinase regulates human
1092 immunodeficiency virus type 1 replication following viral entry in primary CD4+ T lymphocytes
1093 and macrophages. *J. Virol.* 77, 2539–2549.

1094

1095 Fruman, D.A., Snapper, S.B., Yballe, C.M., Davidson, L., Yu, J.Y., Alt, F.W., and Cantley, L.C.
1096 (1999). Impaired B cell development and proliferation in absence of phosphoinositide 3-kinase
1097 p85alpha. *Science* 283, 393–397.

1098

1099 Fukazawa, Y., Park, H., Cameron, M.J., Lefebvre, F., Lum, R., Coombes, N., Mahyari, E.,
1100 Hagen, S.I., Bae, J.Y., Reyes, M.D. 3rd., et al. (2012). Lymph node T cell responses predict
1101 the efficacy of live attenuated SIV vaccines. *Nat. Med.* 18, 1673–1681.

1102

1103 Gauduin, M.C., Yu, Y., Barabasz, A., Carville, A., Piatak, M., Lifson, J.D., Desrosiers, R.C.,
1104 and Johnson, R.P. (2006). Induction of a virus-specific effector-memory CD4+ T cell response
1105 by attenuated SIV infection. *J. Exp. Med.* 203, 2661–2672.

1106

1107 Geyer, M., Fackler, O.T., and Peterlin, B.M. (2001). Structure--function relationships in HIV-1
1108 Nef. *EMBO Rep.* 2, 580–585.

1109

1110 Gitlin, A.D., Shulman, Z. and Nussenzweig, M.C. (2014). Clonal selection in the germinal
1111 centre by regulated proliferation and hypermutation. *Nature* 509, 637–640.

1112

1113 Gray, E.S., Madiga, M.C., Hermanus, T., Moore, P.L., Wibmer, C.K., Tumba, N.L., Werner, L.,
1114 Mlisana, K., Sibeko, S., Williamson, C., et al. (2011). The neutralization breadth of HIV-1
1115 develops incrementally over four years and is associated with CD4+ T cell decline and high
1116 viral load during acute infection. *J. Virol.* 85, 4828–4840.

1117

1118 Haigwood, N.L., Watson, A., Sutton, W.F., McClure, J., Lewis, A., Ranchalis, J., Travis, B.,
1119 Voss, G., Letvin, N.L., Hu, S.L., et al. (1996). Passive immune globulin therapy in the
1120 SIV/macaque model: early intervention can alter disease profile. *Immunol. Lett.* 51, 107–114.
1121
1122 Haralick, R.M., Shanmugam, K., and Dinstein, I. (1973) Textural features for image
1123 classification. *IEEE Transactions on Systems, Man, and Cybernetics* SMC-3, 610–621.
1124
1125 Harris, R.S., Bishop, K.N., Sheehy, A.M., Craig, H.M., Petersen-Mahrt, S.K., Watt, I.N.,
1126 Neuberger, M.S., and Malim, M.H. (2003). DNA deamination mediates innate immunity to
1127 retroviral infection. *Cell* 113, 803–809.
1128
1129 Hashimoto, M., Bhuyan, F., Hiyoshi, M., Noyori, O., Nasser, H., Miyazaki, M., Saito, T., Kondoh,
1130 Y., Osada, H., Kimura, S., et al. (2016). Potential role of the formation of tunneling nanotubes
1131 in HIV-1 spread in macrophages. *J. Immunol.* 196, 1832–1841.
1132
1133 Hau, T.T.T., Nishizawa, M., Harada, S., Phan, M.H., Kanno, Y., Nomura, T., Matsuoka, S.,
1134 Kawana-Tachikawa, A., Hall, W.W., Matano, T., et al. (2022). Association of envelope-specific
1135 B-cell differentiation and viral selective pressure signatures in HIV-1 CRF01_AE infection.
1136 *AIDS* 36, 1629–1641.
1137
1138 Havenar-Daughton, C., Carnathan, D.G., Torrents de la Peña, A., Pauthner, M., Briney, B.,
1139 Reiss, S.M., Wood, J.S., Kaushik, K., van Gils, M.J., Rosales, S.L., et al. (2016). Direct Probing
1140 of Germinal Center Responses Reveals Immunological Features and Bottlenecks for
1141 Neutralizing Antibody Responses to HIV Env Trimer. *Cell Rep.* 17, 2195–2209.
1142
1143 Hirsch, V.M., Santra, S., Goldstein, S., Plishka, R., Buckler-White, A., Seth, A., Ourmanov, I.,
1144 Brown, C.R., Engle, R., Montefiori, D., et al. (2004). Immune failure in the absence of profound
1145 CD4+ T-lymphocyte depletion in simian immunodeficiency virus-infected rapid progressor

1146 macaques. *J. Virol.* 78, 275–284.
1147
1148 Hoof, I., Peters, B., Sidney, J., Pedersen, L.E., Sette, A., Lund, O., Buus, S., and Nielsen, M..
1149 (2009). NetMHCpan, a method for MHC class I binding prediction beyond humans.
1150 *Immunogenetics* 61, 1–13.
1151
1152 Hunziker, L., Recher, M., Macpherson, A.J., Ciurea, A., Freigang, S., Hengartner, H., and
1153 Zinkernagel, R.M. (2003). Hypergammaglobulinemia and autoantibody induction mechanisms
1154 in viral infections. *Nat. Immunol.* 4, 343–349.
1155
1156 Iseda, S., Takahashi, N., Poplimont, H., Nomura, T., Seki, S., Nakane, T., Nakamura, M., Shi,
1157 S., Ishii, H., Furukawa, S., et al. (2016). Biphasic CD8+ T-cell defense in simian
1158 immunodeficiency virus control by acute-phase passive neutralizing antibody immunization. *J.*
1159 *Virol.* 90, 6276–6290.
1160
1161 Ishii, H., Kawada, M., Tsukamoto, T., Yamamoto, H., Matsuoka, S., Shiino, T., Takeda, A.,
1162 Inoue, M., Iida, A., Hara, H., et al. (2012). Impact of vaccination on cytotoxic T lymphocyte
1163 immunodominance and cooperation against simian immunodeficiency virus replication in
1164 rhesus macaques. *J. Virol.* 86, 738–745.
1165
1166 Iwamoto, N., Takahashi, N., Seki, S., Nomura, T., Yamamoto, H., Inoue, M., Shu, T., Naruse,
1167 T.K., Kimura, A., and Matano, T. (2014). Control of simian immunodeficiency virus replication
1168 by vaccine-induced Gag- and Vif-specific $CD8^+$ T cells. *J. Virol.* 88, 425–433.
1169
1170 Jauch, A.J., Bignucolo, O., Seki, S., Ghraichy, M., Delmonte, O.M., von Niederhäusern, V.,
1171 Higgins, R., Ghosh, A., Nishizawa, M., Tanaka, M., et al. (2023). Autoimmunity and
1172 immunodeficiency associated with monoallelic LIG4 mutations via haploinsufficiency. *J.*
1173 *Allergy Clin. Immunol.* 152, 500–516.

1174

1175 Jia, B., Serra-Moreno, R., Neidermyer, W., Rahmberg, A., Mackey, J., Fofana, I.B., Johnson,
1176 W.E., Westmoreland, S., and Evans, D.T. (2009). Species-specific activity of SIV Nef and HIV-
1177 1 Vpu in overcoming restriction by tetherin/BST2. *PLoS Pathog.* 5, e1000429.

1178

1179 Joas, S., Parrish, E.H., Gnanadurai, C.W., Lump, E., Stürzel, C.M., Parrish, N.F., Learn, G.H.,
1180 Sauermann, U., Neumann, B., Rensing, K.M., et al. (2018) Species-specific host factors rather
1181 than virus-intrinsic virulence determine primate lentiviral pathogenicity. *Nat. Commun.* 9, 1371.

1182

1183 Joas, S., Sauermann, U., Roshani, B., Klippert, A., Daskalaki, M., Mätz-Rensing, K., Stolte-
1184 Leeb, N., Heigele, A., Tharp, G.K., Gupta, P.M., et al. (2020). Nef-Mediated CD3-TCR
1185 Downmodulation Dampens Acute Inflammation and Promotes SIV Immune Evasion. *Cell Rep.*
1186 30, 2261–2274.e7.

1187

1188 Johnson, R.P., Glickman, R.L., Yang, J.Q., Kaur, A., Dion, J.T., Mulligan, M.J., and Desrosiers,
1189 R.C. (1997). Induction of vigorous cytotoxic T-lymphocyte responses by live attenuated simian
1190 immunodeficiency virus. *J. Virol.* 71, 7711–7718.

1191

1192 Jolly, C., Kashefi, K., Hollinshead, M., and Sattentau, Q.J. (2004). HIV-1 cell to cell transfer
1193 across an Env-induced, actin-dependent synapse. *J. Exp. Med.* 199, 283–293.

1194

1195 Junt, T., Moseman, E.A., Iannacone, M., Massberg, S., Lang, P.A., Boes, M., Fink, K.,
1196 Henrickson, S.E., Shayakhmetov, D.M., Di Paolo, N.C., et al. (2007). Subcapsular sinus
1197 macrophages in lymph nodes clear lymph-borne viruses and present them to antiviral B cells.
1198 *Nature* 450, 110–114.

1199

1200 Kawada, M., Tsukamoto, T., Yamamoto, H., Takeda, A., Igarashi, H., Watkins, D.I., and Matano,
1201 T. (2007). Long-term control of simian immunodeficiency virus replication with central memory

1202 CD4+ T-cell preservation after nonsterile protection by a cytotoxic T-lymphocyte-based
1203 vaccine. *J. Virol.* 81, 5202–5211.
1204
1205 Kennedy, S.G., Wagner, A.J., Conzen, S.D., Jordán, J., Bellacosa, A., Tsichlis, P.N., and Hay,
1206 N. (1997). The PI 3-kinase/Akt signaling pathway delivers an anti-apoptotic signal. *Genes Dev.*
1207 11, 701–713.
1208
1209 Kestler, H.W. 3rd, Ringler, D.J., Mori, K., Panicali, D.L., Sehgal, P.K., Daniel, M.D., and
1210 Desrosiers, R.C. (1991). Importance of the nef gene for maintenance of high virus loads and
1211 for development of AIDS. *Cell* 65, 651–662.
1212
1213 Khan, H., Sumner, R.P., Rasaiyaah, J., Tan, C.P., Rodriguez-Plata, M.T., Van Tulleken, C.,
1214 Fink, D., Zuliani-Alvarez, L., Thorne, L., Stirling, D., et al. (2020). HIV-1 Vpr antagonizes innate
1215 immune activation by targeting karyopherin-mediated NF-κB/IRF3 nuclear transport. *Elife* 9,
1216 e60821.
1217
1218 Kim, D.H., Sarbassov, D.D., Ali, S.M., Latek, R.R., Guntur, K.V., Erdjument-Bromage, H.,
1219 Tempst, P., and Sabatini, D.M. (2003). GbetaL, a positive regulator of the rapamycin-sensitive
1220 pathway required for the nutrient-sensitive interaction between raptor and mTOR. *Mol. Cell* 11,
1221 895–904.
1222
1223 Kirchhoff, F., Greenough, T.C., Brettler, D.B., Sullivan, L.L. and Desrosiers, R.C. (1995).
1224 Absence of intact nef sequences in a long-term, nonprogressing survivor of HIV-1 infection. *N.*
1225 *Engl. J. Med. 332*, 228–232.
1226
1227 Kumar, A., Abbas, W., Colin, L., Khan, K.A., Bouchat, S., Varin, A., Larbi, A., Gatot, J.S.,
1228 Kabeya, K., Vanhulle, C., et al. (2016). Tuning of AKT-pathway by Nef and its blockade by

1229 protease inhibitors results in limited recovery in latently HIV infected T-cell line. *Sci. Rep.* 6,
1230 24090.
1231
1232 Kumar, V., Scandella, E., Danuser, R., Onder, L., Nitschké, M., Fukui, Y., Halin, C., Ludewig,
1233 B., and Stein, J.V. (2010). Global lymphoid tissue remodeling during a viral infection is
1234 orchestrated by a B cell-lymphotoxin-dependent pathway. *Blood* 115, 4725–4733.
1235
1236 Laguette, N., Sobhian, B., Casartelli, N., Ringeard, M., Chable-Bessia, C., Ségéral, E., Yatim,
1237 A., Emiliani, S., Schwartz, O., and Benkirane, M. (2011). SAMHD1 is the dendritic- and
1238 myeloid-cell-specific HIV-1 restriction factor counteracted by Vpx. *Nature* 474, 654–657.
1239
1240 Langer, S., Hammer, C., Hopfensperger, K., Klein, L., Hotter, D., De Jesus, P.D., Herbert, K.M.,
1241 Pache, L., Smith, N., van der Merwe, J.A., et al. (2019) HIV-1 Vpu is a potent transcriptional
1242 suppressor of NF-κB-elicited antiviral immune responses. *Elife* 8, e41930.
1243
1244 Leuchowius, K.J., Weibrecht, I., Landegren, U., Gedda, L., and Söderberg, O. (2009). Flow
1245 cytometric in situ proximity ligation analyses of protein interactions and post-translational
1246 modification of the epidermal growth factor receptor family. *Cytometry A* 75, 833–839.
1247
1248 Levesque, M.C., Moody, M.A., Hwang, K.K., Marshall, D.J., Whitesides, J.F., Amos, J.D.,
1249 Gurley, T.C., Allgood, S., Haynes, B.B., Vandergrift, N.A., et al. (2009). Polyclonal B cell
1250 differentiation and loss of gastrointestinal tract germinal centers in the earliest stages of HIV-
1251 1 infection. *PLoS Med.* 6, e1000107.
1252
1253 Lichterfeld, M., Kavanagh, D.G., Williams, K.L., Moza, B., Mui, S.K., Miura, T., Sivamurthy, R.,
1254 Allgaier, R., Pereyra, F., Trocha, A., et al. (2007). A viral CTL escape mutation leading to
1255 immunoglobulin-like transcript 4-mediated functional inhibition of myelomonocytic cells. *J. Exp.*
1256 *Med.* 204, 2813–2824.

1257

1258 Limon, J.J., So, L., Jellbauer, S., Chiu, H., Corado, J., Sykes, S.M., Raffatellu, M., and Fruman,
1259 D.A. (2014). mTOR kinase inhibitors promote antibody class switching via mTORC2 inhibition.
1260 *Proc. Natl. Acad. Sci. USA* 111, E5076–5085.

1261

1262 Lindqvist, M., van Lunzen, J., Soghoian, D.Z., Kuhl, B.D., Ranasinghe, S., Kranias, G.,
1263 Flanders, M.D., Cutler, S., Yudanin, N., Muller, M.I., et al. (2012). Expansion of HIV-specific T
1264 follicular helper cells in chronic HIV infection. *J. Clin. Invest.* 122, 3271–3280.

1265

1266 Locci, M., Havenar-Daughton, C., Landais, E., Wu, J., Kroenke, M.A., Arlehamn, C.L., Su, L.F.,
1267 Cubas, R., Davis, M.M., Sette, A., et al. (2013). Human circulating PD-1^{+}CXCR3^{-}CXCR5^{+}
1268 memory Tfh cells are highly functional and correlate with broadly neutralizing HIV antibody
1269 responses. *Immunity* 39, 758–769.

1270

1271 Lucas, C.L., Kuehn, H.S., Zhao, F., Niemela, J.E., Deenick, E.K., Palendira, U., Avery, D.T.,
1272 Moens, L., Cannons, J.L., Biancalana, M., et al. (2014). Dominant-activating germline
1273 mutations in the gene encoding the PI(3)K catalytic subunit p110δ result in T cell senescence
1274 and human immunodeficiency. *Nat. Immunol.* 15*,* 88–97.

1275

1276 Luo, W., Hawse, W., Conter, L., Trivedi, N., Weisel, F., Wikenheiser, D., Cattley, R.T., and
1277 Shlomchik, M.J. (2019). The AKT kinase signaling network is rewired by PTEN to control
1278 proximal BCR signaling in germinal center B cells. *Nat. Immunol.* 20, 736–746.

1279

1280 Marzec, M., Liu, X., Kasprzycka, M., Witkiewicz, A., Raghunath, P.N., El-Salem, M., Robertson,
1281 E., Odum, N., and Wasik, M.A. (2008). IL-2- and IL-15-induced activation of the rapamycin-
1282 sensitive mTORC1 pathway in malignant CD4+ T lymphocytes. *Blood* 111, 2181–2189.

1283

1284 Mason, R.D., Welles, H.C., Adams, C., Chakrabarti, B.K., Gorman, J., Zhou, T., Nguyen, R.,
1285 O'Dell, S., Lusvarghi, S., Bewley, C.A., et al. (2016). Targeted Isolation of Antibodies Directed
1286 against Major Sites of SIV Env Vulnerability. *PLoS Pathog.* 12, e1005537.
1287
1288 Matano, T., Kobayashi, M., Igarashi, H., Takeda, A., Nakamura, H., Kano, M., Sugimoto, C.,
1289 Mori, K., Iida, A., Hirata, T., et al. (2004). Cytotoxic T lymphocyte-based control of simian
1290 immunodeficiency virus replication in a preclinical AIDS vaccine trial. *J. Exp. Med.* 199, 1709–
1291 1718.
1292
1293 Mattapallil, J.J., Douek, D.C., Hill, B., Nishimura, Y., Martin, M., and Roederer, M. (2005).
1294 Massive infection and loss of memory CD4+ T cells in multiple tissues during acute SIV
1295 infection. *Nature* 434, 1093–1097.
1296
1297 McDonald, D., Wu, L., Bohks, S.M., KewalRamani, V.N., Unutmaz, D., and Hope, T.J. (2003).
1298 Recruitment of HIV and its receptors to dendritic cell-T cell junctions. *Science* 300, 1295–1297.
1299
1300 Mikell, I., Sather, D.N., Kalams, S.A., Altfeld, M., Alter, G., and Stamatatos, L. (2011).
1301 Characteristics of the earliest cross-neutralizing antibody response to HIV-1. *PLoS Pathog.* 7,
1302 e1001251.
1303
1304 Moir, S., Malaspina, A., Ogwaro, K.M., Donoghue, E.T., Hallahan, C.W., Ehler, L.A., Liu, S.,
1305 Adelsberger, J., Lapointe, R., Hwu, P., et al. (2001). HIV-1 induces phenotypic and functional
1306 perturbations of B cells in chronically infected individuals. *Proc. Natl. Acad. Sci. USA* 98,
1307 10362–10367.
1308
1309 Moody, M.A., Pedroza-Pacheco, I., Vandergrift, N.A., Chui, C., Lloyd, K.E., Parks, R.,
1310 Soderberg, K.A., Ogbe, A.T., Cohen, M.S., Liao, H.X., Gao, F., et al. (2016). Immune

1311 perturbations in HIV-1-infected individuals who make broadly neutralizing antibodies. *Sci.*
1312 *Immunol.* 1, aag0851.
1313
1314 Moore, P.L., Gray, E.S., Wibmer, C.K., Bhiman, J.N., Nonyane, M., Sheward, D.J., Hermanus,
1315 T., Bajimaya, S., Tumba, N.L., Abrahams, M.R., et al. (2012). Evolution of an HIV glycan-
1316 dependent broadly neutralizing antibody epitope through immune escape. *Nat. Med.* 18,
1317 1688–1692.
1318
1319 Moukambi, F., Rabezanahary, H., Rodrigues, V., Racine, G., Robitaille, L., Krust, B., Andreani,
1320 G., Soundaramourty, C., Silvestre, R., Laforge, M., et al. (2015). Early loss of splenic Tfh cells
1321 in SIV-infected rhesus macaques. *PLoS Pathog.* 11, e1005287.
1322
1323 Moukambi, F., Rabezanahary, H., Fortier, Y., Rodrigues, V., Clain, J., Benmadid-Laktout, G.,
1324 Zghidi-Abouzid, O., Soundaramourty, C., Laforge, M., and Estaquier, J. (2019) Mucosal T
1325 follicular helper cells in SIV-infected rhesus macaques: contributing role of IL-27. *Mucosal*
1326 *Immunol.* 12, 1038–1054.
1327
1328 Nakane, T., Nomura, T., Shi, S., Nakamura, M., Naruse, T.K., Kimura, A., Matano, T., and
1329 Yamamoto, H. (2013). Limited impact of passive non-neutralizing antibody immunization in
1330 acute SIV infection on viremia control in rhesus macaques. *PLoS ONE* 8, e73453.
1331
1332 Naruse, T.K., Chen, Z., Yanagida, R., Yamashita, T., Saito, Y., Mori, K., Akari, H., Yasutomi, Y.,
1333 Miyazawa, M., Matano, T., et al. (2010). Diversity of MHC class I genes in Burmese-origin
1334 rhesus macaques. *Immunogenetics* 62, 601–611.
1335
1336 Neil, S.J., Zang, T., and Bieniasz, P.D. (2008). Tetherin inhibits retrovirus release and is
1337 antagonized by HIV-1 Vpu. *Nature* 451, 425–430.
1338

1339 Ng, C.T., Jaworski, J.P., Jayaraman, P., Sutton, W.F., Delio, P., Kuller, L., Anderson, D.,
1340 Landucci, G., Richardson, B.A., Burton, D.R., et al. (2010). Passive neutralizing antibody
1341 controls SHIV viremia and enhances B cell responses in infant macaques. *Nat. Med.* 16, 1117–
1342 1119.
1343
1344 Nguyen, H., Ramana, C.V., Bayes, J., and Stark, G.R. (2001). Roles of phosphatidylinositol 3-
1345 kinase in interferon-gamma-dependent phosphorylation of STAT1 on serine 727 and activation
1346 of gene expression. *J. Biol. Chem.* 276, 33361–33368.
1347
1348 Nishimura, Y., Gautam, R., Chun, T.W., Sadjadpour, R., Foulds, K.E., Shingai, M., Klein, F.,
1349 Gazumyan, A., Golijanin, J., Donaldson, M., et al. (2017). Early antibody therapy can induce
1350 long-lasting immunity to SHIV. *Nature* 543, 559–563.
1351
1352 Nomura, T., Yamamoto, H., Shiino, T., Takahashi, N., Nakane, T., Iwamoto, N., Ishii, H.,
1353 Tsukamoto, T., Kawada, M., Matsuoka, S., et al. (2012). Association of major histocompatibility
1354 complex class I haplotypes with disease progression after simian immunodeficiency virus
1355 challenge in Burmese rhesus macaques. *J. Virol.* 86, 6481–6490.
1356
1357 Nutt, S.L., Hodgkin, P.D., Tarlinton, D.M., and Corcoran, L.M. (2015). The generation of
1358 antibody-secreting plasma cells. *Nat. Rev. Immunol.* 15, 160–171.
1359
1360 Omori, S.A., Cato, M.H., Anzelon-Mills, A., Puri, K.D., Shapiro-Shelef, M., Calame, K., and
1361 Rickert, R.C. (2006). Regulation of class-switch recombination and plasma cell differentiation
1362 by phosphatidylinositol 3-kinase signaling. *Immunity* 25, 545–557.
1363
1364 Perfetto, S.P., Chattopadhyay, P.K., Lamoreaux, L., Nguyen, R., Ambrozak, D., Koup, R.A.,
1365 and Roederer, M. (2006). Amine reactive dyes: an effective tool to discriminate live and dead
1366 cells in polychromatic flow cytometry. *J. Immunol. Methods* 313, 199–208.

1367

1368 Petrovas, C., Yamamoto, T., Gerner, M.Y., Boswell, K.L., Wloka, K., Smith, E.C., Ambrozak,
1369 D.R., Sandler, N.G., Timmer, K.J., Sun, X., et al. (2012). CD4 T follicular helper cell dynamics
1370 during SIV infection. *J. Clin. Invest.* 122, 3281–3294.

1371

1372 Qiao, X., He, B., Chiu, A., Knowles, D.M., Chadburn, A., and Cerutti, A. (2006). Human
1373 immunodeficiency virus 1 Nef suppresses CD40-dependent immunoglobulin class switching
1374 in bystander B cells. *Nat. Immunol.* 7, 302–310.

1375

1376 Querec, T.D., Akondy, R.S., Lee, E.K., Cao, W., Nakaya, H.I., Teuwen, D., Pirani, A., Gernert,
1377 K., Deng, J., Marzolf, B., et al. (2009). Systems biology approach predicts immunogenicity of
1378 the yellow fever vaccine in humans. *Nat. Immunol.* 10, 116–125.

1379

1380 Ray, J.P., Staron, M.M., Shyer, J.A., Ho, P.C., Marshall, H.D., Gray, S.M., Laidlaw, B.J., Araki,
1381 K., Ahmed, R., Kaech, S.M., et al. (2015). The interleukin-2-mTORc1 kinase axis defines the
1382 signaling, differentiation, and metabolism of T helper 1 and follicular B helper T cells. *Immunity*
1383 43, 690–702.

1384

1385 Recher, M., Lang, K.S., Hunziker, L., Freigang, S., Eschli, B., Harris, N.L., Navarini, A., Senn,
1386 B.M., Fink, K., Lötscher, M., et al. (2004). Deliberate removal of T cell help improves virus-
1387 neutralizing antibody production. *Nat. Immunol.* 5, 934–942.

1388

1389 Recher, M., Lang, K.S., Navarini, A., Hunziker, L., Lang, P.A., Fink, K., Freigang, S., Georgiev,
1390 P., Hangartner, L., Zellweger, R., et al. (2007). Extralymphatic virus sanctuaries as a
1391 consequence of potent T-cell activation. *Nat. Med.* 13, 1316–1323.

1392

1393 Reuschl, A.K., Mesner, D., Shivkumar, M., Whelan, M.V.X., Pallett, L.J., Guerra-Assunção,
1394 J.A., Madansein, R., Dullabh, K.J., Sigal, A., Thornhill, J.P., et al. (2022). HIV-1 Vpr drives a

1395 tissue residency-like phenotype during selective infection of resting memory T cells. *Cell Rep.*
1396 39, 110650.
1397
1398 Rickles, R.J., Botfield, M.C., Weng, Z., Taylor, J.A., Green, O.M., Brugge, J.S., and Zoller, M.J.
1399 (1994). Identification of Src, Fyn, Lyn, PI3K and Abl SH3 domain ligands using phage display
1400 libraries. *EMBO J.* 13, 5598–5604.
1401
1402 Samer, S., Chowdhury, A., Wiche Salinas, T.R., Estrada, P.M.D.R., Reuter, M., Tharp, G.,
1403 Bosinger, S., Cervasi, B., Auger, J., Gill, K., et al. (2023). Lymph-Node-based $CD3^+$ $CD20^+$
1404 cells emerge from membrane exchange between T follicular helper cells and B cells and
1405 increase their frequency following simian immunodeficiency virus infection. *J. Virol.* 97,
1406 e0176022.
1407
1408 Sammicheli, S., Kuka, M., Di Lucia, P., de Oya, N.J., De Giovanni, M., Fioravanti, J., Cristofani,
1409 C., Maganuco, C.G., Fallet, B., Ganzer, L., et al. (2016). Inflammatory monocytes hinder
1410 antiviral B cell responses. *Sci. Immunol.* 1, pii: eaah6789.
1411
1412 Sander, S., Chu, V.T., Yasuda, T., Franklin, A., Graf, R., Calado, D.P., Li, S., Imami, K., Selbach,
1413 M., Di Virgilio, M., et al. (2015). PI3 kinase and FOXO1 transcription factor activity differentially
1414 control B cells in the germinal center light and dark zones. *Immunity* 43, 1075–1086.
1415
1416 Sarbassov, D.D., Guertin, D.A., Ali, S.M., and Sabatini, D.M. (2005) Phosphorylation and
1417 regulation of Akt/PKB by the rictor-mTOR complex. *Science* 307, 1098–1101.
1418
1419 Schindler, M., Münch, J., Brenner, M., Stahl-Hennig, C., Skowronski, J., and Kirchhoff, F.
1420 (2004). Comprehensive analysis of nef functions selected in simian immunodeficiency virus-
1421 infected macaques. *J. Virol.* 78, 10588–10597.
1422

1423 Schindler, M., Münch, J., Kutsch, O., Li, H., Santiago, M.L., Bibollet-Ruche, F., Müller-Trutwin,
1424 M.C., Novembre, F.J., Peeters, M., Courgnaud, V., et al. (2006). Nef-mediated suppression of
1425 T cell activation was lost in a lentiviral lineage that gave rise to HIV-1. *Cell* 125, 1055–1067.
1426
1427 Sette, A., Sidney, J., Southwood, S., Moore, C., Berry, J., Dow, C., Bradley, K., Hoof, I., Lewis,
1428 M.G., Hildebrand, W.H., et al. (2012). A shared MHC supertype motif emerges by convergent
1429 evolution in macaques and mice, but is totally absent in human MHC molecules.
1430 *Immunogenetics* 64, 421–434.
1431
1432 Sheehy, A.M., Gaddis, N.C., Choi, J.D., and Malim, M.H. (2002). Isolation of a human gene
1433 that inhibits HIV-1 infection and is suppressed by the viral Vif protein. *Nature* (2002) 418, 646–
1434 650.
1435
1436 Shi, S., Seki, S., Matano, T., and Yamamoto, H. (2013). IL-21-producer $CD4^+$ T cell kinetics
1437 during primary simian immunodeficiency virus infection. *Microbes Infect.* 15, 697–707.
1438
1439 Shulman, Z., Gitlin, A.D., Weinstein, J.S., Lainez, B., Esplugues, E., Flavell, R.A., Craft, J.E.,
1440 and Nussenzweig, M.C. (2014). Dynamic signaling by T follicular helper cells during germinal
1441 center B cell selection. *Science* 345, 1058–1062.
1442
1443 Silveira, E.L., Kasturi, S.P., Kovalenkov, Y., Rasheed, A.U., Yeiser, P., Jinnah, Z.S., Legere,
1444 T.H., Pulendran, B., Villinger, F., and Wrammert, J. (2015). Vaccine-induced plasmablast
1445 responses in rhesus macaques: phenotypic characterization and a source for generating
1446 antigen-specific monoclonal antibodies. *J. Immunol. Methods* 416, 69–83.
1447
1448 Sommerstein, R., Flatz, L., Remy, M.M., Malinge, P., Magistrelli, G., Fischer, N., Sahin, M.,
1449 Bergthaler, A., Igonet, S., Ter Meulen, J., et al. (2015). Arenavirus glycan shield promotes
1450 neutralizing antibody evasion and protracted infection. *PLoS Pathog.* 11, e1005276.

1451

1452 Srinivasan, L., Sasaki, Y., Calado, D.P., Zhang, B., Paik, J.H., DePinho, R.A., Kutok, J.L.,
1453 Kearney, J.F., Otipoby, K.L., and Rajewsky, K. (2009). PI3 kinase signals BCR-dependent
1454 mature B cell survival. *Cell* 139, 573–586.

1455

1456 Stolp, B., Reichman-Fried, M., Abraham, L., Pan, X., Giese, S.I., Hannemann, S., Goulimari,
1457 P., Raz, E., Grosse, R., and Fackler, O.T. (2009). HIV-1 Nef interferes with host cell motility by
1458 deregulation of Cofilin. *Cell Host Microbe* 6, 174–186.

1459

1460 Stolp, B., Imle, A., Coelho, F.M., Hons, M., Gorina, R., Lyck, R., Stein, J.V., and Fackler, O.T.
1461 (2012). HIV-1 Nef interferes with T-lymphocyte circulation through confined environments in
1462 vivo. *Proc. Natl. Acad. Sci. USA* 109, 18541–18546.

1463

1464 Swingler, S., Zhou, J., Swingler, C., Dauphin, A., Greenough, T., Jolicoeur, P., and Stevenson,
1465 M. (2008). Evidence for a pathogenic determinant in HIV-1 Nef involved in B cell dysfunction
1466 in HIV/AIDS. *Cell Host Microbe* 4, 63–76.

1467

1468 Takahashi, N., Nomura, T., Takahara, Y., Yamamoto, H., Shiino, T., Takeda, A., Inoue, M., Iida,
1469 A., Hara,H., Shu, T., et al. (2013). A novel protective MHC-I haplotype not associated with
1470 dominant Gag-specific $CD8^+$ T-cell responses in SIV_{mac239} infection of Burmese rhesus
1471 macaques. *PLoS ONE* 8, e54300.

1472

1473 Terahara, K., Ishii, H., Nomura, T., Takahashi, N., Takeda, A., Shiino, T., Tsunetsugu-Yokota,
1474 Y., and Matano, T. (2014). Vaccine-induced $CD107a^+$ $CD4^+$ T cells are resistant to depletion
1475 following AIDS virus infection. *J. Virol.* 88, 14232–14240.

1476

1477 Tomaras, G.D., Yates, N.L., Liu, P., Qin, L., Fouda, G.G., Chavez, L.L., Decamp, A.C., Parks,
1478 R.J., Ashley, V.C., Lucas, J.T., et al. (2008). Initial B-cell responses to transmitted human

1479 immunodeficiency virus type 1: virion-binding immunoglobulin M (IgM) and IgG antibodies
1480 followed by plasma anti-gp41 antibodies with ineffective control of initial viremia. *J. Virol.* 82,
1481 12449–12463.
1482
1483 Volcic, M., Sparrer, K.M.J., Koepke, L., Hotter, D., Sauter, D., Stürzel, C.M., Scherer, M.,
1484 Stamminger, T., Hofmann, T.G., Arhel, N.J., et al. (2020). Vpu modulates DNA repair to
1485 suppress innate sensing and hyper-integration of HIV-1. *Nat. Microbiol.* 5, 1247–1261.
1486
1487 Wang, J., Sohn, H., Sun, G., Milner, J.D. and Pierce, S.K. (2014). The autoinhibitory C-terminal
1488 SH2 domain of phospholipase C-γ2 stabilizes B cell receptor signalosome assembly. *Sci.*
1489 *Signal.* 7, ra89.
1490
1491 Whitney, J.B., Hill, A.L., Sanisetty, S., Penaloza-MacMaster, P., Liu, J., Shetty, M., Parenteau,
1492 L., Cabral, C., Shields, J., Blackmore, S., et al. (2014). Rapid seeding of the viral reservoir
1493 prior to SIV viraemia in rhesus monkeys. *Nature* 512, 74–77.
1494
1495 Wülfing, C., Sjaastad, M.D., and Davis, M.M. (1998). Visualizing the dynamics of T cell
1496 activation: intracellular adhesion molecule 1 migrates rapidly to the T cell/B cell interface and
1497 acts to sustain calcium levels. *Proc. Natl. Acad. Sci. USA* 95, 6302–6307.
1498
1499 Xu, H., Wang, X., Malam, N., Aye, P.P., Alvarez, X., Lackner, A.A., and Veazey, R.S. (2015).
1500 Persistent simian immunodeficiency virus infection drives differentiation, aberrant
1501 accumulation, and latent infection of germinal center follicular T helper cells. *J. Virol.* 90,1578–
1502 1587.
1503
1504 Xu, W., Santini, P.A., Sullivan, J.S., He, B., Shan, M., Ball, S.C., Dyer, W.B., Ketas, T.J.,
1505 Chadburn, A., Cohen-Gould, L., et al. (2009). HIV-1 evades virus-specific IgG2 and IgA

1506 responses by targeting systemic and intestinal B cells via long-range intercellular conduits.
1507 *Nat. Immunol.* 10, 1008–1017.
1508
1509 Yamada, E., Nakaoka, S., Klein, L., Reith, E., Langer, S., Hopfensperger, K., Iwami, S.,
1510 Schreiber, G., Kirchhoff, F., Koyanagi, Y., et al. (2018) Human-specific adaptations in Vpu
1511 conferring anti-tetherin activity are critical for efficient early HIV-1 replication in vivo. *Cell Host*
1512 *Microbe* 23, 110–120.e7.
1513
1514 Yamamoto, H., Kawada, M., Takeda, A., Igarashi, H. and Matano, T. (2007). Post-infection
1515 immunodeficiency virus control by neutralizing antibodies. *PLoS ONE 2*, e540.
1516
1517 Yan, J., Shun, M.C., Zhang, Y., Hao, C., and Skowronski, J. (2019). HIV-1 Vpr counteracts
1518 HLTF-mediated restriction of HIV-1 infection in T cells. *Proc. Natl. Acad. Sci. USA.* 116, 9568–
1519 9577.
1520
1521 Zhang, F., Wilson, S.J., Landford, W.C., Virgen, B., Gregory, D., Johnson, M.C., Munch, J.,
1522 Kirchhoff, F., Bieniasz, P.D., and Hatziioannou, T. (2009). Nef proteins from simian
1523 immunodeficiency viruses are tetherin antagonists. *Cell Host Microbe 6*, 54–67.
1524
1525 Zotos, D., Coquet, J.M., Zhang, Y., Light, A., D'Costa, K., Kallies, A., Corcoran, L.M., Godfrey,
1526 D.I., Toellner, K.M., Smyth, M.J., et al. (2010). IL-21 regulates germinal center B cell
1527 differentiation and proliferation through a B cell-intrinsic mechanism. *J. Exp. Med.* 207, 365–
1528 378.
1529

1530 **Supplemental Information Legends**

1531

1532 **Fig. 1-Supplement 1. Profile of SIV_{mac239}-NAb non-inducer subgroup cohort.**

1533 Summary of a SIV_{mac239}-NAb non-inducer subgroup cohort (*n* = 19), composed from previously
1534 partially characterized, MHC class I haplotype-balanced naïve animals. Symbols A+, B+, E+,
1535 J+ and D+ represent possession of MHC-I haplotypes *90-120-Ia*, *90-120-Ib*, *90-010-Ie*, *90-*
1536 *088-Ij* and *90-010-Id*, respectively. For the titers, - represents negative; +/- represents
1537 neutralization in three out of four wells in a quadruplicate test. Gray shadings indicate
1538 euthanasia due to AIDS progression. Mamu-A and Mamu-B alleles of interest in this study are
1539 listed. These NAb non-inducers were previously partially reported for their plasma viral loads
1540 and MHC-I alleles (Nomura et al., 2012; Takahashi et al., 2013; Nakane et al., 2013; Iwamoto
1541 et al., 2014). R01-011 was previously partially reported for NAb titers measured with the same
1542 method using MT4 cells as targets (Kawada et al., 2007), which derived comparable results.

1543

1544 **Fig. 1-Supplement 2. IgG class-switched NAbs in the inducers.**

1545 Titration of SIV_{mac239}-neutralizing IgGs in the NAb inducers. SIV_{mac239}-specific IgGs, purified
1546 from pools of plasma with SIV_{mac239}-specific NAb titers, were obtained from each animal as
1547 described (Yamamoto et al., 2007) and examined for their neutralizing activity by 10 $TCID_{50}$
1548 SIV_{mac239} killing on MT4-R5 cells. NAb-negative anti-SIV IgG and control IgG were prepared
1549 from a representative animal (R01-011) with NAb-negative plasma and pooled plasma of
1550 uninfected rhesus macaques, respectively.

1551

1552 **Fig.1-Supplement 3. Anti-SIV binding IgG profiles in NAb inducers and non-inducers.**

1553 **(A)** Temporal changes in SIV_{mac251} Env gp120-specific antibody titers in the NAb non-inducers
1554 without rapid progression [NAb-negative non-rapid progressors, NAb(-) non-RPs] (left, *n* = 11)
1555 and NAb inducers [NAb(+)] (right, *n* = 9). NAb non-inducers showing rapid progression
1556 (euthanized with AIDS onset within approximately 1 year) were not included except for
1557 macaque R10-001 (shown in the left for aligned comparison). Samples for non-RPs R06-001

1558 and R10-002 were unavailable.

1559 **(B)** Unpaired t test of log-transformed anti-SIV Env Ab titers in NAb(-) non-RPs and NAb
1560 inducers. Bars represent geometric mean absorbance within each group.

1561 **(C)** Lysed SIV_{mac} virion linear antigen-binding at year 1 p.i. in NAb(-) non-RPs (left, *n* = 12)
1562 and NAb inducers (right, *n* = 9). Plasma anti-SIV_{mac251} IgGs were detected using a commercial
1563 western blotting system against the parental strain SIV_{mac251} (ZeptoMetrix). White arrowheads
1564 indicate Env gp120-specific bands. Experiments were performed twice with comparable
1565 results.

1566

1567 **Fig. 1-Supplement 4. Env sequence variation pattern is not a major characteristic of**
1568 **NAb induction.**

1569 SIV_{mac239} Env sequence variations before and after NAb induction. For each animal, the upper
1570 time point shows pre-induction and the lower time point (in purple) shows post-induction (first
1571 or second time point with NAb titer > 1:2). Dominant residue changes are shown as follows:
1572 gp120 (gray), variable regions V1-V5 (blue), and gp41 (blue gray). Subdominant mutations
1573 are uncolored. Unlabeled gray and black shadings show subdominant and dominant deletion
1574 of residues. Parental SIV_{mac239} sequence is listed for V1-V5. Residues mutated in multiple
1575 animals within V1-V5 are shown in red.

1576

1577 **Fig. 3-Supplement 1. Selection of Nef-G63E mutant SIV is linked with Nef_{62-70}-specific**
1578 **$CD8^+$ T-cell response positivity.**

1579 **(A)** Nef_{62-70}-specific CD8+ T-cell responses around week 20 post-SIV challenge in seven
1580 viremic NAb non-inducers possessing either of the MHC-I alleles Mamu-B*039:01, Mamu-
1581 B*004:01 or Mamu-A1*032:02.

1582 **(B)** Temporal supernatant SIV p27 concentrations after wild type (WT) or Nef-G63E mutant
1583 SIV infection at multiplicity of infection (MOI) 0.001 on HSC-F cells. Data represent one of two
1584 independent experiments performed in triplicate. Bars: mean ± SEM.

1585 **(C)** Comparison of plasma viral loads in Nef-G63E-selecting NAb non-inducers (*n* = 7) versus

1586 non-inducers at indicated time points post-SIV challenge. Bars represent geometric means.
1587 log10-transformed values are compared by unpaired t tests.
1588
1589 **Fig. 4-Supplement 1. Decreased Akt hyperactivation properties of Nef-G63E mutant SIV.**
1590 **(A)** Plasma ferritin levels (ng/ml) in examined NAb non-inducers versus Nef-G63E mutant SIV-
1591 selecting NAb inducers around year 1 post-infection. Bars represent mean in each group. Log-
1592 transformed values compared by unpaired t test.
1593 **(B)** Relative levels of pAkt Ser473 (left panel) and threonine (Thr) 308 (right panel) in SIV Nef^+
1594 HSR5.4 cells (MOI 0.1, 4 days p.i.).
1595 **(C)** Relative pAkt Ser473 levels in Nef^+ HSC-F cells without stimuli and transiently pulsed with
1596 IFN-γ, IL-2 or SIV_{mac} Env gp130 after infection (MOI 0.2, 1 day).
1597 **(D)** Gene expression significantly differing between WT and Nef-G63E SIV infection (MOI 5,
1598 1 day). Black bars show potentially Akt-related genes. Asterisks show dynamics concordant
1599 with the Nef-G63E phenotype (PI3K-pAkt Ser473 downstream downregulation or inhibition
1600 upregulation).
1601 **(E)** Representative flow cytometric gating (NAb inducer R01-012, wk 30 p.i.) of peripheral
1602 blood $CXCR3^-CXCR5^+PD\text{-}1^+$ memory follicular CD4+ T cells. Cells were gated as $CD3^+CD8^-$
1603 $CD4^+CD95^+CXCR5^+PD\text{-}1^+CXCR3^-$ live singlet PBMCs. Available samples of six NAb inducers
1604 showing peak Nef-G63E mutant selection around week 30 p.i. and thirteen viremic NAb non-
1605 inducers were tracked.
1606 **(F)** Comparison of peripheral $CXCR3^-CXCR5^+PD\text{-}1^+$ memory Tfh cell frequencies between
1607 pre-SIV infection and around week 30 post-infection in examined NAb non-inducers
1608 developing disease before week 60 (left: n = 5) and alive more than 70 weeks (middle: n = 8)
1609 and Nef-G63E-detected NAb inducers alive more than 70 weeks (right: n = 6). Analyzed by
1610 Wilcoxon signed-rank tests.
1611 MFIs relative to those in uninfected controls (%) are shown. **: $P < 0.01$, ***: $P < 0.001$, n.s.:
1612 not significant between WT and Nef-G63E mutant by unpaired t tests (B-C). Data represent
1613 one of two (B, C) independent experiments performed in triplicate (C: unstimulated) or

1614 quadruplicate (B, C: PI3K-pulsed). Bars: mean ± SEM.

1615

1616 **Fig. 4-Supplement 2. Nef-G63R mutant SIV properties.**

1617 **(A)** Comparison of frequencies of macaques selecting for Nef-G63R mutant in plasma
1618 between NAb non-inducers and inducers. Compared by Fisher's exact test.

1619 **(B)** Temporal relationship of Nef G63R frequencies in plasma virus in a NAb non-inducer
1620 macaque R06-034 preferentially selecting for Nef-G63R but not Nef-G63E mutant. Black
1621 boxes (left Y axis) show $\log_2$ NAb titers; red triangles and blue diamonds (right Y axis) show
1622 percentage of G63E and G63R mutations detected by subcloning (15 clones/point on average),
1623 respectively.

1624 **(C)** Left: representative histograms of relative pAkt serine (Ser) 473 levels in $p27^+$
1625 subpopulations after WT, Nef-G63E or Nef-G63R mutant SIV infection at MOI 0.1 on HSC-F
1626 cells. Numbers show pAkt Ser473 mean fluorescence intensities (MFIs) for each. Right:
1627 Deviation of pAkt Ser473 MFIs in $p27^+$ HSC-F cells compared with mean MFI of uninfected
1628 cells. Analyzed by one-way ANOVA with Tukey's post-hoc multiple comparison tests. Data
1629 represent one of two independent experiments performed in quadruplicate with similar results.

1630

1631 **Fig. 5-Supplement 1. Machine learning-verified morphological gating of Nef-invaded B**
1632 **cells *in vivo*.**

1633 **(A)** Representative gating strategy plus schematic of inguinal lymph node Nef^+CD19^+ B cells
1634 of an SIV_{mac239}-infected rhesus macaque analyzed by ImageStreamX MK II imaging flow
1635 cytometry (R10-012, week 160 p.i.). First-step incorporation of Live/Dead staining gates out
1636 $CD19^+$ B cells staining positive for Nef potentially due to pre-experimental membrane
1637 permeation (e.g., image #246896, #248952 and #71859). Second-step dual gating for
1638 intracellular Nef signal pixel Haralick variance mean (H Variance mean, X axis), a textural
1639 feature calculated from a gray level co-occurrence matrix (GLCM) for each image representing
1640 adjacent pixel signal strength heterogeneity and Nef signal intensity threshold (Y axis) gates
1641 out $CD19^+$ B cells showing potentially non-specific, strong intracellular binary clustered

1642 staining pixels for Nef deriving a large variance (X axis), and/or cells stained overtly strong for
1643 Nef and hence becoming void for feasible image verification (high threshold) (Y axis), both
1644 likely originating stochastically from post-experimental rupturing procedures including
1645 membrane permeation (e.g. image #18541). This two-step noise cancellation results in
1646 acquisition of a Live/Dead^{-}-Nef signal Haralick variance mean^{lo}-Nef signal intensity threshold^{lo}-
1647 Nef^{+}CD19^{+} B-cell population (e.g. image #116318, #116250 and #132927) with a pericellular
1648 Nef^{int-lo} staining, biologically concordant with Nef membrane anchoring, resembling Nef^{+} cells
1649 experimentally generated *in vitro* and showed the highest score in IDEAS6.3 machine learning
1650 module scoring for segregation of typical void vs. valid images (upper right). This gating was
1651 implemented for counting and analysis of Env-specific B-cell Nef invasion *in vivo* (**Figure 5**).
1652 **(B)** Detection of contact-dependent Nef invasion from SIV-infected HSC-F CD4^{+} T cells to
1653 cocultured Ramos B cells *in vitro*. One typical image of an intercellular conduit (SSC, purple)
1654 with Nef (green) protrusions from infected HSC-F cells to CD19^{+} (red) Ramos B cells from two
1655 independent experiments are shown.
1656
1657 **Fig. 7-Supplement 1. Full gating strategy of SIV$_{mac239}$ Env gp140-specific B-cell**
1658 **responses.**
1659 Full gating (R02-004, week 32 p.i.) of SIV Env gp140-specific memory B cells (B_{mem}) and
1660 plasmablasts (PBs) shown in **Figure 7**.

Figure 1

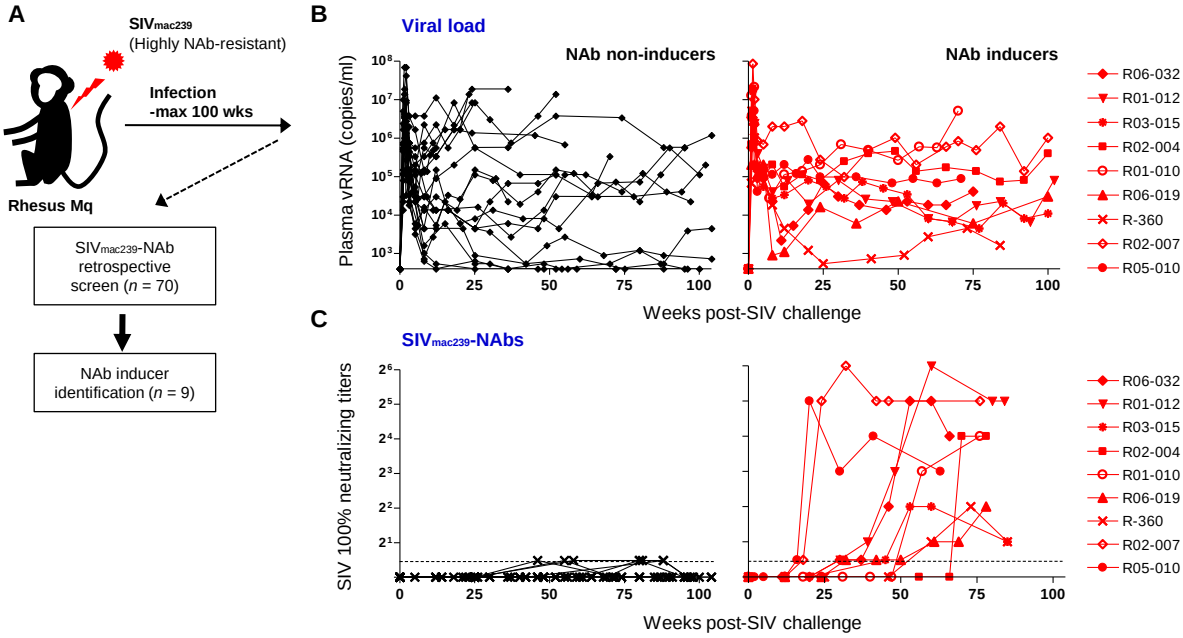
A
SIVmac239
(Highly NAb-resistant)
Infection
-max 100 wks
Rhesus Mq
SIVmac239-NAb
retrospective
screen (n = 70)
NAb inducer
identification (n = 9)
B
Viral load
NAb non-inducers
NAb inducers
Plasma vRNA (copies/ml)
Weeks post-SIV challenge
R06-032
R01-012
R03-015
R02-004
R01-010
R06-019
R-360
R02-007
R05-010
C
SIVmac239-NAbs
SIV 100% neutralizing titers
Weeks post-SIV challenge

Figure 2

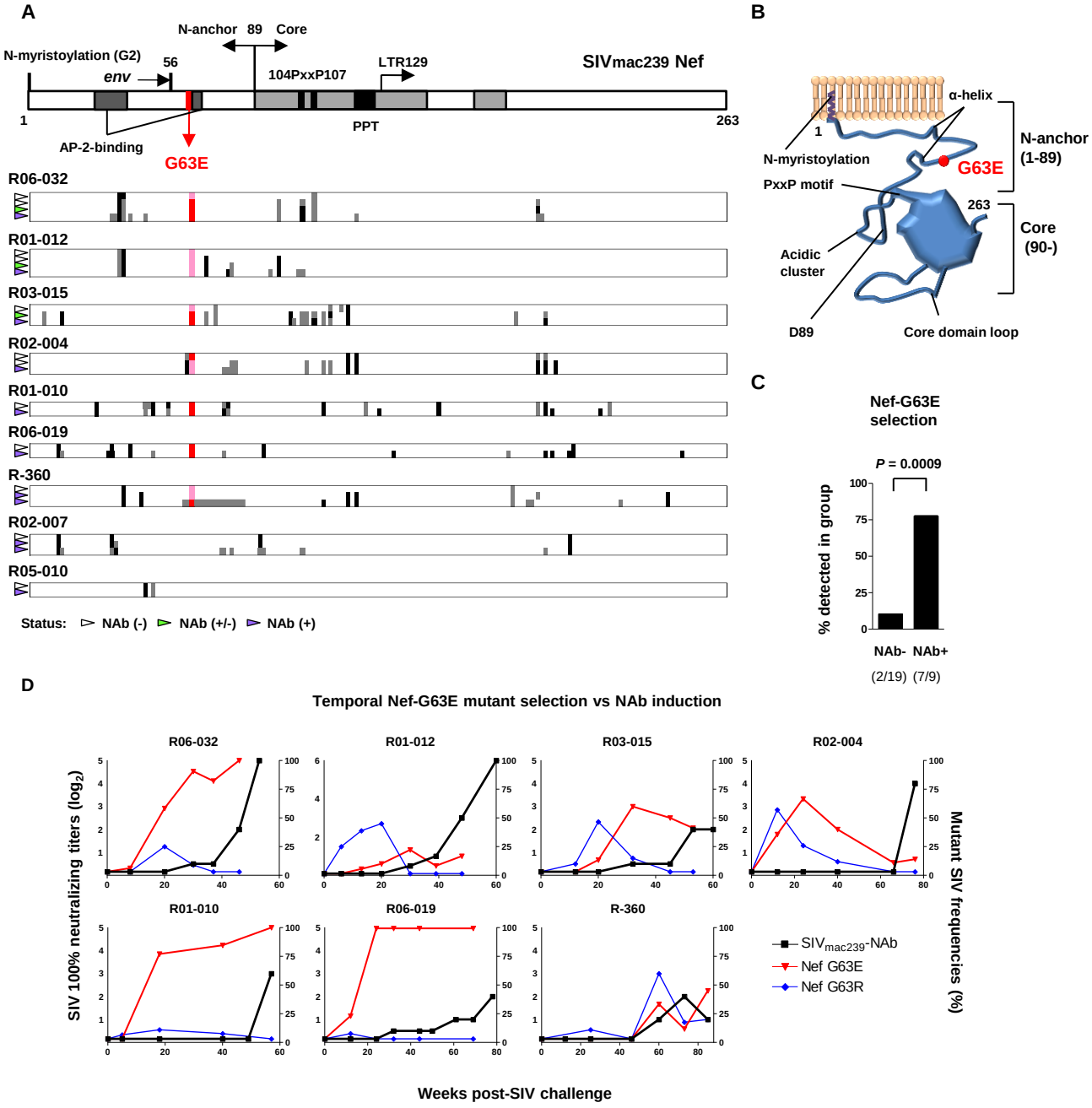
A
N-anchor 89 Core
N-myristoylation (G2)
56
env
104PxxP107
LTR129
SIVmac239 Nef
1
263
PPT
AP-2-binding
G63E
R06-032
R01-012
R03-015
R02-004
R01-010
R06-019
R-360
R02-007
R05-010
Status: NAb (-) NAb (+/-) NAb (+)
B
α-helix
N-anchor (1-89)
1
N-myristoylation
G63E
PxxP motif
263
Core (90-)
Acidic cluster
D89
Core domain loop
C
Nef-G63E selection
P = 0.0009
% detected in group
NAb- NAb+
(2/19) (7/9)
D
Temporal Nef-G63E mutant selection vs NAb induction
R06-032
R01-012
R03-015
R02-004
R01-010
R06-019
R-360
SIV 100% neutralizing titers (log2)
Mutant SIV frequencies (%)
SIVmac239-NAb
Nef G63E
Nef G63R
Weeks post-SIV challenge

Figure 3

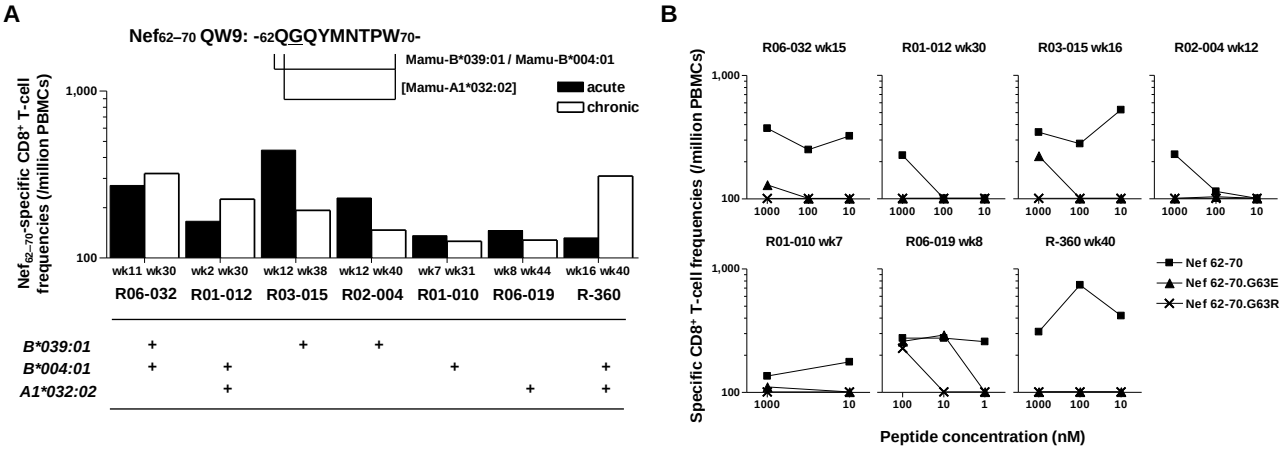
A
Nef62–70 QW9: -62QGQYMNTPW70-
Mamu-B*039:01 / Mamu-B*004:01
[Mamu-A1*032:02]
acute
chronic
Nef62–70-specific CD8+ T-cell frequencies (/million PBMCs)
1,000
100
wk11 wk30
wk2 wk30
wk12 wk38
wk12 wk40
wk7 wk31
wk8 wk44
wk16 wk40
R06-032
R01-012
R03-015
R02-004
R01-010
R06-019
R-360
B*039:01
B*004:01
A1*032:02
B
R06-032 wk15
R01-012 wk30
R03-015 wk16
R02-004 wk12
R01-010 wk7
R06-019 wk8
R-360 wk40
Nef 62-70
Nef 62-70.G63E
Nef 62-70.G63R
Specific CD8+ T-cell frequencies (/million PBMCs)
Peptide concentration (nM)

Figure 4

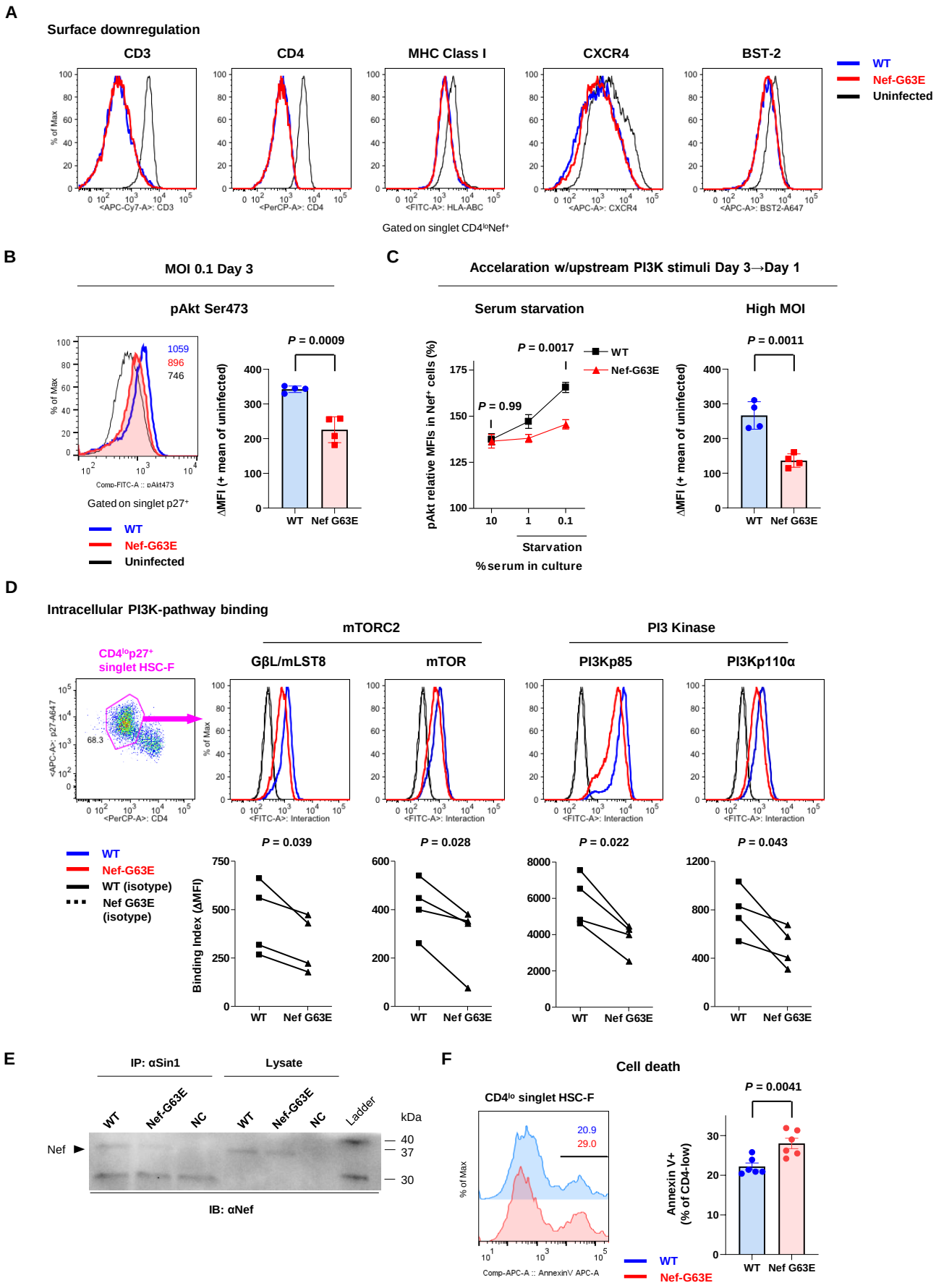
A
Surface downregulation
CD3
CD4
MHC Class I
CXCR4
BST-2
WT
Nef-G63E
Uninfected
% of Max
<APC-Cy7-A>: CD3
<PerCP-A>: CD4
<FITC-A>: HLA-ABC
<APC-A>: CXCR4
<APC-A>: BST2-A647
Gated on singlet CD4loNef+
B
MOI 0.1 Day 3
pAkt Ser473
1059
896
746
Comp-FITC-A :: pAkt473
Gated on singlet p27+
WT
Nef-G63E
Uninfected
P = 0.0009
ΔMFI (+ mean of uninfected)
WT
Nef G63E
C
Accelaration w/upstream PI3K stimuli Day 3→Day 1
Serum starvation
High MOI
P = 0.0017
P = 0.99
pAkt relative MFIs in Nef+ cells (%)
Starvation
% serum in culture
P = 0.0011
D
Intracellular PI3K-pathway binding
mTORC2
PI3 Kinase
CD4lop27+
singlet HSC-F
68.3
<APC-A>: p27-A647
<PerCP-A>: CD4
GβL/mLST8
mTOR
PI3Kp85
PI3Kp110α
<FITC-A>: Interaction
WT (isotype)
Nef G63E (isotype)
P = 0.039
P = 0.028
P = 0.022
P = 0.043
Binding Index (ΔMFI)
E
IP: αSin1
Lysate
Ladder
kDa
Nef
40
37
30
IB: αNef
F
Cell death
CD4lo singlet HSC-F
20.9
29.0
Comp-APC-A :: AnnexinV APC-A
P = 0.0041
Annexin V+ (% of CD4-low)

Figure 5

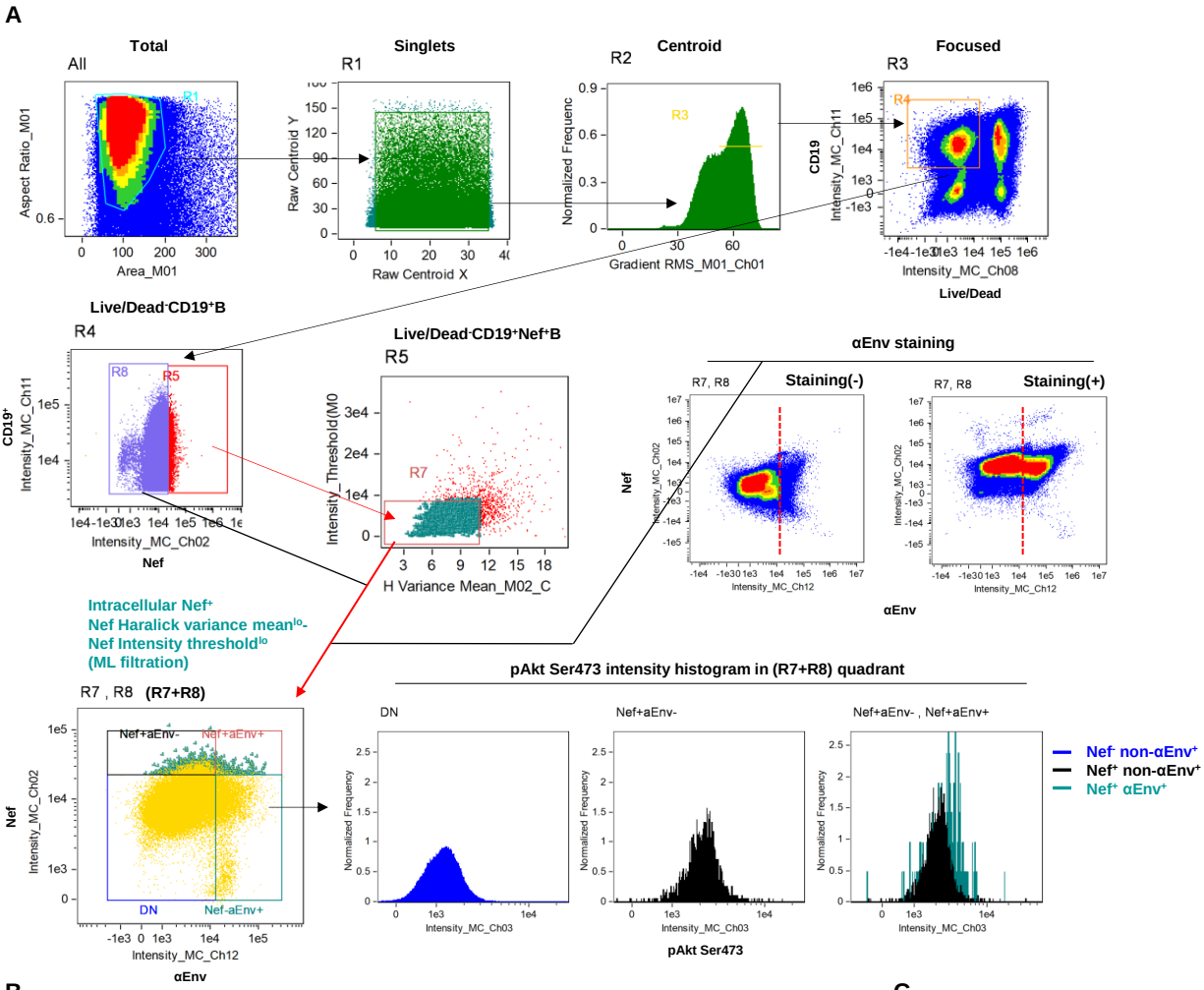
A
Total
All
Aspect Ratio_M01
Area_M01
Singlets
R1
Raw Centroid Y
Raw Centroid X
Centroid
R2
R3
Normalized Frequenc
Gradient RMS_M01_Ch01
Focused
R3
R4
CD19
Intensity_MC_Ch11
Intensity_MC_Ch08
Live/Dead
Live/Dead-CD19+B
R4
R8
R5
CD19+
Intensity_MC_Ch11
Intensity_MC_Ch02
Nef
Live/Dead-CD19+Nef+B
R5
R7
Intensity_Threshold(M0
H Variance Mean_M02_C
αEnv staining
R7, R8
Staining(-)
Staining(+)
Nef
Intensity_MC_Ch02
Intensity_MC_Ch12
αEnv
Intracellular Nef+
Nef Haralick variance mean lo-
Nef Intensity threshold lo
(ML filtration)
pAkt Ser473 intensity histogram in (R7+R8) quadrant
R7 , R8 (R7+R8)
Nef+aEnv-
Nef+aEnv+
DN
Nef-aEnv+
Nef
Intensity_MC_Ch02
Intensity_MC_Ch12
αEnv
DN
Nef+aEnv-
Nef+aEnv- , Nef+aEnv+
Normalized Frequency
Intensity_MC_Ch03
pAkt Ser473
Nef- non-αEnv+
Nef+ non-αEnv+
Nef+ αEnv+

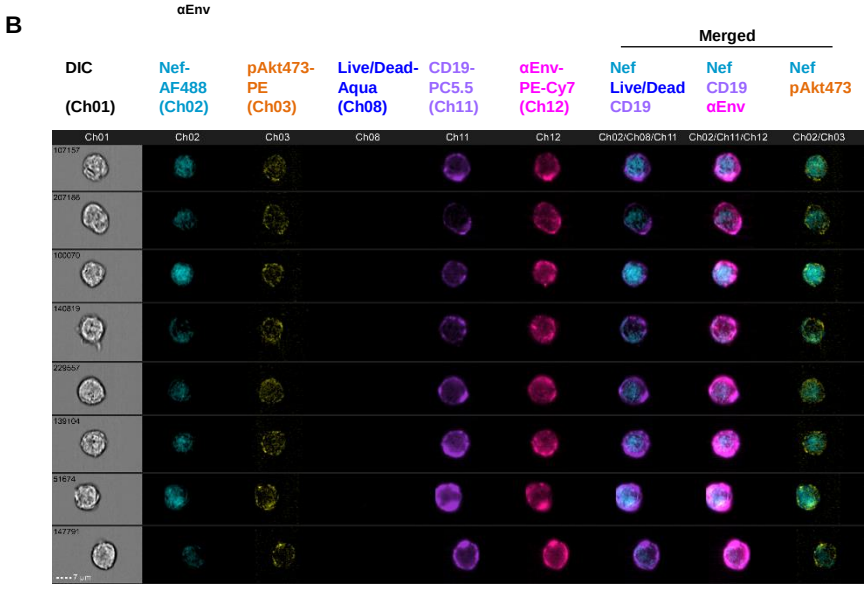
B
Merged
DIC (Ch01)
Nef-AF488 (Ch02)
pAkt473-PE (Ch03)
Live/Dead-Aqua (Ch08)
CD19-PC5.5 (Ch11)
αEnv-PE-Cy7 (Ch12)
Nef Live/Dead CD19
Nef CD19 αEnv
Nef pAkt473
Ch01
Ch02
Ch03
Ch08
Ch11
Ch12
Ch02/Ch08/Ch11
Ch02/Ch11/Ch12
Ch02/Ch03

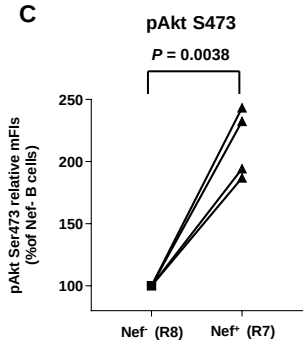
C
pAkt S473
P = 0.0038
pAkt Ser473 relative mFIs (%of Nef- B cells)
Nef- (R8)
Nef+ (R7)

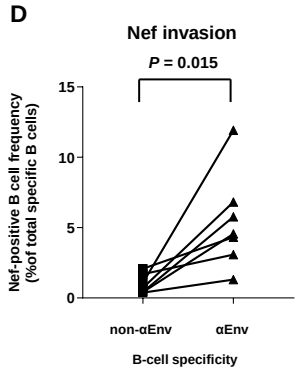
D
Nef invasion
P = 0.015
Nef-positive B cell frequency (%of total specific B cells)
non-αEnv
αEnv
B-cell specificity

Figure 6

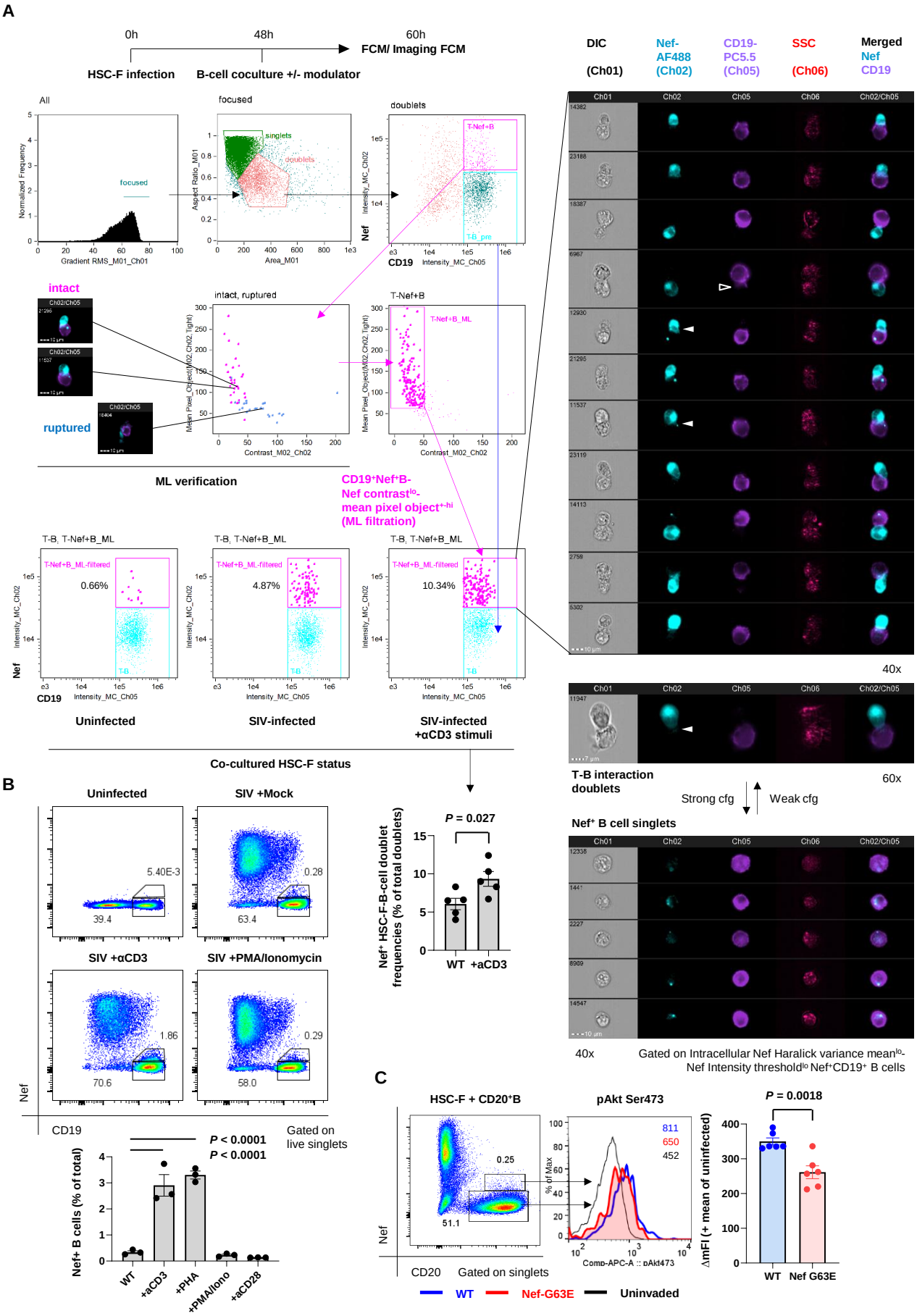
A
0h
48h
60h
FCM/ Imaging FCM
HSC-F infection
B-cell coculture +/- modulator
All
focused
doublets
singlets
Normalized Frequency
Gradient RMS_M01_Ch01
Aspect Ratio_M01
Area_M01
Nef
CD19
Intensity_MC_Ch05
Intensity_MC_Ch02
T-Nef+B
T-B_pre
intact
ruptured
intact, ruptured
T-Nef+B
T-Nef+B_ML
Mean Pixel_Object(M02 Ch02, Tight)
Contrast_M02_Ch02
ML verification
CD19+Nef+B-
Nef contrastlo-
mean pixel object+-hi
(ML filtration)
T-B, T-Nef+B_ML
T-Nef+B_ML-filtered
T-B
0.66%
4.87%
10.34%
Uninfected
SIV-infected
SIV-infected
+αCD3 stimuli
Co-cultured HSC-F status
DIC
(Ch01)
Nef-
AF488
(Ch02)
CD19-
PC5.5
(Ch05)
SSC
(Ch06)
Merged
Nef
CD19
Ch01
Ch02
Ch05
Ch06
Ch02/Ch05
40x
T-B interaction
doublets
60x
Strong cfg
Weak cfg
Nef+ B cell singlets
40x
Gated on Intracellular Nef Haralick variance meanlo-
Nef Intensity thresholdlo Nef+CD19+ B cells
B
Uninfected
SIV +Mock
SIV +αCD3
SIV +PMA/Ionomycin
5.40E-3
39.4
0.28
63.4
1.86
70.6
0.29
58.0
Nef
CD19
Gated on
live singlets
P = 0.027
Nef+ HSC-F-B-cell doublet
frequencies (% of total doublets)
WT
+αCD3
P < 0.0001
P < 0.0001
Nef+ B cells (% of total)
WT
+αCD3
+PHA
+PMA/Iono
+αCD28
C
HSC-F + CD20+B
pAkt Ser473
0.25
51.1
811
650
452
% of Max
Comp-APC-A :: pAkt473
CD20
Gated on singlets
P = 0.0018
ΔmFI (+ mean of uninfected)
WT
Nef G63E
WT
Nef-G63E
Uninvaded

Figure 7

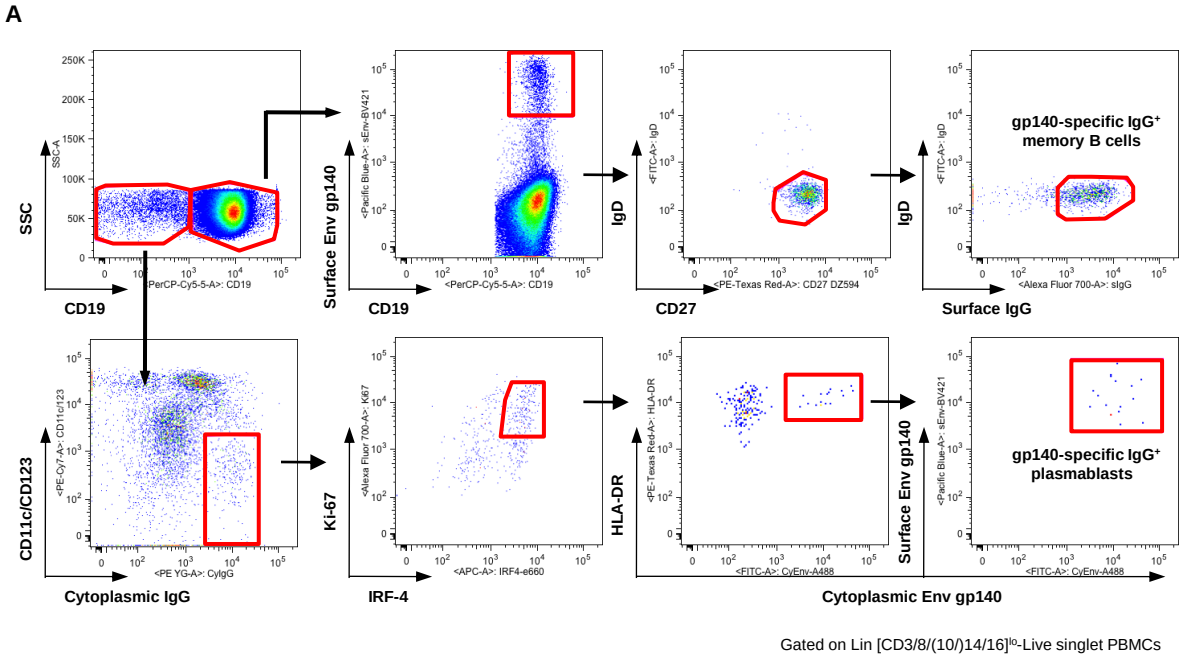
A
SSC
CD19
Surface Env gp140
CD19
IgD
CD27
IgD
Surface IgG
gp140-specific IgG+ memory B cells
CD11c/CD123
Cytoplasmic IgG
Ki-67
IRF-4
HLA-DR
Surface Env gp140
Cytoplasmic Env gp140
gp140-specific IgG+ plasmablasts
Gated on Lin [CD3/8/(10)/14/16]lo-Live singlet PBMCs

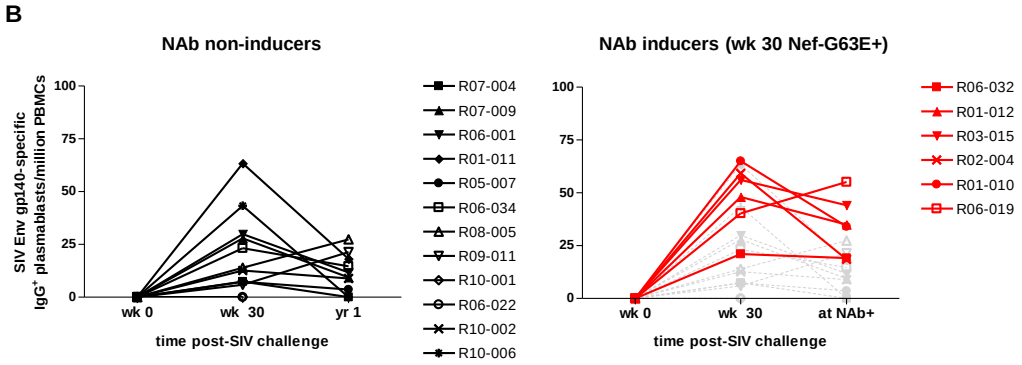
B
NAb non-inducers
NAb inducers (wk 30 Nef-G63E+)
SIV Env gp140-specific IgG+ plasmablasts/million PBMCs
time post-SIV challenge
wk 0
wk 30
yr 1
at NAb+
R07-004
R07-009
R06-001
R01-011
R05-007
R06-034
R08-005
R09-011
R10-001
R06-022
R10-002
R10-006
R06-032
R01-012
R03-015
R02-004
R01-010
R06-019

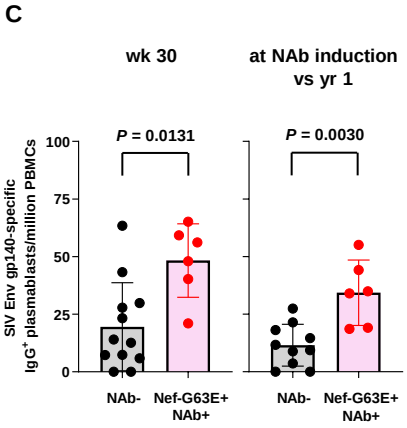
C
wk 30
at NAb induction vs yr 1
P = 0.0131
P = 0.0030
SIV Env gp140-specific IgG+ plasmablasts/million PBMCs
NAb-
Nef-G63E+ NAb+

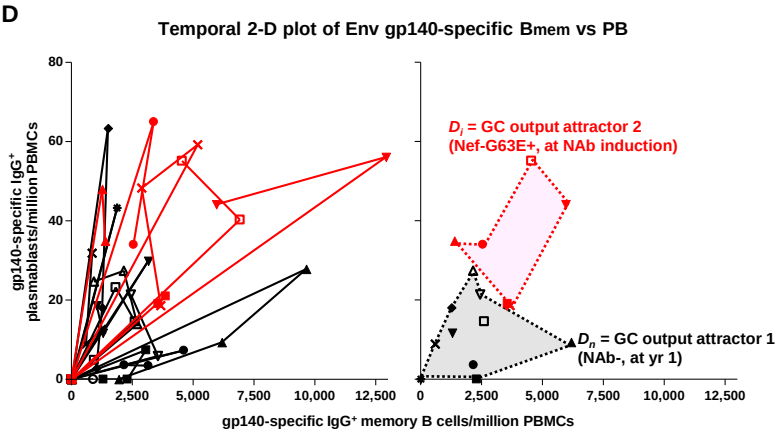
D
Temporal 2-D plot of Env gp140-specific Bmem vs PB
gp140-specific IgG+ plasmablasts/million PBMCs
gp140-specific IgG+ memory B cells/million PBMCs
Di = GC output attractor 2 (Nef-G63E+, at NAb induction)
Dn = GC output attractor 1 (NAb-, at yr 1)

NAb non-inducer cohort (*n* = 19)

MHC-I/ID	SIV$_{mac239}$ neutralization at 1:2 plasma dilution by 10TCID$_{50}$ killing assay (wks p.i.) wk11–20	wk21–30	wk31–40	wk41–50	wk51–60	wk61–70	wk71–80	wk81–90	wk91–104	pVL at 6 mo	Nef G63E at 1 yr	Detected *Mamu* alleles
A+												
R06-037		wk25 -		wk46 +/-			wk72 -	wk87 -	wk95 -	6.4×10^2	- (pVL < 400)	
R07-001		wk25 -		wk42 -				wk88 +/-	wk96 -	< 400	- (pVL < 400)	*A1*032:02*
R07-004		wk25 -		wk46 -		wk64 -	wk74 -	wk86 -		4.5×10^3	+	*B*039:01*
R07-009		wk25 -		wk46 -		wk64 -	wk74 -			4.5×10^3	-	
B+												
R06-001		wk25 -		wk48 -	wk60 -		wk80 -	wk90 -		8.2×10^3	-	
R06-039		wk25 -		wk46 -	wk56 -					8.5×10^6	-	*A1*032:02* , *B*004:01*
E+												
R01-011		wk22 -	wk40 -		wk52 -		wk71 -	wk85 -	wk104 -	1.3×10^5	-	*B*004:01*
R05-007		wk26 -			wk55 +/-		wk71 -	wk89 -	wk97 -	1.6×10^4	-	
R08-007		wk21 -		wk46 -		wk69 -		wk82 +/-		8.5×10^6	-	
R09-011	wk18 -		wk36 -		wk52 -					8.5×10^6	-	
R06-038		wk25 -			wk58 +/-		wk80 +/-		wk95 -	1.1×10^5	-	
J+												
R04-014	wk12 -	wk25 -	wk40 -							1.5×10^5	+ (wk40)	*B*039:01*
R06-022	wk12 -	wk23 -								1.4×10^7	- (wk23)	*B*039:01*
R10-001	wk14 -	wk30 -	wk37 -							1.9×10^7	- (wk37)	*B*039:01*
D+												
R05-006		wk25 -		wk48 -			wk80 -	wk90 -	wk98 -	5.4×10^2	-	*A1*032:02* , *B*004:01*
R06-034		wk25 -		wk42 -		wk61 -	wk80 +/-	wk88 +/-	wk96 -	4.5×10^3	-	*A1*032:02* , *B*004:01*
R08-005		wk25 -		wk48 -		wk68 -			wk100 -	9.0×10^2	-	*A1*032:02* , *B*004:01*
Others												
R10-002	wk14 -				wk59 -				wk104 -	5.7×10^5	-	
R10-006	wk14 -	wk30 -			wk55 -					1.0×10^6	-	

Group	Rhesus ID	mg/ml (IgG)	Collected/pooled (wks post-challenge)	10 $TCID_{50}$ SIV_{mac239} 100% killing titer
NAb (+)	R06-032	30	wk 76	1:16
	R01-012	30	wk 73–87	1:32
	R03-015	30	wk 112	1:8
	R02-004	30	wk 76	1:4
	R01-010	30	wk 77	1:16
	R06-019	30	wk 85	1:4
	R-360	30	wk 60–86	1:4
	R02-007	30	wk 42–70	1:32
	R05-010	30	wk 71	1:64
NAb (-)	R01-011	42	wk 104	< 1:2
uninfected	pooled	36	-	< 1:2

A

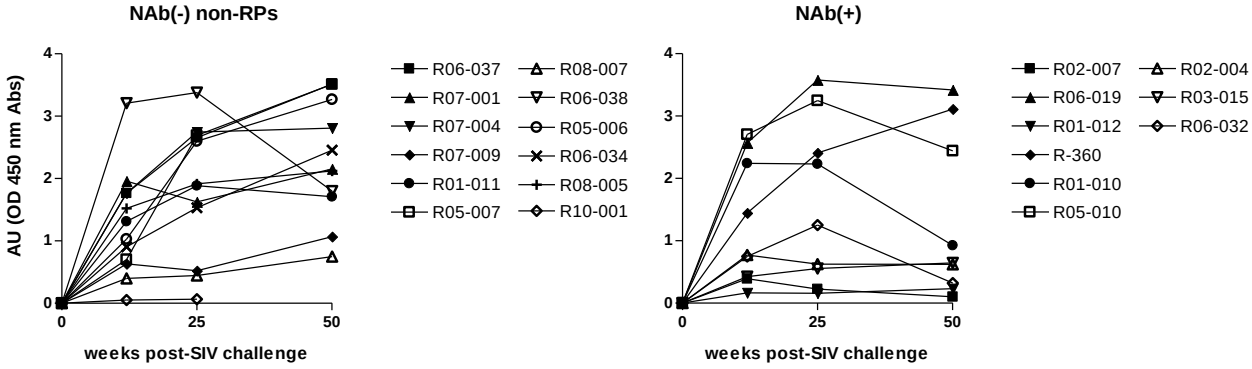
NAb(-) non-RPs
AU (OD 450 nm Abs)
weeks post-SIV challenge
R06-037
R07-001
R07-004
R07-009
R01-011
R05-007
R08-007
R06-038
R05-006
R06-034
R08-005
R10-001
NAb(+)
AU (OD 450 nm Abs)
weeks post-SIV challenge
R02-007
R06-019
R01-012
R-360
R01-010
R05-010
R02-004
R03-015
R06-032

B

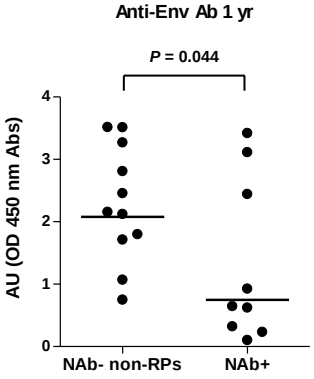
Anti-Env Ab 1 yr
P = 0.044
AU (OD 450 nm Abs)
NAb- non-RPs
NAb+

C

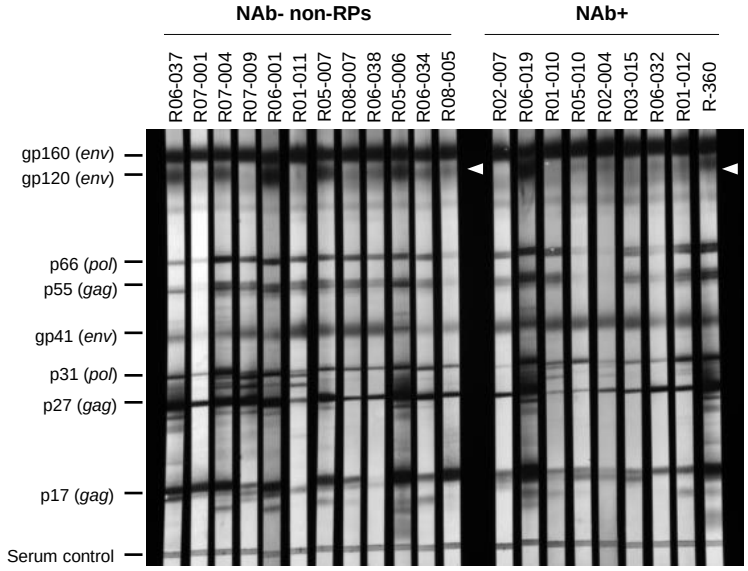
NAb- non-RPs
NAb+
R06-037
R07-001
R07-004
R07-009
R06-001
R01-011
R05-007
R08-007
R06-038
R05-006
R06-034
R08-005
R02-007
R06-019
R01-010
R05-010
R02-004
R03-015
R06-032
R01-012
R-360
gp160 (env)
gp120 (env)
p66 (pol)
p55 (gag)
gp41 (env)
p31 (pol)
p27 (gag)
p17 (gag)
Serum control

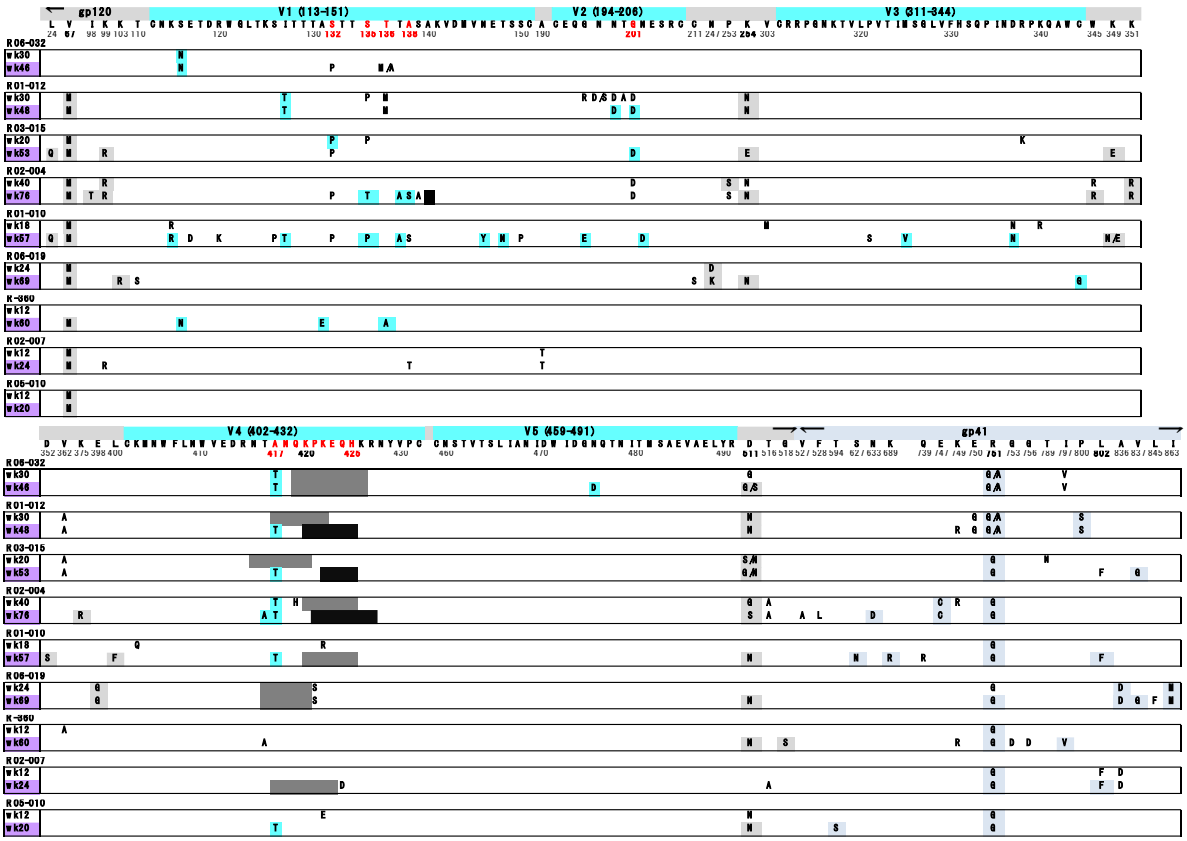
gp120
V1 (113-151)
V2 (194-206)
V3 (311-344)
R06-032
wk30
wk46
R01-012
wk30
wk48
R03-015
wk20
wk53
R02-004
wk40
wk76
R01-010
wk18
wk57
R06-019
wk24
wk69
K-560
wk12
wk60
R02-007
wk12
wk24
R05-010
wk12
wk20
V4 (402-432)
V5 (459-491)
gp41

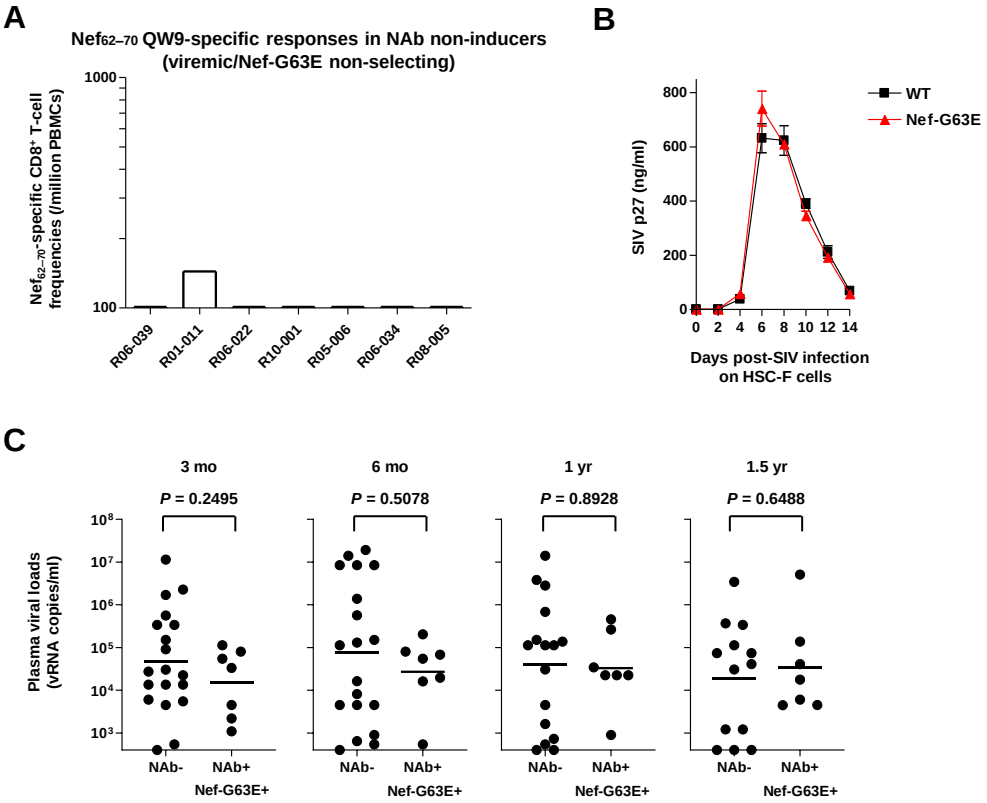
A
Nef62–70 QW9-specific responses in NAb non-inducers
(viremic/Nef-G63E non-selecting)
Nef62–70-specific CD8+ T-cell frequencies (/million PBMCs)
1000
100
R06-039
R01-011
R06-022
R10-001
R05-006
R06-034
R08-005
B
SIV p27 (ng/ml)
800
600
400
200
0
0 2 4 6 8 10 12 14
Days post-SIV infection on HSC-F cells
WT
Nef-G63E
C
3 mo
6 mo
1 yr
1.5 yr
P = 0.2495
P = 0.5078
P = 0.8928
P = 0.6488
Plasma viral loads (vRNA copies/ml)
10^8
10^7
10^6
10^5
10^4
10^3
NAb-
NAb+
Nef-G63E+

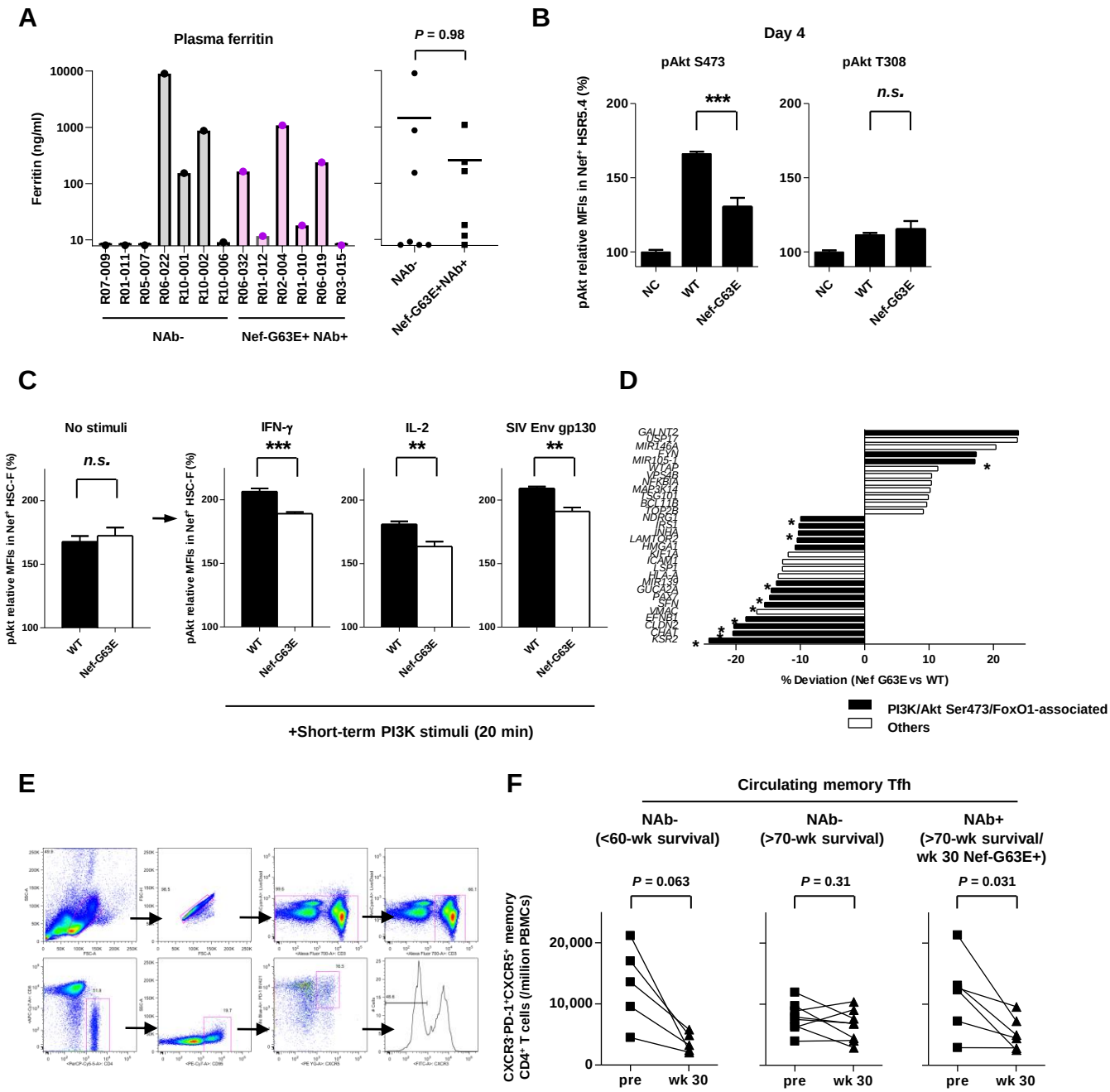
A
Plasma ferritin
Ferritin (ng/ml)
10000
1000
100
10
R07-009
R01-011
R05-007
R06-022
R10-001
R10-002
R10-006
R06-032
R01-012
R02-004
R01-010
R06-019
R03-015
NAb-
Nef-G63E+ NAb+
P = 0.98
NAb-
Nef-G63E+NAb+
B
Day 4
pAkt S473
pAkt T308
pAkt relative MFIs in Nef+ HSR5.4 (%)
***
n.s.
200
150
100
NC
WT
Nef-G63E
C
No stimuli
IFN-γ
IL-2
SIV Env gp130
pAkt relative MFIs in Nef+ HSC-F (%)
n.s.
***
**
**
WT
Nef-G63E
+Short-term PI3K stimuli (20 min)
D
GALNT2
USP17
MIR146A
FYN
MIR105-1
WTAP
VPS4B
NFKBIA
MAP3K14
TSG101
BCL11B
TOP2B
NDRG1
IRS1
INPA
LAMTOR2
HMGA1
KIF1A
ICAM1
LSP1
HLA-A
MIR139
GUCA2A
PAX2
SFN
VMAC
EFNB1
CLDN2
CHAT
KSR2
-20
-10
0
10
20
% Deviation (Nef G63E vs WT)
PI3K/Akt Ser473/FoxO1-associated
Others
E
F
Circulating memory Tfh
NAb-
(<60-wk survival)
NAb-
(>70-wk survival)
NAb+
(>70-wk survival/
wk 30 Nef-G63E+)
P = 0.063
P = 0.31
P = 0.031
CXCR3-PD-1+CXCR5+ memory
CD4+ T cells (/million PBMCs)
20,000
10,000
0
pre
wk 30

A

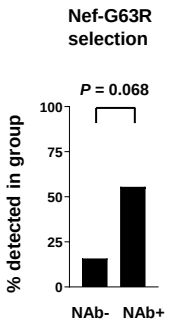
Nef-G63R selection
P = 0.068
% detected in group
100
75
50
25
0
NAb-
NAb+

B

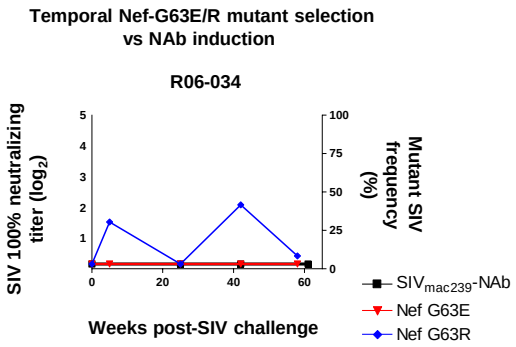
Temporal Nef-G63E/R mutant selection vs NAb induction
R06-034
SIV 100% neutralizing titer (log2)
Mutant SIV frequency (%)
Weeks post-SIV challenge
SIVmac239-NAb
Nef G63E
Nef G63R

C

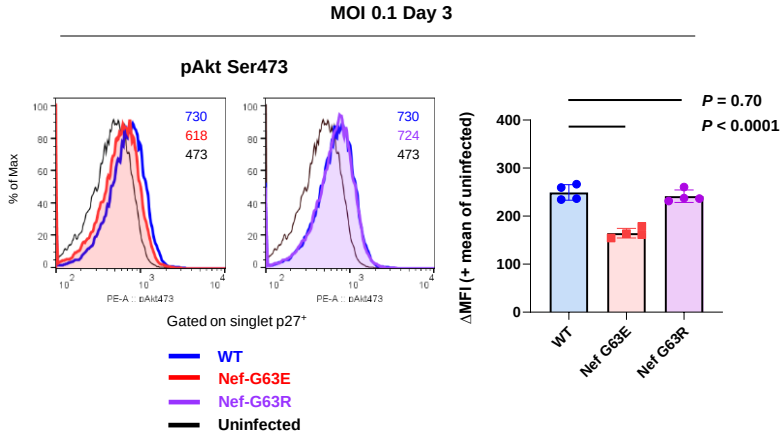
MOI 0.1 Day 3
pAkt Ser473
% of Max
730
618
473
730
724
473
PE-A :: pAkt473
Gated on singlet p27+
WT
Nef-G63E
Nef-G63R
Uninfected
ΔMFI (+ mean of uninfected)
P = 0.70
P < 0.0001
WT
Nef G63E
Nef G63R

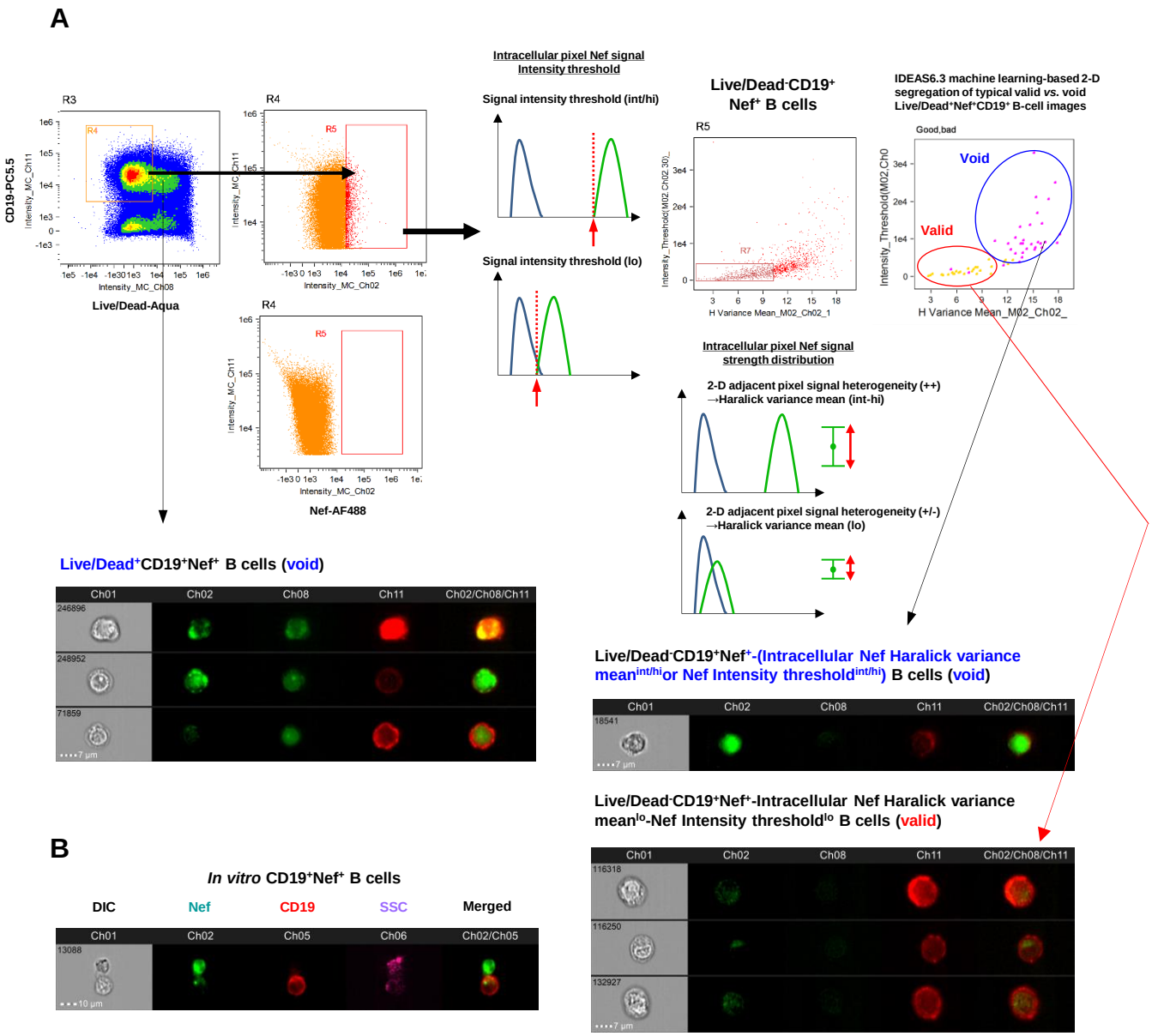
A
CD19-PC5.5
R3
R4
Intensity_MC_Ch11
Intensity_MC_Ch08
Live/Dead-Aqua
R4
R5
Intensity_MC_Ch11
Intensity_MC_Ch02
R4
R5
Intensity_MC_Ch11
Intensity_MC_Ch02
Nef-AF488
Intracellular pixel Nef signal
Intensity threshold
Signal intensity threshold (int/hi)
Signal intensity threshold (lo)
Live/Dead-CD19+
Nef+ B cells
R5
R7
H Variance Mean_M02_Ch02_1
IDEAS6.3 machine learning-based 2-D
segregation of typical valid vs. void
Live/Dead+Nef+CD19+ B-cell images
Good,bad
Void
Valid
H Variance Mean_M02_Ch02_
Intracellular pixel Nef signal
strength distribution
2-D adjacent pixel signal heterogeneity (++)
→Haralick variance mean (int-hi)
2-D adjacent pixel signal heterogeneity (+/-)
→Haralick variance mean (lo)
Live/Dead+CD19+Nef+ B cells (void)
Ch01
Ch02
Ch08
Ch11
Ch02/Ch08/Ch11
246896
248952
71859
7 µm
Live/Dead-CD19+Nef+-(Intracellular Nef Haralick variance
mean int/hi or Nef Intensity threshold int/hi) B cells (void)
Ch01
Ch02
Ch08
Ch11
Ch02/Ch08/Ch11
18541
7 µm
Live/Dead-CD19+Nef+-Intracellular Nef Haralick variance
mean lo-Nef Intensity threshold lo B cells (valid)
Ch01
Ch02
Ch08
Ch11
Ch02/Ch08/Ch11
116318
116250
132927
7 µm
B
In vitro CD19+Nef+ B cells
DIC
Nef
CD19
SSC
Merged
Ch01
Ch02
Ch05
Ch06
Ch02/Ch05
13088
10 µm

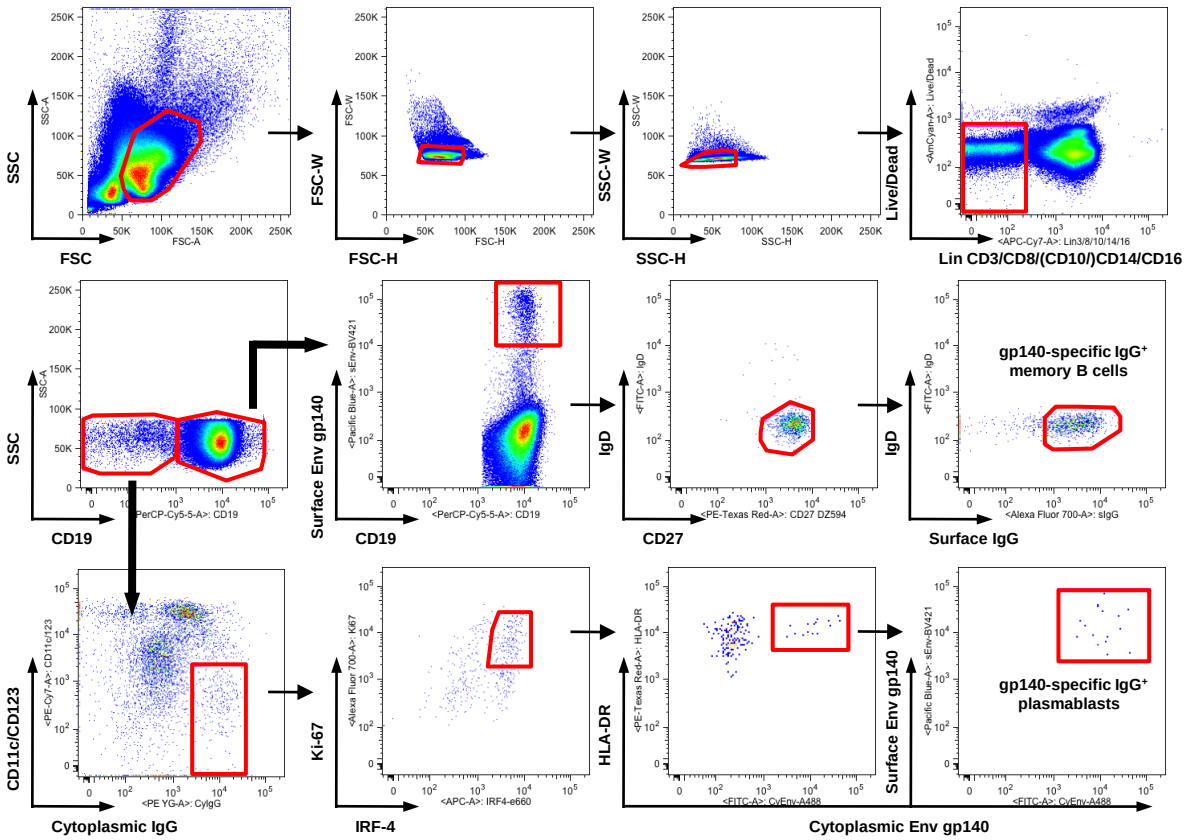
SSC
FSC
FSC-W
FSC-H
SSC-W
SSC-H
Live/Dead
Lin CD3/CD8/(CD10/)CD14/CD16
CD19
Surface Env gp140
IgD
CD27
Surface IgG
gp140-specific IgG+ memory B cells
CD11c/CD123
Cytoplasmic IgG
Ki-67
IRF-4
HLA-DR
Cytoplasmic Env gp140
gp140-specific IgG+ plasmablasts

Key Resources Table				
Reagent type (species) or resource	**Designation**	**Source or reference**	**Identifiers**	**Additional information**
gene (*Lentivirus*)	*env*, *nef*	GenBank	M33262.1	SIV_{mac239}
strain, strain background (*Lentivirus*)	SIV_{mac239}	PMID: 2032289		Obtained via COS-1 transfection of pBR_{mac239} and repropagation on MT4-R5 cells
strain, strain background (*Escherichia coli*)	One Shot™ TOP10 Chemically Competent *E. coli*	Invitrogen (Thermo Fisher Scientific)	Cat#:C404003	For subcloning sequencing
cell line (*Homo-sapiens*)	MT4-R5	PMID: 27122584		STR profiling (+)
cell line (*Chlorocebus aethiops*)	COS-1	ATCC	CRL-1650	STR profiling (+)
cell line (*Macaca fascicularis*)	HSC-F cells (CD4+ T-cell line)	PMID: 8610465	Gift from producer (Dr. Hirofumi Akari)	
cell line (*Macaca mulatta*)	HSR5.4 cells (CD4+ T-cell line)	PMID: 8610465	Gift from producer (Dr. Hirofumi Akari)	
cell line (*Homo-sapiens*)	Ramos B cell line	ATCC	CRL-1596	STR profiling (+)
biological sample (*Macaca mulatta*)	Primary simian PBMCs from SIV-infected macaques	Japan SLC	http://www.jslc.co.jp/service/	Cryopreserved from *Macaca mulatta*

biological sample (*Macaca mulatta*)	Primary simian lymph node cells from SIV-infected macaques	Japan SLC	http://www.jslc.co.jp/service/	Cryopreserved from *Macaca mulatta*
antibody	Mouse monoclonal anti-human CD4-FITC (M-T477)	BD Pharmingen	Cat#556615	FACS (5 µl per test)
antibody	Mouse monoclonal anti-human CD8-PerCP (SK1)	BD Biosciences	Cat#347314	FACS (5 µl per test)
antibody	Mouse monoclonal anti-human CD3-APC (SP34-2)	BD Pharmingen	Cat#557597	FACS (5 µl per test)
antibody	Mouse monoclonal anti-human IFN-γ-PE (4S.B3)	BioLegend	Cat#502510	FACS (5 µl per test)
antibody	Mouse monoclonal anti-SIV_{mac251} Gag p27 mAb	ABL	Cat#4324	FACS (1:500 with conjugation)
antibody	Mouse monoclonal anti-SIV_{mac251} Nef mAb (clone 17)	Themo Fisher Scientific	Cat#MA1-71522	FACS, PLA, immuno-blotting and imaging cytometry (FACS and imaging cytometry, 1:500 with conjugation; PLA, 1:100; immuno-blotting, 1:1000)
antibody	Mouse IgG1 isotype control mAb (P3.6.2.8.1)	Themo Fisher Scientific	Cat#14-4714-85	PLA (1:100)

antibody	Rabbit monoclonal Alexa Fluor 488-conjugated anti-human phospho-Akt (Ser473) (D9E)	Cell Signaling Technology	Cat#4071	FACS (5 µl per test)
antibody	Rabbit monoclonal Alexa Fluor 488-conjugated anti-human phospho-Akt (Thr308) (C31E5E)	Cell Signaling Technology	Cat#2918	FACS (5 µl per test)
antibody	Rabbit monoclonal PE-conjugated anti-human phospho-Akt (Ser473) (D9E)	Cell Signaling Technology	Cat#5315	FACS and imaging cytometry (1:100)
antibody	Rabbit monoclonal Alexa Fluor 647-conjugated anti-human phospho-Akt (Ser473) (D9E)	Cell Signaling Technology	Cat#4075	FACS (5 µl per test)
antibody	Rabbit monoclonal Alexa Fluor 647-conjugated anti-human phospho-Akt (Thr308) (C31E5E)	Cell Signaling Technology	Cat#3375	FACS (5 µl per test)
antibody	Mouse monoclonal anti-human CD19-PC-5.5 (J3-119)	Beckman Coulter	Cat#66328	FACS and imaging cytometry (5 µl per test)
antibody	Mouse monoclonal anti-human CD4, purified (clone L200)	BD Biosciences	Cat#550625	FACS (25 µg/ml per test for blockade)
antibody	Mouse monoclonal anti-human CD3-	BD Pharmingen	Cat#557757	FACS (5 µl per test)

	APC-Cy7 (SP34-2)			
antibody	Mouse monoclonal anti-human CD8-APC-Cy7 (RPA-T8)	BD Pharmingen	Cat#557760	FACS (5 µl per test)
antibody	Mouse monoclonal anti-human CD14-APC-Cy7 (M5E2)	BioLegend	Cat#301820	FACS (5 µl per test)
antibody	Mouse monoclonal anti-human CD16-APC-Cy7 (3G8)	BioLegend	Cat#302018	FACS (5 µl per test)
antibody	Mouse monoclonal anti-human CD10-APC-Cy7 (HI10a)	BioLegend	Cat#312212	FACS (5 µl per test)
antibody	Mouse monoclonal anti-human CD11c-PE-Cy7 (3.9)	BioLegend	Cat#301608	FACS (5 µl per test)
antibody	Mouse monoclonal anti-human CD123-PE-Cy7 (6H6)	BioLegend	Cat#306010	FACS (5 µl per test)
antibody	Mouse monoclonal anti-human HLA-DR-PE-Texas Red (TU36)	Invitrogen (Thermo Fisher Scientific)	Cat# MHLDR17	FACS (5 µl per test)
antibody	Mouse monoclonal anti-human CD27-PE/Dazzle 594 (M-T271)	BioLegend	Cat#356422	FACS (5 µl per test)
antibody	Mouse monoclonal anti-human CD10-PE-Cy7 (HI10a)	BioLegend	Cat#312214	FACS (5 µl per test)

antibody	Rabbit polyclonal anti-human IgD-FITC $F(ab')_2$	DaKo	Cat#F0189	FACS (5 µl per test)
antibody	Mouse monoclonal anti-human CD38-Alexa 647 (AT1)	Santa Cruz Biotechnology	Cat# sc-7325 AF647	FACS (5 µl per test)
antibody	Mouse monoclonal anti-human IgG-Alexa 700 (G18-145)	BD Pharmingen	Cat#561296	FACS (5 µl per test)
antibody	Mouse monoclonal anti-human CD138-PE (DL-101)	eBioscience (Thermo Fisher Scientific)	Cat#12-1389-42	FACS (5 µl per test)
antibody	Mouse monoclonal anti-human IgG-PE (G18-145)	BD Biosciences	Cat#555787	FACS (5 µl per test)
antibody	Rat monoclonal anti-human/mouse IRF4-eFluor 660 (3E4)	eBioscience (Thermo Fisher Scientific)	Cat#50-9858-80	FACS (5 µl per test)
antibody	Mouse monoclonal anti-human Ki67-Alexa 700 (B56)	BD Pharmingen	Cat#561277	FACS (5 µl per test)
antibody	Mouse monoclonal anti-human anti-CD4-PerCP (L200)	BD Pharmingen	Cat#550631	FACS (5 µl per test)
antibody	Mouse monoclonal anti-human anti-CD3-Alexa 700 (SP34-2)	BD Pharmingen	Cat#561805	FACS (5 µl per test)
antibody	Mouse monoclonal anti-human anti-CD95-PE-Cy7 (DX2)	eBioscience (Thermo Fisher Scientific)	Cat#25-0959-42	FACS (5 µl per test)

antibody	Mouse monoclonal anti-human anti-CXCR5-PE (87.1)	eBioscience (Thermo Fisher Scientific)	Cat#12-1859-42	FACS (5 µl per test)
antibody	Mouse monoclonal anti-human PD-1-Brilliant Violet 421 (EH12.2H7)	BioLegend	Cat#329920	FACS (5 µl per test)
antibody	Mouse monoclonal anti-human CXCR3-Alexa 488 (G025H7)	BioLegend	Cat#353710	FACS (5 µl per test)
antibody	Mouse monoclonal anti-human HLA-ABC-FITC (G46-2.6)	BD Biosciences	Cat#557348	FACS (5 µl per test)
antibody	Mouse monoclonal anti-human CXCR4-APC (12G5)	BioLegend	Cat#306510	FACS (5 µl per test)
antibody	Mouse monoclonal anti-human BST2-Alexa647 (RS38E)	BioLegend	Cat#348404	FACS (5 µl per test)
antibody	Mouse monoclonal anti-human CD20 (2H7)	Biolegend	Cat#302324	FACS (5 µl per test)
antibody	Rabbit monoclonal anti-GβL (86B8)	Cell Signaling Technology	Cat#3274	PLA (1:100)
antibody	Rabbit monoclonal anti-mTOR (7C10)	Cell Signaling Technology	Cat#2983	PLA (1:100)
antibody	Rabbit polyclonal anti-human PI3K p85	Merck Millipore	Cat#ABS1856	PLA (1:100)

antibody	Rabbit monoclonal anti-PI3 Kinase p110α (C73F8)	Cell Signaling Technology	Cat#4249	PLA (1:100)
antibody	Goat polyclonal HRP-conjugated anti-monkey IgG (H+L)	Bethyl Laboratory	Cat# A140-102P	ELISA (1:1000)
antibody	Rabbit monoclonal anti-Sin1 (D7G1A)	Cell Signaling Technology	Cat#12860	Co-immuno-precipitation (1:50)
antibody	Mouse TrueBlot™ ULTRA anti-mouse Ig HRP (eB144)	Rockland Immuno-chemicals	Cat# 18-8817-30	Immuno-blotting (1:1000)
antibody	Mouse monoclonal anti-CD3 (FN-18)	Abcam	Cat#ab25109	Stimulation assay (1 µg/ml)
antibody	CD20 MicroBeads, non-human primate	Miltenyi Biotec	Cat#130-091-105	
recombinant DNA reagent	pBR_{mac239}	PMID: 2032289	GenBank M33262	coding full sequence of *nef*-open SIV_{mac239}
sequence-based reagent	9520GA-F	This paper	PCR primers	GGGACAG AAATACAA TCAGGAA CAGTATAT GAATACTC CATGGAG
sequence-based reagent	9520GA-R	This paper	PCR primers	CTCCATG GAGTATTC ATATACTG TTCCTGAT TGTATTTC TGTCCC
sequence-based reagent	9519GA-F	This paper	PCR primers	GAGGGAC AGAAATAC AATCAGA GACAGTA

				TATGAATA CTCCAT
sequence-based reagent	9519GA-R	This paper	PCR primers	ATGGAGT ATTCATAT ACTGTCTC TGATTGTA TTTCTGTC CCTC
peptide, recombinant protein	Peptide Nef_{62-70}	Sigma Aldrich	CTL epitope peptide	QGQYMNT PW
peptide, recombinant protein	Peptide Nef_{62-70}.G63E	Sigma Aldrich	Mutant CTL epitope peptide	QEQYMNT PW
peptide, recombinant protein	Peptide Nef_{62-70}.G63R	Sigma Aldrich	Mutant CTL epitope peptide	QRQYMNT PW
peptide, recombinant protein	GolgiStop	BD Biosciences	Cat#554724	
peptide, recombinant protein	recombinant SIV_{mac251} Env gp130	ImmunoDx	Cat#5001	Ligand stimulation assay (10 µg/ml)
peptide, recombinant protein	recombinant human IL-2	Roche Diagnostics	Cat#1114752 8001	Ligand stimulation assay (100 IU/ml)
peptide, recombinant protein	recombinant human IFN-γ	Gibco (Thermo Fisher Scientific)	Cat#PHC403 3	Ligand stimulation assay (40 ng/ml)
peptide, recombinant protein	recombinant SIV_{mac239} Env gp140 (biotin-conjugated)	Immune Technology	Cat#IT-001-140p	FACS and imaging cytometry (10µg/ml for probing)

peptide, recombinant protein	streptavidin-Brilliant Violet 421	BioLegend	Cat#405225	FACS (1:100)
peptide, recombinant protein	streptavidin-Alexa Fluor 488	BioLegend	Cat#405235	FACS (1:100)
peptide, recombinant protein	streptavidin-PE-Cy7	BioLegend	Cat#405206	Imaging cytometry (1:100)
peptide, recombinant protein	Recombinant Human IL-4 Protein (carrier-free)	R&D Systems	Cat# 204-IL-050/CF	Functional assay (40 ng/ml)
commercial assay or kit	High Pure Viral RNA kit	Roche Diagnostics	Cat#11858882001	
commercial assay or kit	SIV p27 ELISA	ABL	Cat#5436	
commercial assay or kit	SureBlue TMB 1-Component Microwell Peroxidase Substrate	KPL	Cat# 5120-0075	
commercial assay or kit	Prime-Script one-step RT-PCR kit v2	TaKaRa	Cat#RR055A	
commercial assay or kit	KOD-Plus v2	Toyobo	Cat#KOD-211	
commercial assay or kit	Zero Blunt TOPO PCR cloning kit for sequencing	Invitrogen (Thermo Fisher Scientific)	Cat#K287540	
commercial assay or kit	Cytofix/Cytoperm kit	BD Biosciences	Cat#554714	
commercial assay or kit	Monkey Ferritin (Sandwich	LS Bio	Cat#LS-F36490-1	

	ELISA) ELISA Kit			
commercial assay or kit	QuikChange II XL site-directed mutagenesis kit	Agilent Technologies	Cat#200522	
commercial assay or kit	RNeasy Plus Mini kit	Qiagen	Cat#74136	
commercial assay or kit	GeneChip WT Plus reagent	Affymetrix (Thermo Fisher Scientific)	Cat#902280	
commercial assay or kit	GeneChip Human Gene 2.0 ST Array	Affymetrix (Thermo Fisher Scientific)	Cat#902113	
commercial assay or kit	Alexa Fluor™ 488 Antibody Labeling Kit	Invitrogen (Thermo Fisher Scientific)	Cat#A20181	
commercial assay or kit	Alexa Fluor™ 647 Antibody Labeling Kit	Invitrogen (Thermo Fisher Scientific)	Cat# A20186	
commercial assay or kit	Duolink In Situ PLA Probe anti-mouse PLUS	Sigma (Merck)	Cat#DUO92001	
commercial assay or kit	Duolink In Situ PLA Probe anti-rabbit MINUS	Sigma (Merck)	Cat#DUO92005	
commercial assay or kit	Duolink flow PLA detection kit-Green	Sigma (Merck)	Cat#DUO94002	
commercial assay or kit	FuGENE6	Promega	Cat#E2691	
commercial assay or kit	Capturem IP & Co-IP Kit	Clontech/Takara	Cat#635721	

software, algorithm	FACS Diva	BD Biosciences	http://www.bdbiosciences.com/jp/instruments/software/facsdiva/	
software, algorithm	FlowJo v10.7.1	BD/Treestar	https://www.flowjo.com/solutions/flowjo	
software, algorithm	Affymetrix Expression Console Software	Affymetrix/Thermo Fisher Scientific	https://www.thermofisher.com/jp/ja/home/life-science/microarray-analysis/microarray-analysis-instruments-software-services/microarray-analysis-software/affymetrix-transcriptome-analysis-console-software.html	
software, algorithm	IDEAS 6.3 (+Machine learning module)	Amnis/Merck Millipore/Luminex	https://www.luminexcorp.com/imaging-flow-cytometry/	
software, algorithm	Image Lab software	BioRad	https://www.bio-rad.com/en-jp/product/image-lab-software	
software, algorithm	Prism 8	GraphPad Software	https://www.graphpad.com	
other	LIVE/DEAD® Fixable Aqua stain	Invitrogen (Thermo Fisher Scientific)	Cat#L34957	FACS and imaging cytometry (1:1000)

other	APC Annexin V	Biolegend	Cat#640920	FACS (5 µl per 100 µl test)
other	Annexin V Binding Buffer	Biolegend	Cat#422201	Diluent
other	LIVE/DEAD® Fixable Near-IR stain	Invitrogen (Thermo Fisher Scientific)	Cat#L10119	FACS (1:1000)
other	phorbol-12-myristate-13-acetate (PMA)	Sigma/Merck	Cat#P1585	Stimulation assay (10 ng/ml)
other	ionomycin	Sigma/Merck	Cat#I3909	Stimulation assay (10 ng/ml)
other	4–15% Mini-PROTEAN® TGX™ Precast Protein Gels	BioRad	Cat#4561085	
other	SuperSignal West Pico	Thermo Fisher Scientific	Cat#34580	